Department of Physics and Astronomy

University of Heidelberg

Master thesis

in Physics

submitted by

Rima Xenia Schüßler

born in Heppenheim

2015

# A new Detection System for the high-precision Penning-trap mass spectrometer PENTATRAP

**This Master thesis has been carried out by Rima Xenia Schüßler**

**at the**

**Max Planck Institute for Nuclear Physics**

**under the supervision of**

**Prof. Dr. Klaus Blaum**

**Ein neues Detektionssystems für das Hochpräzisions-Penningfallen-Massenspektrometer PENTATRAP**

Das Penningfallen-Massenspektrometer PENTATRAP has das Ziel, Massenverhältnisse für einzelne stabile und langlebige hochgeladene Ionen mit einer relativen Ungenauigkeit von $10^{-11}$ zu messen. Zur Bestimmung der Massenverhältnisse werden die Zyklotronfrequenzen zweier Ionenspezies im Magnetfeld der Penningfallen bestimmt. Die Eigenfrequenzen der Ionen werden durch die nicht-destruktive Detektion der Spiegelströme gemessen. Der Hauptbestandteil des Detektionssystems ist ein kryogener Resonator hoher Güte, welcher aus einer supraleitenden NbTi oder einer normalleitenden Kupferspule in einem Kupfergehäuse besteht. PENTATRAP verwendet Resonatoren für die reduzierte Zyklotron- und die axiale Mode, welche direktes Kühlen und die Detektion dieser Bewegungen ermöglichen. Die winzigen Spiegelströme, welche von einem einzelnen Ion induziert werden, können mit Hilfe von kryogenen GaAs-FET-Verstärkern detektiert werden. Aufgrund eines Umbaus von PENTATRAP wird ein neues Detektionssystem benötigt, welches im Rahmen dieser Masterarbeit entworfen wurde. Die axialen und Zyklotronresonatoren des neuen Designs haben das gleiche Gehäuse, weshalb beide Spulen als Ringspulen entworfen wurden. Das vorhandene Verstärkerdesign wurde an das neue Gehäuse angepasst. Erste Tests der Resonatoren, mit und ohne Verstärker, wurden an einem Kaltkopf durchgeführt. Für ein $^{35}Cl^{10+}$-Ion wird die Dipdetektion mit den axialen Resonatoren, welche an einer Korrekturelektrode angeschlossen sind, zu einer Dipbreite von $\sim 1.73\,\mathrm{Hz}$ führen. Mit dem Zyklotronresonator, welcher an ein Segment der Korrekturelektrode angeschlossen ist, wird für dieses Ion eine Kühlzeitkonstante der Zyklotronbewegung von $\sim 36.6\,\mathrm{s}$ erwartet.

**A new Detection System for the high-precision Penning-trap mass spectrometer PENTATRAP**

The Penning-trap mass spectrometer PENTATRAP aims for measurements of mass ratios of single stable and long-lived highly-charged ions with a relative uncertainty on the order of $10^{-11}$. For the mass-ratio measurement the cyclotron frequencies are measured for two ion species inside the magnetic field of the Penning traps. The ions' eigenfrequencies are measured by means of a non-destructive detection of image currents. Essential part of each detection circuit is a cryogenic high-quality (high-$Q$) resonator, realised as a superconducting NbTi or copper coil in a copper housing. PENTATRAP incorporates detectors for the axial and the modified cyclotron mode, which enable direct cooling and detection of these modes. The tiny image currents induced by a single ion become detectable with the help of cryogenic GaAs FET amplifiers. Due to a modification of the PENTATRAP setup, a new detection system is needed. This detection system was developed in the framework of this thesis. The new detection system features identical housings for the axial and the cyclotron resonators. Both coil types were designed as toroidal coils. The previous amplifier circuit was adapted to the new amplifier box. First tests of the resonators, with and without the cryogenic amplifier, were conducted inside a cryocooler. For a $^{35}Cl^{10+}$-ion the final resonators will lead to a dip width of $\sim 1.73\,\mathrm{Hz}$ for a dip detection measurement with the axial resonator at the correction electrode. With the cyclotron resonator connected to one half of the correction electrode the expected cooling time constant for this ion is $\sim 36.6\,\mathrm{s}$.

# Contents

# List of Figures

# List of Tables

# Chapter 1

# Introduction

High-precision measurements with trapped charged particles or ions are used to test fundamental physical theories. To name a few, tests of QED can be realised by precise measurements of $g$-factors of the free [HFG08] or the bound electron in highly charged ions [Stu11] and comparison with theory. Furthermore, relative mass measurements allow to test the energy-mass equivalence $E = mc^2$ by combining measurements of atomic mass differences and of $\gamma$-ray wavelengths [Rai+05]. Another application of precision Penning-trap mass measurements is to assist in the determination of neutrino properties [BNW10].

In order to achieve high-precision mass measurements the ion needs to be isolated from external influeneces. One possiblity is to store the ion in the vacuum of an ion trap, which leads to long storage and observation times. Since among the most precisely known fundamental units is the second, a high precision can be achieved by converting the mass into a frequency measurement. In a Penning trap this is realised with the help of a magnetic field, which defines the oscillation frequency of the ion.

The Penning trap was first described by John R. Pierce [Pie54] and later realised experimentally by Hans Dehmelt [DW68]. A superposition of a homogeneous magnetic field and a quadrupolar electrostatic field is used to confine the ion. Among other factors the precision of mass measurements depends on the magnetic field fluctuations and electrode voltage fluctuations.

Using Penning traps to perform relative mass measurements, precisions of $10^{-11}$ have been achieved [RTP04]. The limitation in precision thereby arises from magnetic field fluctuations [Mye13]. In order to overcome this limitation, our setup called PENTATRAP consists of five traps which allow simultaneous cyclotron frequency determinations of several ions. Together with a suitable measurement scheme the effect of the magnetic field fluctuations can thereby be reduced, as will be explained in chapter 3. The so achievable relative precision is on the order of a few $10^{-11}$ and below. Mass-ratio measurements at this level of precision can contribute to fundamental studies. One example (neutrino mass studies) will be given in the following, more details of the physics programme of PENTATRAP can be found in [Rep+12].

The Standard Model is the theory of elementary particles and describes all processes between these particles caused by three of the four fundamental forces: the weak, the electromagnetic and the strong interaction. One contradiction to the Standard Model comes from the discovery of neutrino oscillations [Fuk+98], which imply that the neutrino is a massive particle, whereas the Standard Model assumes a massless neutrino.

A direct way to determine the electron (anti-)neutrino mass is to study the $\beta^-$-decay or an electron-capture transition of nuclei [DHMW13]. A promising candidate for such an experiment is the electron capture in $^{163}$Ho, which captures an electron from the inner shells, thereby changing a proton into a neutron. The resulting $^{163}$Dy is formed in an excited state and de-excites by the emission of X-rays or Auger electrons:

$$^{163}\mathrm{Ho} \rightarrow {}^{163}\mathrm{Dy}^* + \nu_e \rightarrow {}^{163}\mathrm{Dy} + \gamma/e^- + \nu_e \quad . \tag{1.1}$$

For a determination of the electron neutrino mass the energy spectrum of all final state particles except the emitted electron neutrino need to be measured. The ECHo collaboration [Gas+14] aims for a determination of an upper limit for the electron neutrino mass with a precision in the range of eV. Therefore, the mass difference of $^{163}$Ho and $^{163}$Dy ($Q_{\mathrm{EC}}$-value) has to be determined with a precision of 1 eV and below and will be measured with PENTATRAP.

The measurement of the de-excitation lines is done via metallic magnetic calorimeters. The maximum energy for the X-rays or Auger electrons is given by the mass difference of the $^{163}$Ho and $^{163}$Dy minus the mass of the neutrino. Therefore, the shape of the endpoint region of the spectrum depends heavily on the neutrino mass. The neutrino mass as well as the $Q_{\mathrm{EC}}$-value can be extracted from the line-shape fit. A comparison of the $Q_{\mathrm{EC}}$-value from the fit with the $Q_{\mathrm{EC}}$-value determined independently by PENTATRAP can then be used as a test of systematic uncertainties.

The PENTATRAP experiment is situated at the Max Planck Institute for Nuclear Physics in Heidelberg. It has access to highly-charged ions over a broad mass range which allows for relative mass measurements with a high precision in the region of medium- to high-$Z$ (atomic number) elements. For the production of highly-charged ions two electron beam ion traps (EBIT) are available, the HD-EBIT [CLUDMU99] and a DREEBIT [Zsc+09]. The PENTATRAP setup was first commissioned in summer 2013 and first ions were already trapped [Dör15]. Due to vacuum problems the setup is currently undergoing a revision, leading to the necessity of a new detection system, which was developed in the framework of this thesis.

In order to achieve a relative mass measurement of ions in a Penning trap with a precision of $10^{-11}$ a sophisticated detection system is needed. At PENTATRAP the ion in the Penning trap is detected by means of the non-destructive image current detection. An ion oscillating in the trap will induce an alternating current in the trap electrodes [DW68]. The frequency of this current is the oscillation frequency of the ion. The current is picked up by a resistance in parallel to the Penning trap. This resistance is realised as an $LCR$-circuit with a high $Q$-value and accordingly low losses in resonance with the ion's frequency. The voltage across the $LCR$-circuit is amplified with a low-noise cryogenic amplifier. Detection systems of this kind have proven single-ion sensitivity

[SWSB11; Ulm+11].

This thesis is structured as follows. The second chapter will give an introduction into the phyics of Penning traps. Afterwards, the detection method for ions is explained as well as different cooling methods.

The third chapter describes the current PENTATRAP setup, as well as future changes to the cryogenic setup. It closes with a possible measurement scheme which prevents the problems in precision caused by magnetic field fluctuations.

Details of the detection system are given in chapter four. A general description of the setup of resonators and amplifiers is followed by a summary of the previous detection system. For first tests with the new detection system a test setup was designed. The determination of the dimensions for the coil body in order to end up with the appropriate resonance frequency is described. Afterwards, the characterisation of the new resonators and amplifiers will be given. The thesis concludes with a summary and an outlook.

# Chapter 2

# Ion Storage and Detection

## 2.1 Basics of Penning Traps

A charged particle or ion with charge $q$ moving with velocity $\vec{v}$ in an electromagnetic field will experience the Lorentz force:

$$\vec{F}_{\mathrm{L}} = q\left(\vec{E} + \vec{v} \times \vec{B}\right) \quad . \tag{2.1}$$

For a homogeneous magnetic field, e.g. $\vec{B} = B\hat{e}_z$, and no electric field the resulting motion is a circular orbit. The revolution frequency, called the free space cyclotron frequency, is given by

$$\omega_c = \frac{q}{m}B \quad , \tag{2.2}$$

where $m$ the ion's mass and $B$ the strength of the magnetic field. The ion's mass can be determined through a measurement of the free space cyclotron frequency, knowing the ion's charge and the magnetic field strength.

However, a precise measurement of the free space cyclotron frequency requires the ion to be confined in three dimensions. A magnetic field along the $z$-axis stores the ion only in two dimensions, the $x$-$y$ plane perpendicular to the magnetic field lines. The ion can still move in the direction of the magnetic field lines.

In a Penning trap the three dimensional storage of the ion is realised by superimposing a weak electrostatic quadrupolar potential onto the strong homogenous magnetic field. The quadrupolar potential is given by

$$\Phi(\vec{r}) = C_2 V_0 \left(z^2 - \frac{x^2 + y^2}{2}\right) \quad . \tag{2.3}$$

$C_2$ is a trap parameter of dimension $1/\mathrm{length}^2$ and $V_0$ is the voltage between certain electrodes of the trap. The quadrupolar potential can be realised by hyperbolical electrodes as shown in Fig. 2.1. Cylindrical electrodes with suitable dimensions and applied voltages can also generate a quadrupolar potential between a center electrode and two

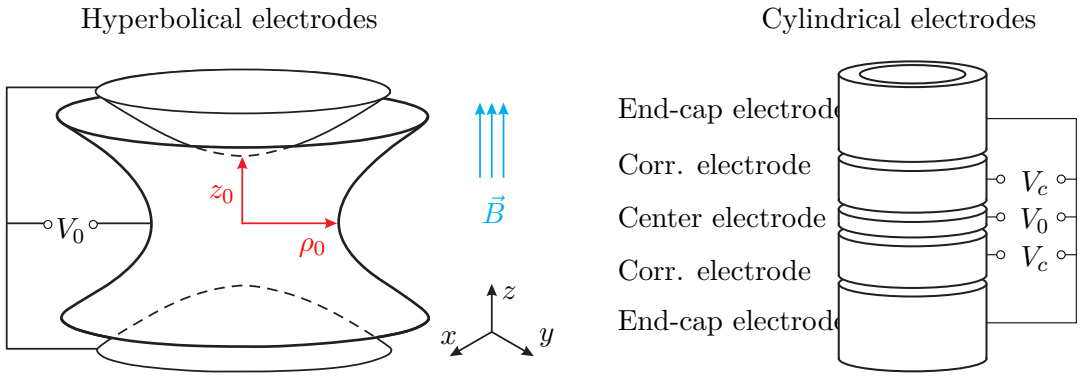


**Figure 2.1:** A schematic drawing of hyperbolical electrodes (left) of a Penning trap consisting of a ring electrode with radius $\rho_0$ and two end caps placed $2z_0$ apart. A quadrupolar electric field is realised by applying a voltage $V_0$ between the ring electrode and the end caps. The same field can be generated by cylindrical electrodes (right) with additional correction electrodes. Three dimensional storage of charged particles is achieved by superimposing a magntic field $\vec{B}$ onto the electric field.

end-cap electrodes. Two additional electrodes in between can be used to correct the electric field.

The superposition of the electric and magnetic fields in a Penning trap leads to the following equations of motion for the ion:

$$\ddot{x} = \frac{C_2 q V_0}{m} x + \frac{qB}{m}\dot{y} \quad , \tag{2.4}$$

$$\ddot{y} = \frac{C_2 q V_0}{m} y - \frac{qB}{m}\dot{x} \quad , \tag{2.5}$$

$$\ddot{z} = -\frac{2C_2 q V_0}{m} z \quad . \tag{2.6}$$

The last equation describes the harmonic oscillatory motion of the ion in axial ($z$-) direction parallel to the magnetic field. The coefficient in Eq. (2.6) translates directly to the axial frequency

$$\omega_z = \sqrt{\frac{2C_2 q V_0}{m}} \quad . \tag{2.7}$$

The radial motion is a superposition of two eigenmotions. To obtain the associated eigenfrequencies the coupled system of differential equations described by Eq. (2.4) and Eq. (2.5) has to be solved. Introducing $u = x + iy$ and using the ansatz $u = e^{i\omega t}$ yields

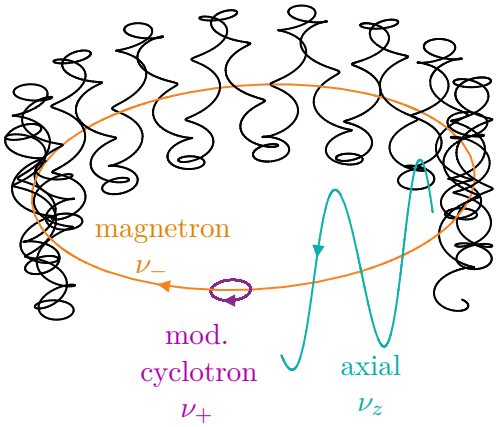


| | | $^{35}Cl^{10+}$ |
|---|---|---|
| free cyclotron | $\omega_c/2\pi$ | 30.712 MHz |
| axial | $\omega_z/2\pi$ | 600 kHz |
| mod. cyclotron | $\omega_+/2\pi$ | 30.071 MHz |
| magnetron | $\omega_-/2\pi$ | 5.862 kHz |

**Figure 2.2:** Left: Schematic drawing of the motion of an ion in a Penning trap. Right: Typical values for the free cyclotron frequency and the eigenfrequencies of a $^{35}Cl^{10+}$-ion in the 7 T magnet of PENTATRAP.

the frequencies for the

$$\text{magnetron motion} \qquad \omega_- = \frac{\omega_c}{2} - \sqrt{\frac{\omega_c^2}{4} - \frac{\omega_z^2}{2}} \approx C_2 \frac{V_0}{B} \qquad \text{and the} \tag{2.8}$$

$$\text{modified cyclotron motion} \qquad \omega_+ = \frac{\omega_c}{2} + \sqrt{\frac{\omega_c^2}{4} - \frac{\omega_z^2}{2}} \approx \omega_c - C_2 \frac{V_0}{B} \quad . \tag{2.9}$$

In first order Taylor expansion ($\omega_z^2 \ll \omega_c^2$) the magnetron frequency is independent of the charge-to-mass ratio of the ion.

In order to store an ion in a Penning trap two conditions have to be fulfilled. First, resulting from Eq. (2.7), the axial frequency has to be real and therefore $C_2 q V_0 > 0$. Second, the magnetron and modified cyclotron frequencies have to be real, leading to $\omega_c^2 > 2\omega_z^2$.

In Fig. 2.2 the three eigenmotions are sketched and their values for a $^{35}Cl^{10+}$-ion are given. For Penning-trap mass spectrometry the following relations between the frequencies are important:

$$\omega_c = \omega_+ + \omega_- \quad , \tag{2.10}$$

$$\omega_c^2 = \omega_z^2 + \omega_+^2 + \omega_-^2 \quad . \tag{2.11}$$

Eq. (2.10) holds for an ideal Penning trap where the electric and magnetic fields are perfectly aligned, whereas the invariance theorem in Eq. (2.11) [BG86] also holds for traps with certain imperfections, for example misalignement of the trap axis and the magnetic field direction.

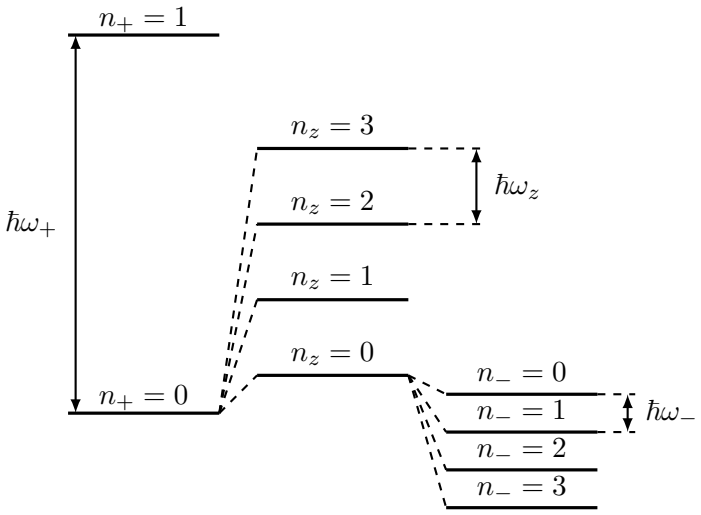


**Figure 2.3:** Energy diagramm (not to scale) of the harmonic oscillator levels for a particle in a Penning trap. Spin contributions are omitted.

All three eigenmotions represent harmonic oscillators [BG82]. In a quantum-mechanical picture (omitting spin contributions) the energy of the ion is

$$E = \left(n_+ + \frac{1}{2}\right)\hbar\omega_+ - \left(n_- + \frac{1}{2}\right)\hbar\omega_- + \left(n_z + \frac{1}{2}\right)\hbar\omega_z \quad , \tag{2.12}$$

where $n_+$, $n_-$ and $n_z$ are the quantum numbers for the respective oscillatory motion. Fig. 2.3 shows the energy levels for a particle in a Penning trap. As can be seen in Eq. (2.12) the energy of the magnetron motion is negative. This is due to the fact that the potential energy dominates over the kinetic energy. Decreasing the total energy leads therefore to an increase in the magnetron radius.

The quantum numbers of the modes can be changed by a dipolar or a quadrupolar excitation [BG86]. The excitation is realised by applying radiofrequency signals to a suitable electrode or a segment of an electrode.

A dipolar excitation can be used to change the quantum number of a single mode [BG86]. This is achieved by applying an rf-voltage (rf: radio-frequency) with the corresponding eigenfrequency of the mode to an electrode or electrode segment. For the magnetron and modified cyclotron mode one possibility is to apply the dipole field to a segmented ring electrode. For the axial mode the rf-signal could be applied to an end electrode.

The quadrupolar excitation can be used to couple two modes and transfer energy between them [Kön+95]. The frequency of the applied field is the sum or the difference of the eigenfrequencies of the coupled modes. In most cases this signal is applied to a segment of an end electrode.

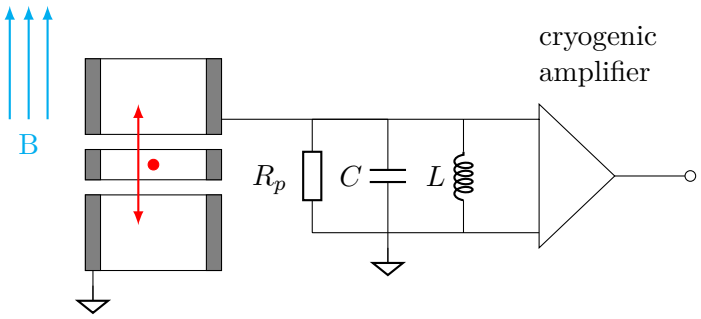


**Figure 2.4:** A schematic drawing of the detection principle used at PENTATRAP. The ion oscillates parallel to the magnetic field lines, leading to a mirror current in the trap electrodes. This current is picked up by a resonant $LCR$-circuit. The voltage drop across the impedance is amplified by a cryogenic amplifier. The frequency of the ion's motion is obtained by taking the Fourier transform of the signal.

## 2.2 Detection Principle

In this section the non-destructive Fourier-transform ion cyclotron resonance (short FT-ICR) technique for the eigenfrequency detection of the ion in the trap is explained. In contrast to destructive techniques, e.g. the time-of-flight ion cyclotron resonance detection technique [GKT80], where the ion is lost after one measurement, using a non-destructive technique enables one to repeatedly use the same ion for measurements, enabling longer storage and observation times and thus higher measurement precision.

The determination of the ion's eigenfrequencies is realised by measuring the image current, which the ion induces into the trap electrodes. The principle of this non-destructive detection is sketched in Fig. 2.4. In the following the image current measurement is explained exemplarily for the axial mode.

An ion moving between the plates of a parallel plate capacitor in the direction of the electric field lines will lead to a mirror charge in the electrodes. Since the electrodes are held on fixed potentials, a current is flowing to balance the additional charge. If the movement is harmonic, e.g.

$$z(t) = z_0 \sin(\omega t) \quad , \tag{2.13}$$

the induced current will oscillate at the same frequency $\omega = 2\pi\nu$, with $\omega$ the angular frequency and $\nu$ the measurable frequency.

According to the Shockley-Ramo theorem [Sho38; Ram39], the current induced by an ion of mass $m$ and charge $q$ is

$$I_z = \frac{q}{D}\dot{z}(t) = \frac{qz_0\omega}{D}\cos(\omega t) \quad , \tag{2.14}$$

where $D$ is the distance of the two plates of the capacitor. Exchanging the parallel plate capacitor with a Penning trap, the electrode distance has to be replaced by the effective electrode distance $D_{\text{eff}}$ [Sta98].

The image current of a single ion is usually tiny. For a $^{35}Cl^{10+}$-ion moving in a trap with $D_{\text{eff}} = 12.5\,\text{mm}$ on an orbit of amplitude $z_0 = 50\,\mu\text{m}$ with the axial frequency $\nu_z = 600\,\text{kHz}$ the induced current is $\approx 24\,\text{fA}$. These small currents are measured as a voltage drop over an impedance in parallel to the trap. This impedance consists of an inductance $L$, which, together with a capacitance $C$ (trap capacitance, inductor's self-capacitance and further parasitic capacitances) and a parallel resistance $R_p$ (dielectric and resistive losses) forms an $LCR$-circuit [DW68]. A cryogenic amplifier is used to further amplify the signal and set the signal-to-noise ratio (see Sec. 2.2.3).

The image current $I$ leads to a voltage drop across the impedance of the $LCR$-circuit

$$U = I \cdot Z_{LCR}(\omega) \tag{2.15}$$

$$= I \cdot \left( \frac{1}{R_p} + \frac{1}{i\omega L} + i\omega C \right)^{-1} \tag{2.16}$$

$$= I\omega L \cdot \left( \frac{1}{\frac{1}{Q}\frac{\omega}{\omega_0} + i\left(\frac{\omega^2}{\omega_0^2} - 1\right)} \right) \quad . \tag{2.17}$$

In the last step the resonance frequency of the $LCR$-circuit $\omega_0 = 1/\sqrt{LC}$ and the quality factor

$$Q = \frac{R_p}{\omega_0 L} \quad . \tag{2.18}$$

were introduced. The latter is also defined as the ratio of the resonance frequency of a resonator to the $-3\,\text{dB}$ bandwidth, $Q = \omega_0/\Delta\omega$.

If the ion's oscillating frequency $\omega$ coincides with the resonance frequency $\omega_0$ of the $LCR$-circuit, the imaginary part of Eq. (2.17) vanishes and the voltage drop across the $LCR$-circuit becomes

$$U = I\omega LQ = IR_p \tag{2.19}$$

The voltage drop therefore depends on the parallel resistance $R_p$.

Attaching the resonator to the trap modifies the motion of the ion. The voltage drop $U = I \cdot Z_{LCR}$ across the resonator generates an electric field $-U/D_{\text{eff}}$ in the trap and leads to a decelerating force on the ion. An additional term arises in the equation of motion of the ion:

$$\ddot{z} = -\frac{qU}{mD_{\text{eff}}} - \omega_z^2 z = -\frac{q^2 Z_{LCR}}{mD_{\text{eff}}^2}\dot{z} - \omega_z^2 z \quad . \tag{2.20}$$

The particle-detector interaction leads to a damping of the ion's motion. The real part of the damping coefficient

$$\gamma = \frac{q^2 \Re(Z_{LCR})}{mD_{\text{eff}}^2} \tag{2.21}$$

describes the dissipation of the ion's energy into the resonator. The energy of the ion is therefore reduced exponentially with the time constant

$$\tau = \gamma^{-1} = \frac{mD_{\text{eff}}^2}{q^2 \Re(Z_{LCR})} \tag{2.22}$$

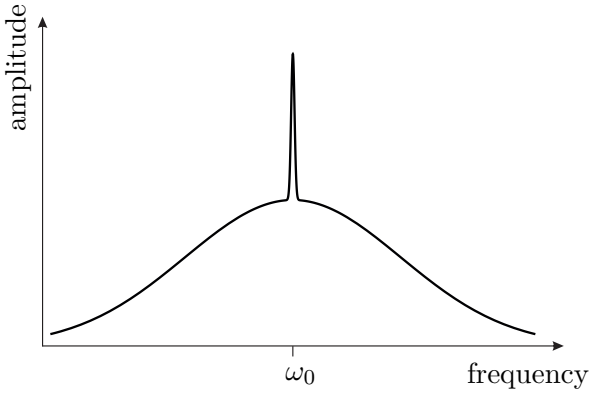


**Figure 2.5:** Schematic drawing of a peak signal. The ion is not yet in thermal equilibrium with the detector. Its signal is a sharp peak on top of the noise signal of the detector.

until the ion is in thermal equilibrium with the detector. Thermal equilibrium is reached when the damping force equals the accelerating force from the detector's noise. This cooling method is called resistive cooling [DW68]. The damping coefficient is only real when $\omega = \omega_0$. For all other cases the imaginary part of the damping force leads to a coil pulling shift in the eigenfrequency of the ion [Stu11; Bra00].

### 2.2.1 Peak-Detection

As long as the ion is not yet in thermal equilibrium with the resonator the ion can be detected by the peak detection method. Eq. (2.17) gives the ion signal for an ion temperature higher than the detector temperature. The ion's signal appears as a sharp peak on top of the detector noise. Fig. 2.5 shows a schematic spectrum of a peak signal.

### 2.2.2 Dip-Detection

In thermal equilibrium with the detector the ion in the trap can be seen as a series $LC$-circuit where the resonance frequency is given by the ion's oscillation frequency, see Fig. 2.6. This can be seen by rewriting Eq. (2.20) in terms of the current using Eq. (2.14):

$$0 = \frac{D_{\text{eff}}^2 m}{q^2} \cdot \dot{I} + Z_{LCR}(\omega) \cdot I + \frac{D_{\text{eff}}^2 m \omega_z^2}{q^2} \int I(t) dt \quad . \tag{2.23}$$

Comparing this equation to the differential equation for a series $LCR$-circuit,

$$l_{\text{ion}} \dot{I} + Z_{LCR}(\omega) I + \frac{1}{c_{\text{ion}}} \int I dt = 0 \quad , \tag{2.24}$$

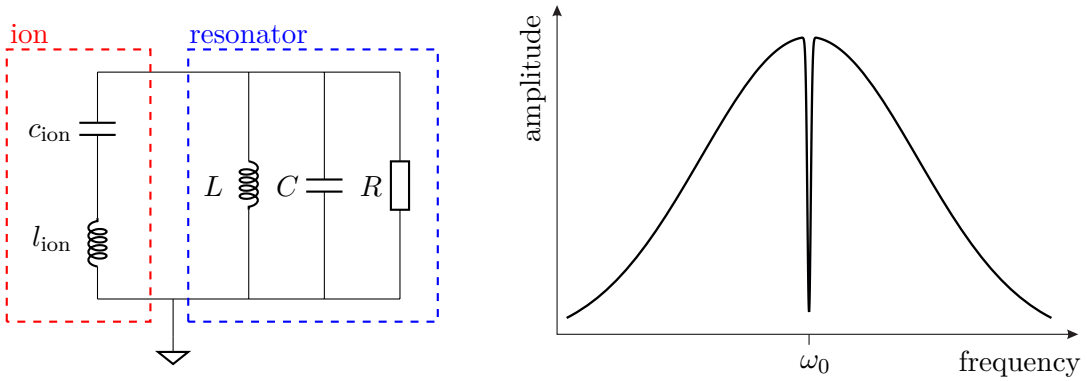


**Figure 2.6:** Left: The ion can be modelled as a series $LC$-circuit with the resonance frequency equal to the ion's eigenfrequency. Right: Schematic drawing of a dip signal. If the ion's oscillation frequency equals the resonance frequency of the detector, the ion effectively shorts the resonator. This leads to a dip in the resonator's noise spectrum.

yields the ion's equivalence inductance and capacitance:

$$l_{\text{ion}} = \frac{D_{\text{eff}}^2 m}{q^2} \quad , \tag{2.25}$$

$$c_{\text{ion}} = \frac{q^2}{D_{\text{eff}}^2 m \omega_z^2} \quad . \tag{2.26}$$

On resonance the ion shortens the resonator leading to a dip in the noise spectrum. Fig. 2.6 shows the ion as an equivalent $LC$-circuit and a resulting dip spectrum. The dip width is defined as [WD75]:

$$\Delta\nu = \frac{q^2 \Re(Z_{LCR})}{2\pi m D_{\text{eff}}^2} = \frac{1}{2\pi\tau} \quad . \tag{2.27}$$

### 2.2.3 Signal-to-Noise Ratio

The signal-to-noise ratio (SNR) is an important parameter for the realisation of a highly sensitive detection system. The ion's motion leads to an induced current in the trap electrodes. The ion itself can therefore be modelled as a current source $I_{\text{ion}}$ parallel to the trap capacitance $C_{\text{trap}}$ and the resonator (see Fig. 2.7). The cryogenic amplifier has an input resistance $R_{\text{in}}$ and capacitance $C_{\text{in}}$. The amplifier's voltage noise density $e_n$ and current noise density $i_n$ are modelled by a voltage and a current source [Dör15], respectively. The amplifier is coupled to the resonator by a capacitance $C_c$ at a certain position on the coil's wire. The coil is thereby divided into two coils with windings $n_1$

and $n_2$, which leads to a transformer-like behaviour. The coupling constant $\kappa$ of the transformer is defined as [Rou12]

$$\kappa = \frac{n_2}{n_1 + n_2} \frac{C_c}{C_c + C_{\text{in}}} \quad . \tag{2.28}$$

Taking the input resistance and the coupling of the resonator to the amplifier into account, the parallel resistance of the system is changed to [Rou12]:

$$R_{\text{sys}} = R_p \frac{1}{1 + \kappa^2 \frac{R_p}{R_{\text{in}}}} \quad . \tag{2.29}$$

For a fixed coupling coefficient $\kappa$ the input resistance of the amplifier has to be as large as possible to increase the system resistance $R_{\text{sys}}$.

The signal-to-noise ratio of the frequency measurement depends on the detection method.

**Dip-Detection** On resonance the ion shorts the resonator and amplifier noise. The SNR is therefore given by the noise of the total system [Rou12],

$$\text{SNR}_{\text{dip}} = \sqrt{\frac{\kappa^2 4 k_B T R_{\text{sys}} + \kappa^4 R_{\text{sys}}^2 i_n^2}{e_n^2}} \quad . \tag{2.30}$$

The signal-to-noise ratio scales with the coupling coefficient $\kappa$. The coupling coefficient also affects the dip width by means of $R_{\text{sys}}$ (see Eq. (2.27)). The ideal dip width is around 1 Hz [Rou12] and the coupling coefficient should be chosen accordingly.

**Peak-Detection** In case of the peak detection the signal is given by the voltage drop over $R_{\text{sys}}$, while the noise consists of thermal, voltage and current noise. The SNR is then given by [Rou12]:

$$\text{SNR}_{\text{peak}} = \sqrt{\frac{\kappa^2 R_{\text{sys}}^2 I_{\text{ion}}^2}{\kappa^2 4 k_B T R_{\text{sys}} + \kappa^4 R_{\text{sys}}^2 i_n^2 + e_n^2}} \quad . \tag{2.31}$$

Besides the SNR, the coupling also affects the time constant $\tau$ defined by Eq. (2.22). This has to be taken into account when choosing the coupling factor.

### 2.2.4 Sideband Cooling

The free-space cyclotron frequency of the ion is determined by measuring all three eigenmotions and finally using the invariance theorem given in Eq. (2.11).

At PENTATRAP, see Chapter 3, the axial motion will be measured directly. The other two eigenmotions will be measured indirectly either by the double-dip method [Ver+04] or by a phase sensitive measurement [SWSB11].

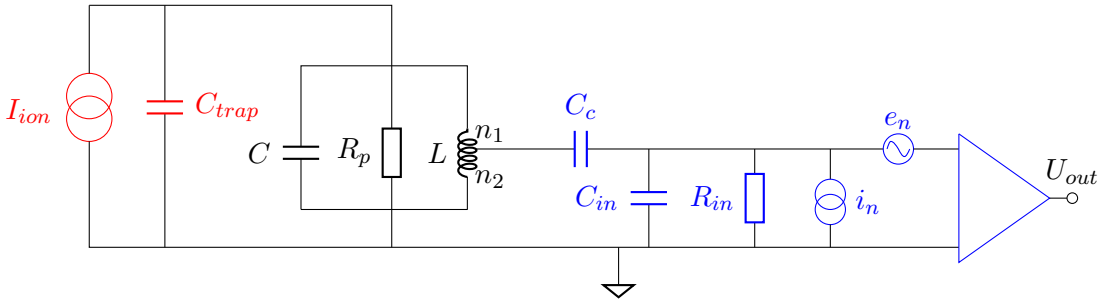


**Figure 2.7:** Model of the trap connected to the resonator and the amplifier. The ion in the trap is modelled as a current source. The amplifier has an input capacitance $C_{in}$ and resistance $R_{in}$ and its noise is described by a voltage noise density $e_n$ and current noise density $i_n$. For more details see text.

**Table 2.1:** Temperatures of the different modes for a $^{35}Cl^{10+}$-ion after coupling to the axial and the cyclotron resonator.

| mode | mod. cycl. | axial | magnetron |
|---|---|---|---|
| coupling to | $T_+$ | $T_z$ | $T_-$ |
| axial detector | 200 K | 4.2 K | 0.04 K |
| cyclotron detector | 4.2 K | 0.08 K | 0.76 mK |

PENTATRAP aims for precisions of $10^{-11}$ and below for relative mass measurements. At this level of precision many energy-dependent eigenfrequency shifts have to be considered [Ket+14a; Ket+14b]. In order to control these shifts the modes of the ion's motion have to be cooled. This can be done by resistive cooling as explained above. The temperature achievable by direct resistive cooling of the mode is the temperature of the resonator, in this case $\approx 4\,\mathrm{K}$. Resistive cooling of the magnetron mode is not possible as a decrease of energy leads to an increase in the magnetron radius. Another possibility is to cool the modes indirectly by coupling them to a directly cooled mode by means of a quadrupolar coupling. The temperature of mode $i$ coupled to mode $j$ depends on the frequency ratio of the two modes [BG86]:

$$T_i = \frac{\omega_i}{\omega_j} T_j \quad . \tag{2.32}$$

Tab. 2.1 shows the temperatures of the modes of a $^{35}Cl^{10+}$-ion after coupling to the axial or cyclotron mode connected to a resonator at 4.2 K.

Energy dependent shifts of the cyclotron frequency are dominated by the energy of the modified cyclotron and axial mode [BG86]. During a phase sensitive measurement [SWSB11] these shifts are smaller when using a cyclotron resonator to cool the modified cyclotron mode compared to using sideband cooling by coupling to the axial mode. For example in [SWSB11] the use of a cyclotron resonator would have decreased the

systematic shifts by a factor of 40. Therefore, PENTATRAP implements axial and cyclotron resonators as discussed in the following chapter.

# Chapter 3

# PENTATRAP Setup

The high-precision Penning-trap mass spectrometer PENTATRAP [Rep+12; Rou+12] aims for mass-ratio measurements with relative uncertainties of $10^{-11}$ and below. It is situated in the accelerator hall of the Max Planck Institute for Nuclear Physics (MPIK). The complete setup extends over two floors, with the ion creation part on the ground floor and the Penning trap setup one floor below. A schematic of the whole setup is shown in Fig. 3.1.

This chapter will give an overview of the current setup including the ion creation inside an electron beam ion trap (EBIT), the beamline to transport the ions into the basement and the cryogenic setup with the five Penning traps and the detection system inside a 7 T magnet. Modifications to the setup as well as a possible measurement scheme will be explained afterwards.

## 3.1 Ion Creation - EBIT

At the level of precision PENTATRAP aims at one limiting factor for the measurement precision are voltage fluctuations during the determination of the free-space cyclotron frequency, see Eq. (2.7) and Eq. (2.11). The precision with which the eigenfrequencies need to be measured depends on the ratio of the eigenfrequency to the free-space cyclotron frequency. In order to achieve a precision of $10^{-11}$ a strong hierachy between the eigenfrequencies is needed [Dör15]. For heavy elements this can be achieved by using ions with a high charge state.

Highly-charged ions can be produced by collisions of atoms with highly energetic (1 keV to several 100 keV) electrons inside an EBIT [EM95]. Characteristic values of the two EBITs available for PENTATRAP (DRE-EBIT and HD-EBIT) are given in Tab. 3.1. A schematic of an EBIT setup is shown in Fig. 3.2.

The trapping region consists of several cylindrical electrodes (shown in Fig. 3.2 as three drift tubes). The electrons emitted from the cathode are accelerated towards the trap region by a potential difference between the cathode and the center drift tube. Behind the trap the electron beam is picked up by a collector electrode. The trapping region is surrounded by magnets (shown in grey). The gradient of the strong magnetic

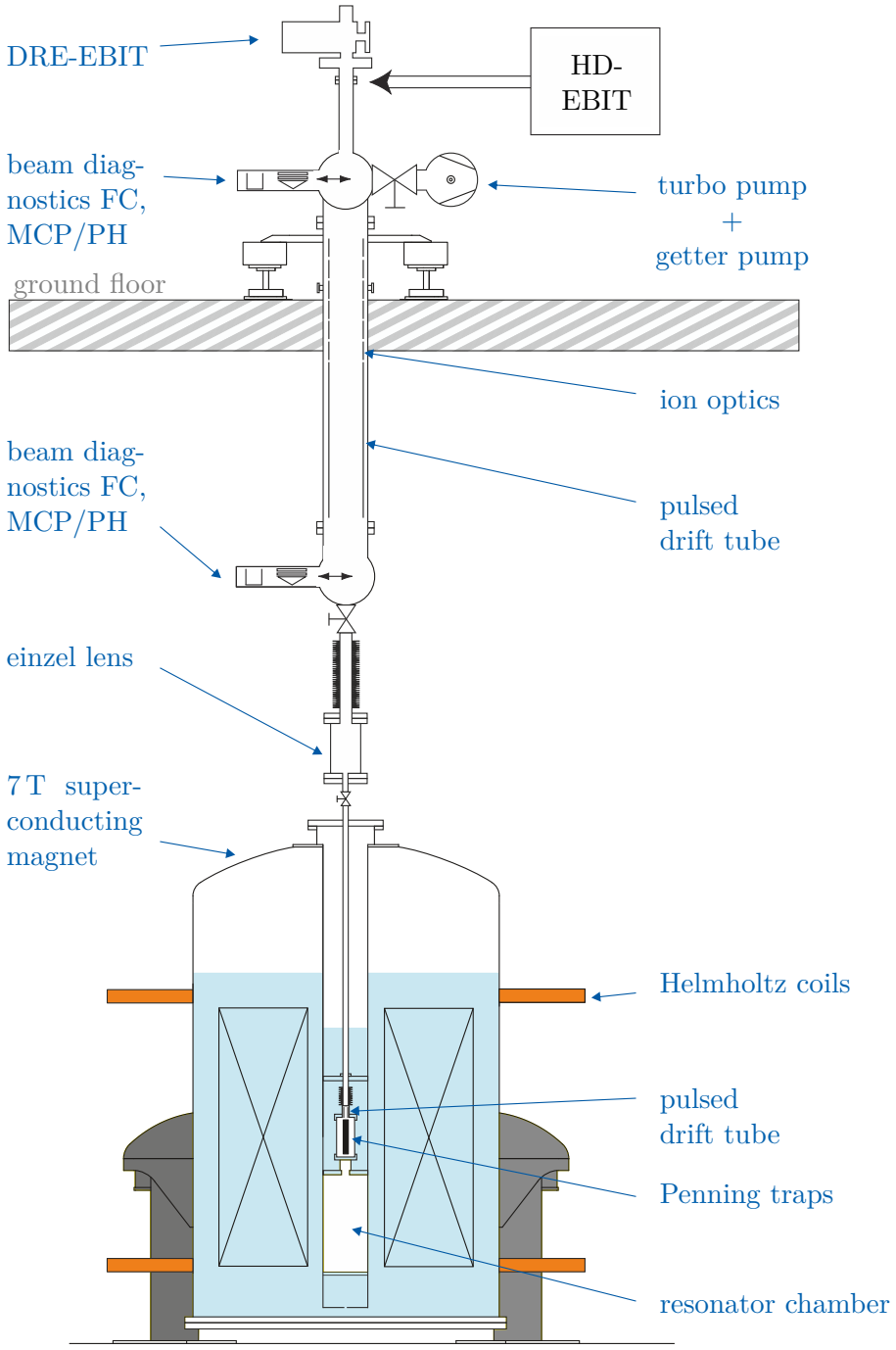


**Figure 3.1:** Overview of the PENTATRAP setup. The liquid helium (LHe) levels inside the magnet are shown in light blue. For details see text.

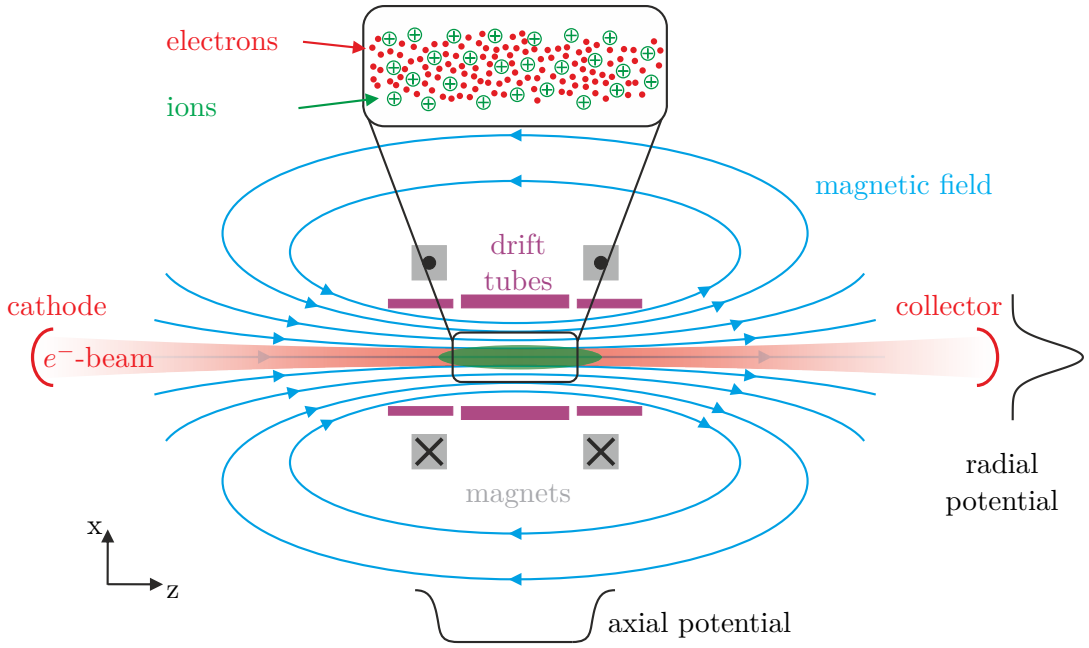


**Figure 3.2:** Schematic of an EBIT. Highly charged ions are created by collisions of atoms with electrons. These are trapped in axial direction in the electrostatic potential of the drift tubes. The magnetic field gradient leads to a compression of the electron beam. The resulting negative space charge confines the ions radially. Adapted from [Rep12].

field (several 100 mT to a few T inside the EBIT) is used to radially compress the electron beam. This increases the electron density in the trapping region. The ions are confined radially by the negative space charge of the electron beam. Axial confinement of the positively charged particles is achieved by setting the central drift tube to a lower potential than the outer drift tubes.

The potential difference between the cathode and the central drift tube defines the electron energy. Since ionisation rates are energy dependent the potential difference can be set in favour of certain charge states. To extract the ions from the EBIT the potential of one of the outer drift tubes is lowered, allowing the ions to escape through a hole in the collector.

PENTATRAP has access to two EBITs. For commissioning purposes the commercially available DRE-EBIT EBIT-W [Zsc+09] is on hand. It is a room-termperature EBIT and can produce any charge state of ions with an atomic number up to $Z \approx 30$, see Tab. 3.1. Heavy highly-charged ions can be produced with the Heidelberg-EBIT (HD-EBIT) [CLUDMU99], which is placed in a separate Faraday room. The electron beam energy of 100 keV is enough to produce e.g. $Hg^{78+}$, see also Tab. 3.1.

**Table 3.1:** Summary of the characteristic values for the DRE-EBIT [Zsc+09] and the HD-EBIT [CLUDMU99]. The data for the HD-EBIT are taken from [Mar+07; LU+04]

| | HD-EBIT | DRE-EBIT |
|---|---|---|
| electron beam energy | 100 keV | 15 keV |
| electron beam current | >500 mA | 15 mA |
| magnetic field | 3...9 T | 250 mT |
| charge state | e.g $Hg^{78+}$, $U^{64+}$, $Xe^{54+}$ | all for Z<30 |

## 3.2 Beamline

The purpose of the PENTATRAP beamline is to guide the ions from the EBITs into the Penning traps inside the cold bore of the magnet (see Fig. 3.1). The beamline is equipped with two diagnostic stations. Each contains a micro-channel plate (MCP) detector and a Faraday cup. Electrostatic lenses are installed to steer and focus the ion beam. To achieve trapping of ions in the Penning traps their kinetic energy is decreased by pulsed drift tubes. For further details refer to [Rep12].

## 3.3 Magnet System

The PENTATRAP magnet is situated in a vibrationally damped and temperature stabilised laboratory. It is a superconducting magnet from *MAGNEX*(Model: 7T/160/AS) with a field strength of $\sim 7\,\mathrm{T}$. Over a region covering three of the five Penning traps the magnetic field inhomogenity is $< 25(1) \cdot 10^{-6}$ [Rep12].

The magnet contains two chambers filled with liquid helium (LHe). The outer chamber houses the superconducting coils and acts as a helium reservoir. The Penning-trap setup resides in the second chamber, the bore of the magnet, which is connected to the helium reservoir by a capillary tube.

Two measures are taken to increase the stability of the magnetic field. In order to reduce the effect of external magnetic field fluctuations, a compensation system consisting of a pair of Helmholtz coils, a fluxgate magnetometer and control electronics is installed [Ris11]. Furthermore, the liquid helium level and the helium pressure in the bore are actively stabilised. This keeps the magnetization of the setup in the bore and the relative position between the trap tower and the magnetic field constant, thus preventing a degradation of the magnetic field stability. The LHe-level inside the bore can be controlled by changing the difference between the pressure inside the bore and the reservoir. More details are given in [Ris14].

## 3.4 Current Cryogenic Setup

The setup in the bore of the magnet consists of a beam tube, the Penning trap stack with five identical traps, an adjustment system, a cryogenic feedthrough flange and the electronics chamber with the detectors. Fig. 3.3 shows a model of the cryogenic setup.

At the core of PENTATRAP are the five Penning traps. Each trap consists of five cylindrical electrodes, one center electrode, two end cap electrodes and two correction electrodes. The liquid-helium cooled trap chamber around the traps provides a high vacuum, enabling storage times on the order of hours or days.

In order to transport the ions between the traps the trap tower has to be aligned with the magnetic field. Hence, an adjustment system is built around the trap chamber.

The detection electronics chamber below the traps houses the resonators and the cryogenic amplifiers. The characteristics of the resonators used in the current version of PENTATRAP will be explained in Sec. 4.3. All cryogenic electrical feedthroughs into the high-vacuum region are mounted on the cryogenic feedthrough flange.

## 3.5 Planned Modifications

In the cryogenic feedthrough flange 20 four-pin feedthroughs are mounted. Some of them became leaky due to the rapid cool-down by directly immersing the setup in LHe. Modifications to the setup are made to prevent this from happening again.

The following changes will be made for version 2 of PENTATRAP [Ris17]:

- Pre-vacuum chamber: A pre-vacuum chamber made of copper will enclose most of the cryogenic setup.
- Pumping barrier: In order to further improve the vacuum in the trap chamber a pumping barrier will be installed above the trap tower. The part above the pumping barrier is pumped through the beamline, while the part below, pumped at room temperature, will reach a higher vacuum due to freezing out of the rest gas at 4.2 K. The pumping barrier then stops atoms from the part above from leaking into the high-vacuum region of the trap.
- Adjustment system: A piezo-driven adjustment system for the alignment of the Penning traps to the magnetic field is planned. This allows for remote adjusting by tilting and translation of the trap system.
- Cryogenic feedthroughs: All feedthroughs will be moved to the room temperature flange and cables will be guided through stainless steel and copper capillaries.
- Resonators: The resonators used for PENTATRAP versions 1 will no longer fit inside the pre-vacuum chamber of PENTATRAP version 2. A new resonator design was therefore developed in the framework of this thesis.

Additionally, an intermediate version, version 1.6, will feature a one-time solution for the vacuum problems. Fig. 3.4 shows all three versions of PENTATRAP.

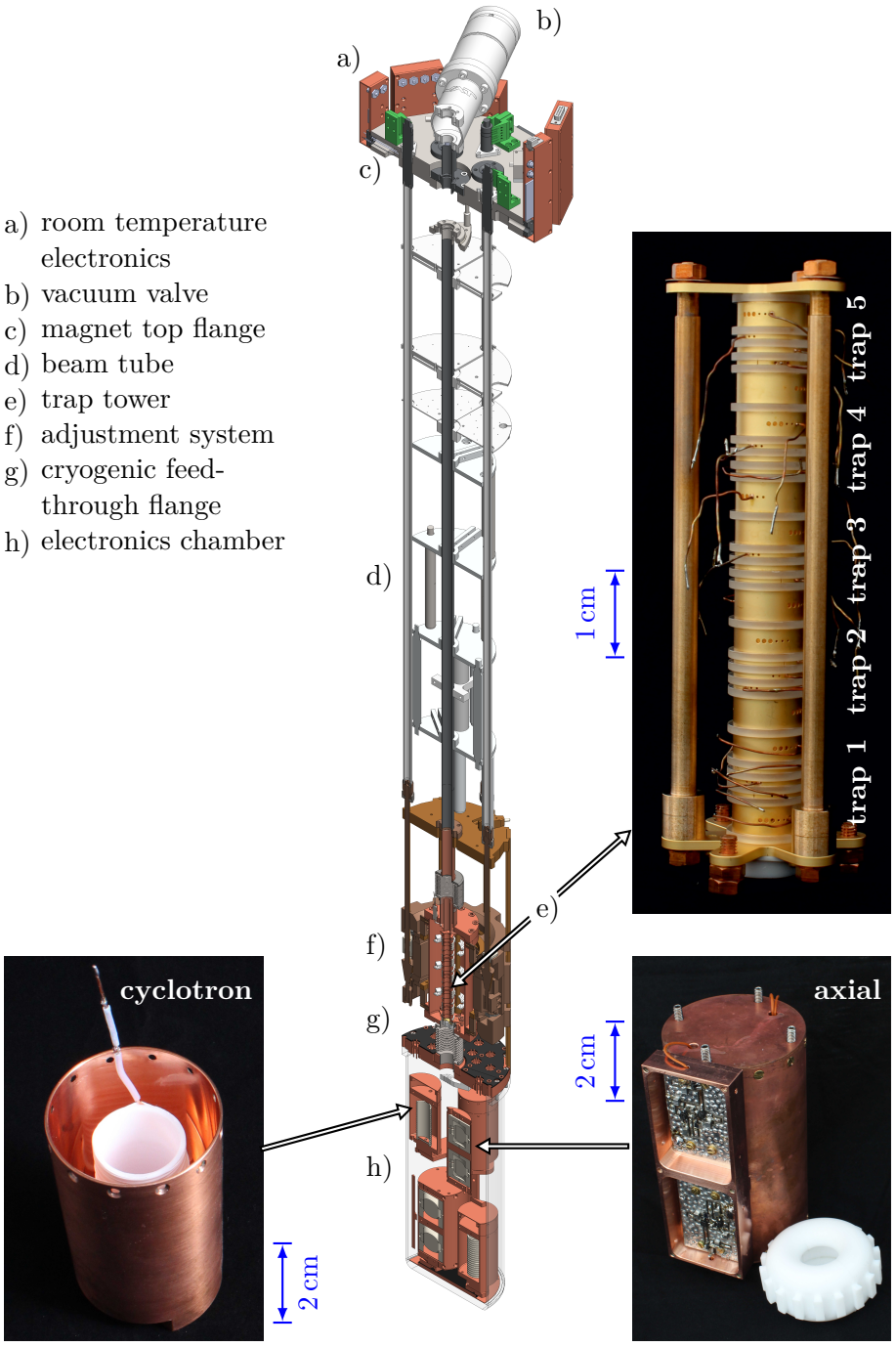


**Figure 3.3:** Model of PENTATRAP version 1 with pictures showing the trap tower, a cyclotron and an axial resonator. All parts except the room temperature electronics, the magnet top flange and the vacuum valve are inside the magnet bore.

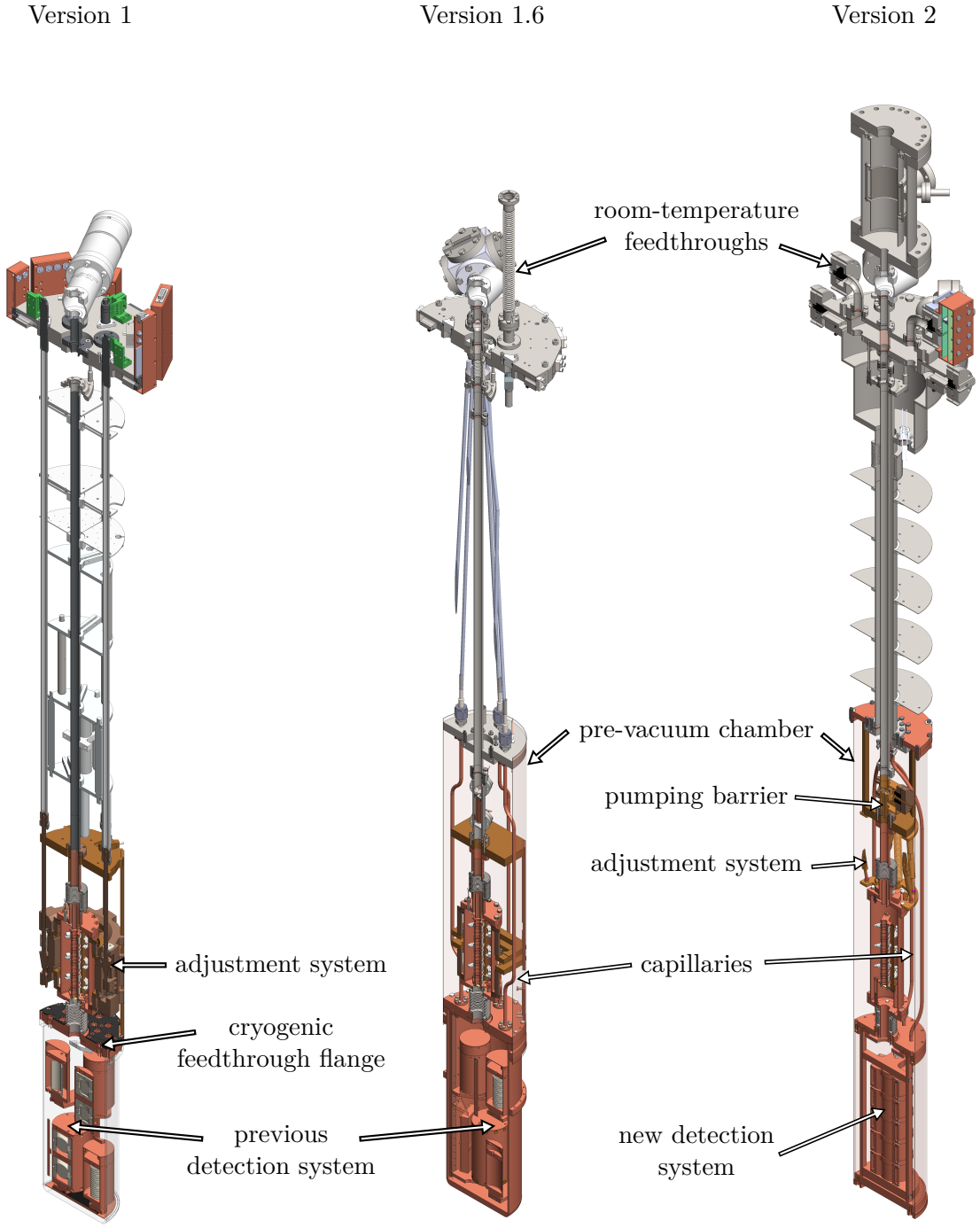


**Figure 3.4:** Overview of the different versions of PENTATRAP. Version 1 (left) was already explained in Fig. 3.3. As an intermediate version, version 1.6 (middle) has characteristics of both version 1 and 2 (right).

Version 1.6 features characteristics of both version 1 and 2. The resonators, the detection electronics and the trap tower are adopted from version 1. The adjustment system was removed to make room for a pre-vacuum chamber. This chamber will be glued onto the cryogenic feedthrough flange, enclosing the trap tower. The electronic feedthroughs are now at room temperature. The cables are guided down from the magnet top flange into the cryogenic part through capillaries.

The capillary system will be more developed in PENTATRAP version 2 where the capillaries are placed in the vacuum chamber around the beam transfer line. The pre-vacuum chamber of version 2 will leave more room between the cryogenic setup and the bore, leading to an easier handling when inserting the setup into the magnet's bore. In the future the adjustment system might be replaced by a piezo driven system and version 2 is designed with a dummy in place.

## 3.6 Measurement Principle

One limiting factor for the precision of Penning-trap mass measurements are the temporal fluctuations of the magnetic field [Mye13]. The five Penning traps allow one to measure the cyclotron frequencies of several ions in different traps at the same time. One example of a possible measurement scheme is given in Fig. 3.5.

In this measurement scheme three ion species are involved. One of the outer traps (in Fig. 3.5 trap 5) is used to store an ion to monitor the magnetic field fluctuations. The other four traps are used to determine the mass ratio of two ion species, 'red' and 'blue'. For the first measurement at $t_1$ a 'blue' ion (blue dot in Fig. 3.5) is in trap 2, a 'red' ion is in trap 3. An additional red ion is situated in trap 1. Taking the ratio of the free cyclotron frequencies measured in trap 2 and 3 for this constellation yields:

$$R(t_1) = \frac{\frac{q_{\mathrm{red}}}{m_{\mathrm{red}}} B_3(t_1)}{\frac{q_{\mathrm{blue}}}{m_{\mathrm{blue}}} B_2(t_1)} \quad . \tag{3.1}$$

After this measurement the ions are moved up one trap, effectively swapping the ion species in the measurement traps 2 and 3. The ratio of the two cyclotron frequencies this time yields:

$$R(t_2) = \frac{\frac{q_{\mathrm{red}}}{m_{\mathrm{red}}} B_2(t_2)}{\frac{q_{\mathrm{blue}}}{m_{\mathrm{blue}}} B_3(t_2)} \quad . \tag{3.2}$$

Under the assumption that the magnetic field ratio $B_3/B_2$ is constant over time and that the charge state is the same for both ion species the following relation gives the mass ratio of the ion species:

$$\sqrt{R(t_1) \cdot R(t_2)} = \frac{m_{\mathrm{blue}}}{m_{\mathrm{red}}} \cdot \sqrt{\frac{B_3(t_1)}{B_2(t_1)} \cdot \frac{B_2(t_2)}{B_3(t_2)}} = \frac{m_{\mathrm{blue}}}{m_{\mathrm{red}}} \quad . \tag{3.3}$$

As indicated in Fig. 3.5 the mass ratio determination starts anew at $t_3$.

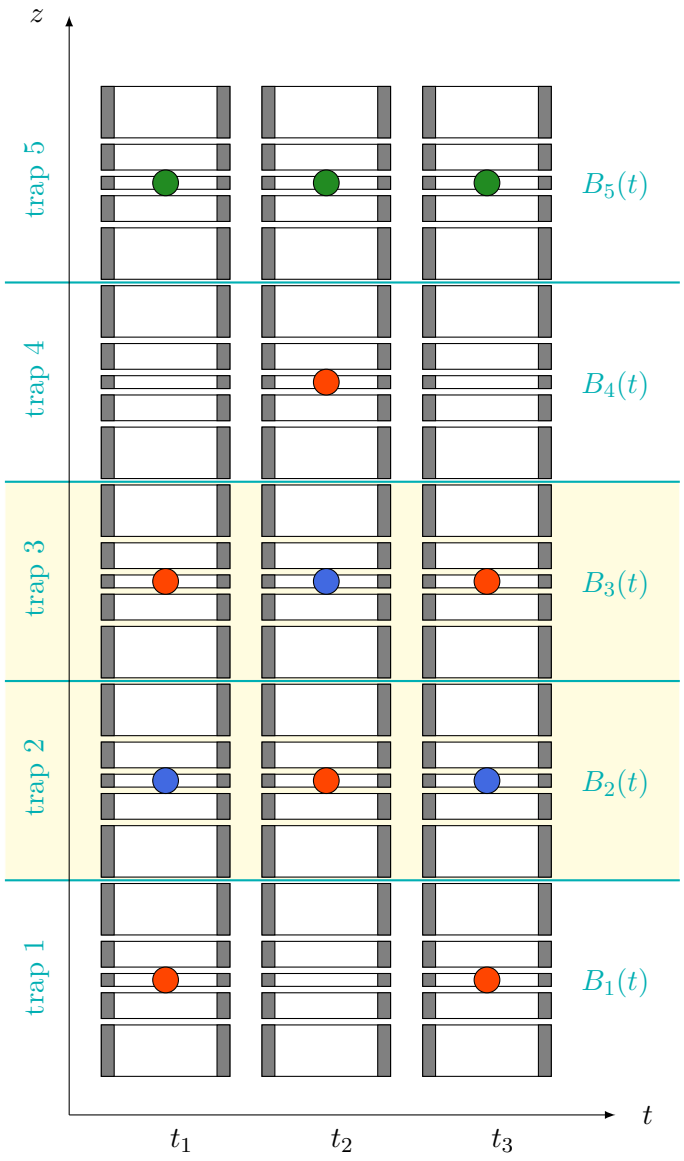


**Figure 3.5:** One possible measurement scheme at PENTATRAP. Trap 5 is used as a monitoring trap, where $\omega_c$ or $\omega_z$ is measured to either monitor magnetic field or voltage fluctuations. The mass ratio of two ion species (red and blue) is deduced from cyclotron frequency measurements in the measurement traps 2 and 3 (yellow) at different times. The ion species are effectively swapped by alternating the ion species in trap 1 to 3 and moving them into traps 2 to 4 for every second measurement. For further details see text.

# Chapter 4

# The PENTATRAP Detection System

In order to build a highly-sensitive detection system several aspects have to be considered. An important parameter in the characterisation of the detection system is the parallel resistance of the $LCR$-circuit or rather the experimentally available $Q$-value. The $Q$-value depends on the losses in the circuit, which can be minimised by choosing the right materials and geometries.

This chapter will start in Sec. 4.1 with a description of the experimental realisation of the $LCR$-circuit and will address possible losses in the resonator. After a short description of the cryogenic amplifiers in Sec. 4.2 and a review of the previous detection system in Sec. 4.3 the design requirements and ideas for the new detection system will be discussed in Sec. 4.4. In order to test the new design a test setup was built and is described in Sec. 4.5. The realisation of the resonators for the axial and the cyclotron detection will be addressed in Sec. 4.6 and Sec. 4.7, respectively.

## 4.1 Experimental Realisation of the $LCR$-Circuit

The $LCR$-circuit described in Sec. 2.2 is realised by attaching an inductance in parallel to the trap. For a realistic description of the $LCR$-circuit losses have to be taken into account. In Fig. 4.1 dielectric losses $R_D$ (described as a resistance in parallel to the

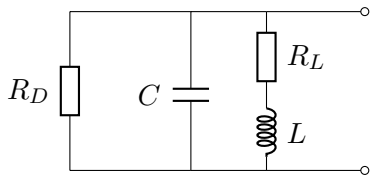


**Figure 4.1:** Schematic circuit diagram of the resonator setup including possible losses. Two effective resistances, $R_D$ and $R_L$, are introduced for dielectric losses and resistive losses, respectively.

capacitance and inductance) and resistive losses $R_L$ are added. The impedance of the complete system is given by:

$$\begin{aligned} Z &= \left( i\omega C + \frac{1}{R_D} + \frac{1}{R_L + i\omega L} \right)^{-1} \\ &= \left( i\omega C + \frac{1}{R_D} + \frac{R_L - i\omega L}{R_L^2 + \omega^2 L^2} \right)^{-1} \\ &\approx \left( i\left( -\frac{1}{\omega L} + \omega C \right) + \frac{R_L}{\omega^2 L^2} + \frac{1}{R_D} \right)^{-1} \quad . \end{aligned} \tag{4.1}$$

In the last step the approximation $R_L^2/\omega^2 L^2 \ll 1$ was used, which holds for typical detectors at PENTATRAP.

A comparison of Eq. (4.1) to Eq. (2.16) gives a relation between the parallel resistance $R_p$ of the $LCR$-circuit and the losses in the system. Close to the resonance frequency this relation can be approximated with:

$$R_p \approx \left( \frac{R_L}{\omega^2 L^2} + \frac{1}{R_D} \right)^{-1} \quad . \tag{4.2}$$

Assuming that the capacitance $C$ of the system (parasitic, trap and cable capacitances) is fixed, the following measures need to be taken to increase the parallel resistance $R_p$:

- For a given resonance frequency the inductance has to be maximised while minimising the parasitic capacitance of the coil.
- The losses $R_L$ in the coil have to be minimised.
- Dielectric losses should be kept at a minimum, which results in a large $R_D$.

In order to control all these parameters the inductance is realised as a coil in a shield or housing. There, the capacitance comes from the parasitic capacitance between the windings and between the coil and the shield. The total capacitance of the detector also includes the capacitance of the cabling and the trap.

The resonator's inductance and the capacitance are dominated by the coil and the shield dimensions. The losses stem mainly from the choice of materials and partly from the geometry.

In the following the effect of the geometry on inductance and capacitance will be discussed. Afterwards, the loss mechanisms for different materials will be addressed. An overview of different materials and geometries of the resonators can be found in Tab. 4.1.

### 4.1.1 Geometry

A coil in combination with the shielding or housing forms a resonator. For the coil geometry two possible shapes have been considered, toroidal and helical. Details are given in the following:

**Table 4.1:** Summary of the materials used for the resonators. The choice of geometry and materials will be discussed in the following sections. Thereby, OFHC stands for oxygen-free high thermal conductivity.

| | axial detection | cyclotron detection |
|---|---|---|
| resonance frequency | $\approx 600\,\mathrm{kHz}$ | $\approx 30\,\mathrm{MHz}$ |
| coil type | toroidal | toroidal /helical (old) |
| winding | chamber winding | single layer winding |
| housing material | OFHC copper | OFHC copper |
| wire material | NbTi | OFHC copper |
| wire insulation | PTFE | none |
| coil body | PTFE | PTFE |

**Toroidal Coils** In a toroidal geometry the magnetic flux is nearly completely confined inside the coil [TMW15]. This minimises the effect of the housing on the coil's inductance and the losses in the housing. The inductance of a shielded coil remains unchanged by the shield and is equal to that of an unshielded coil. The capacitance has to be determined experimentally.

**Helical Coils** A helical coil has a large magnetic stray field compared to a toroidal coil. The stray field leads to eddy currents in the housing and hence resistive losses (see Sec. 4.1.2). The optimal ratio of coil size to housing size can be calculated using the formulars given in [MS59], where expressions for the inductance and the capacitance are also stated. An advantage of this geometry is the manufactoring process with uncomplicated and easy to control winding.

For both coil types the inductance increases with the number of windings $N$: $L \propto N^2$ [LL85]. Therefore, the following relation holds for the resonance frequency:

$$\omega_0 \propto \frac{1}{N} \quad . \tag{4.3}$$

For typical geometries used at PENTATRAP the number of windings for the axial resonator ($\sim 600\,\mathrm{kHz}$) has to be several hundreds, whereas a few tens are sufficient for the cyclotron resonator ($\sim 30\,\mathrm{MHz}$). This allows for the use of wires with diameters up to 1 mm for the cyclotron resonators, while for the axial resonators wires with a diameter of 75 µm are used.

**Capacitance of the Wire** One end of the coil is connected to the trap, the other end is grounded. The voltage resulting from the ion in the trap drops to zero over the

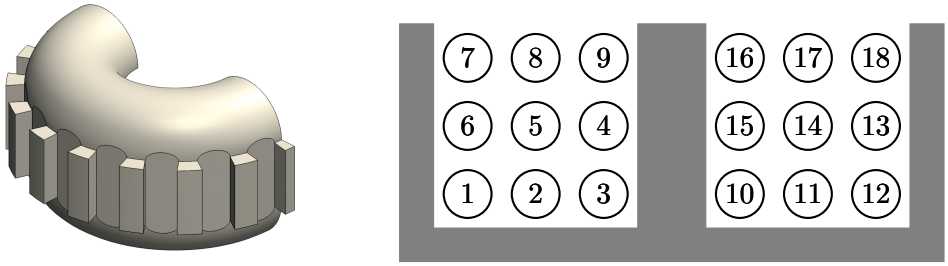


**Figure 4.2:** Left: Picture of one half of the axial coil body of the previous resonator design. The spacer structure on the outside defines chambers, in which the wire is wound. Right: Drawing of a chamber winding with three layers.

length of the coil wire. This leads to a potential gradient over the wire. The potential difference between the windings leads to a parasitic capacitance. In order to reduce the parasitic capacitance, the wire needs to be wound such that the potential difference between neighbouring windings gets minimised. Since the voltage across the coil will drop over the whole length of the wire the largest parasitic capacitance would be between the two ends. In order to maintain the confinement of the magnetic flux inside a toroidal coil the windings are spread out over the whole coil body, making it impossible to avoid the parasitic capacitance between the two ends.

For a single layer winding neighbouring wires have nearly the same potential, giving rise to small parasitic capacitances. In the axial case, the size of the coil does not allow for a single layer winding. In order to reduce the parasitic capacitance between wires of different layers the voltage between them should be as small as possible. This implies that the wire length separating them should be as small as possible. One way to achieve this is to use a chamber winding. The torus is divided into several chambers, where a small number of windings per layer is used. Fig. 4.2 shows a picture of a previous axial coil body and illustrates the chamber winding. The capacitance can additionally be reduced by increasing the distance between the different layers.

### 4.1.2 Losses in the Resonator

The loss mechanisms in the resonator can be split into the losses due to the resistance of the wire, the losses in the dielectric materials and losses in the shield.

**Losses in the wire** The resistance $R$ of a normal conducting wire with length $l$, cross-sectional area $A$ and specific resistance $\rho$ is given by:

$$R = \frac{\rho l}{A} \quad . \tag{4.4}$$

In the final setup the cyclotron resonators will have a resonance frequency of around 30 MHz. At these frequencies the skin effect has to be taken into account [LL85]. If a current is alternating in polarity in a wire the magnetic field induced by the current is

also changing with time. The change in magnetic field leads to the formation of eddy currents, which are opposite to the original field and therefore decrease the current. This effect is larger in the middle of the wire where the magnetic field lines are denser. At high frequencies the current is nearly completely pushed to the surface of the wire. The skin effect can be quantified by the skin depth [LL85]

$$\delta = \sqrt{\frac{2\rho}{\omega\mu}} \quad , \tag{4.5}$$

where $\omega$ is the frequency of the current and $\mu$ the permeability of the wire. The skin depth gives the distance from the wire's outer radius to the radius where the current density has fallen to $1/e$ of its maximum value.

The resistance of a wire with radius $r$ is then

$$R = \frac{\rho l}{A} = \frac{\rho l}{\pi r^2 - \pi(r-\delta)^2} \approx \frac{\rho l}{2\pi r\delta} = \frac{l}{2\pi r}\sqrt{\frac{\omega\mu\rho}{2}} \tag{4.6}$$

and increases with an increase in the frequency $\omega$. By choosing a larger radius, the resistance can be decreased. For the cyclotron resonators a wire with 1 mm diameter was chosen as wires with a larger diameter were not flexible enough to wind a coil.

The skin depth at the cyclotron frequency of 30 MHz for a copper wire with a permeability of $\mu = 1.257$ µH/m and a specific resistance of $\rho_{293\,\mathrm{K}} = 1.71 \cdot 10^{-8}\,\Omega\mathrm{m}$ [Hay14] at room temperature is

$$\delta = 12.01\,\mu\mathrm{m} \quad . \tag{4.7}$$

Imperfections in the wire's surface can be of this order and lead to a longer path for the current at the surface, effectively increasing the length of the wire. This effect can be minimised by polishing the surface of the wire.

The skin effect also depends on the electrical resistivity of the material. Choosing a wire with a low $\rho$ the resistance can also be decreased. A good choice for the material is aluminium ($\rho_{293\,\mathrm{K}} = 2.65 \cdot 10^{-8}\,\Omega\mathrm{m}$ [Hay14]) or copper. Since the resonators will be used at cryogenic temperatures the change of the resistivity with temperature has to be taken into account. The residual-resistance ratio $RRR$ is defined as

$$RRR = \frac{\rho_{300\,\mathrm{K}}}{\rho_{0\,\mathrm{K}}} \approx \frac{\rho_{300\,\mathrm{K}}}{\rho_{4\,\mathrm{K}}} \quad . \tag{4.8}$$

The resistance of a metal consists of two parts: scattering of the electrons on phonons (lattice excitations) of the metal and scattering on impurities and lattice imperfections [Hel81]. Lattice excitations depend on the temperature. The resistivity arising from electron-phonon scattering will therefore decrease with decreasing temperature. At low temperatures the resistivity only depends on imperfections of the metal. Since it is not possible to measure the resistivity at 0 K the value at 4 K is used as an approximation.

The $RRR$ of the copper used for the resonators is on the order of 50. Therefore, the resistive loss in the wire is a factor of $\sqrt{50} \approx 7$ smaller at cryogenic temperatures compared to the room temperature value. This leads to a higher $R_p$ at 4 K.

**Losses in the Housing** Magnetic field lines produced by a current in the coil lead to energy losses when they enter the housing material. The shield around the coil can be seen as a separate coil with only one turn. The coil and the housing have a mutual inductance. The mutual inductance $M$ is defined as [Ter43]

$$M = \frac{\text{flux lines in 2nd coil produced by current in 1st coil}}{\text{current in 1st coil}} \quad . \tag{4.9}$$

The mutual inductance leads to a decrease of the overall inductance of the resonator. The effect of the mutual inductance is smaller for toroidal coils since the magnetic flux is better confined inside the coil as compared to helical coils. Still, for a small number of windings the confinement of the magnetic flux could be considered not to be ideal, leading to a mutual inductance between the housing and the coil.

The resistive losses in the shield arise from energy dissipation in the housing. These losses can be reduced by increasing the distance between the coil and the housing.

**Dielectric Losses** Dielectric losses arise from the energy dissipation due to polarisation currents in the dielectric materials used in the resonators. Dielectric materials are needed for the coil body, the coil holders and, in case of the axial resonator, the wire insulation.

Dielectric materials are characterised by the loss tangent, $\tan(\delta)$, which is defined as the ratio of reactive to dissipative power of the material. The resulting parallel resistance of the $LCR$-circuit is then

$$R_P = \frac{1}{\omega C \tan(\delta)} \quad . \tag{4.10}$$

Thus it is important to choose materials with a low loss tangent. Materials considered to be used in the resonators are PTFE (polytetrafluoroethylene), sapphire and fused silica. For several reasons (machining, price, availability,...) PTFE is mostly chosen.

### 4.1.3 Losses in Superconductors

The axial resonators have a resonance frequency on the order of 800 kHz. At these frequencies the best practice is to use a superconducting wire material [Moo13; Ulm+09]. Due to the 7 T magnetic field of the PENTATRAP magnet superconductors with a higher critical magnetic field $B_{c2}$ are needed. NbTi is a type II superconductor with $B_{c2} \approx 10\,\text{T}$ [Flü+]. It is easily available and good to process and machine as a wire. The following description of the losses in superconductors is based on the description given in [Sch02].

**AC Losses** In the Bardeen-Cooper-Schrieffer (BCS) theory of superconductivity the supercurrent is carried by Cooper pairs. The interaction of a superconductor and an applied electrical alternating current can be described by the 'Two-Fluid Model'. The AC field leads to the formation of two phases: The phase with Cooper pairs is 'superfluid', unpaired electrons are normal fluid and dissipate power. The resistance due to these two phases depends on the applied frequency squared.

**Flux Flow Resistance** Below a critical magnetic field strength $B_{c1}$ ($< B_{c2}$) a type II superconductor cannot be penetrated by a surrounding magnetic field and the superconductor is in the Meißner phase. Above $B_{c1}$, in the mixed phase, the magnetic field enters the superconductor in form of so-called flux tubes. The applied AC current leads to a Lorentz force on the magnetic flux tubes. The flux tubes therefore move perpendicular to the current and generate an electric field in the direction of the current. Dissipative losses arise from the interaction of this current with the normal conducting phase inside the magnetic flux tubes.

The number of magnetic flux tubes increases with increasing magnetic field strength [Ulm+09]. At an upper critical magnetic field strength $B_{c2}$ the flux tubes start touching and the superconducting phase vanishes completely.

### 4.1.4 $Q$-value

The total losses in the resonators consist of all of the effects explained above, and depend on the geometry and the materials. In order to quantify the effect of the losses one can determine the parallel resistance $R_p$. On the other hand experimentally available is the quality factor or $Q$-value.

The quality factor is defined as:

$$Q = 2\pi \frac{\text{total energy in the resonator}}{\text{energy loss per oscillation}} \quad . \tag{4.11}$$

The total energy in the resonator is the sum of the magnetic and electric energy

$$W_{\text{tot}} = W_{\text{el}} + W_{\text{mag}} = \frac{1}{2} L I_{\text{max}}^2 = \frac{1}{2} C U_{\text{max}}^2 \quad , \tag{4.12}$$

which oscillates between the capacitor's electric field and the magnetic field of the inductance. The loss due to Joule heating of the parallel resistance is:

$$W_{\text{loss}} = \int_0^{\text{T}} \frac{U_{\text{max}}^2}{R_p} \cos^2(\omega_0 t) \mathrm{d}t \tag{4.13}$$

$$= \frac{1}{2} \frac{U_{\text{max}}^2}{R_p} \frac{2\pi}{\omega_0} \quad . \tag{4.14}$$

The $Q$-value is then given by

$$Q = 2\pi \frac{\frac{1}{2} C U_{\text{max}}^2}{\frac{1}{2} \frac{U_{\text{max}}^2}{R_p} \frac{2\pi}{\omega_0}} = \frac{R_p}{\omega_0 L} \quad . \tag{4.15}$$

Using Eq. (4.2) the $Q$-value can now be written in terms of the resistive and dielectric losses:

$$Q = \frac{R_p}{\omega_0 L} = \frac{1}{\frac{R_L}{\omega_0^2 L^2} + \frac{1}{R_D}} \frac{1}{\omega_0 L} \quad . \tag{4.16}$$

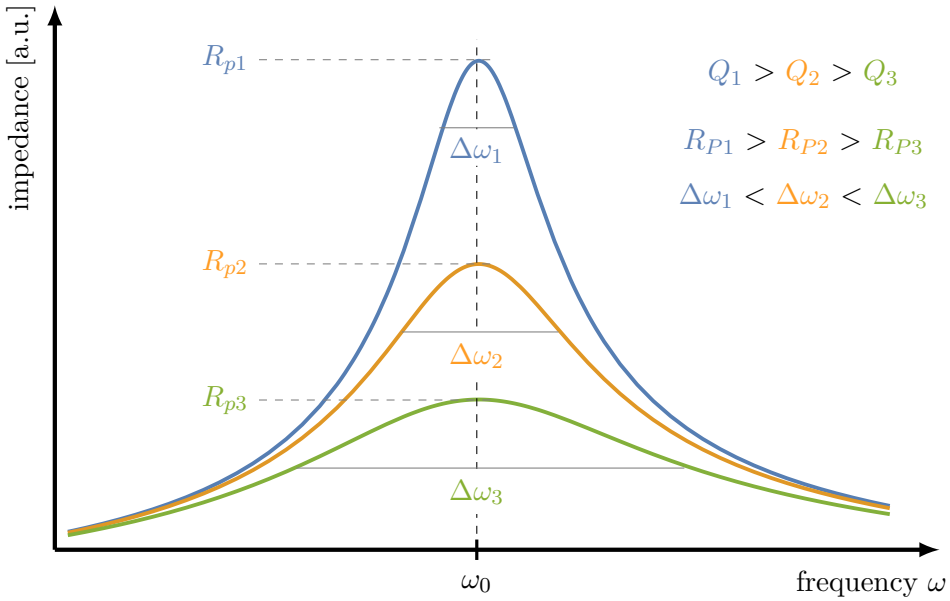


**Figure 4.3:** Resonance curves of an $LCR$-circuit with different parallel resistances $R_p$. All three resonance curves have the same inductance and capacitance. The $-3\,\mathrm{dB}$ bandwidth is shown for every curve, as well as a ranking of the $Q$-values, the bandwidth and the parallel resistances.

Experimentally, the $Q$-value can be determined through measurement of the resonance curve. The absolute value of the complex impedance gives the form of the resonance curve (see Eq. (2.17)):

$$|Z_{LCR}(\omega)| = \left| \frac{\omega L}{\frac{1}{Q}\frac{\omega}{\omega_0} - i\left(1 - \frac{\omega^2}{\omega_0^2}\right)} \right| = \frac{\omega L}{\sqrt{\left(\frac{1}{Q}\frac{\omega}{\omega_0}\right)^2 + \left(1 - \frac{\omega^2}{\omega_0^2}\right)^2}} \quad . \tag{4.17}$$

Another definition of the $Q$-value uses the $-3\,\mathrm{dB}$ bandwidth $\Delta\omega_{-3\,\mathrm{dB}} = \omega_2 - \omega_1$ of the resonant circuit:

$$Q = \frac{\omega_0}{\Delta\omega_{-3\,\mathrm{dB}}} \quad . \tag{4.18}$$

The width of the resonance curve, where the impedance has fallen to $1/\sqrt{2}$ of the maximum value, defines the $-3\,\mathrm{dB}$ bandwidth. The maximum value of the impedance is given by the parallel resistance $R_P$. Therefore, solving the following equation

$$|Z_{LCR}(\omega_{1,2})| = \frac{R_P}{\sqrt{2}} \tag{4.19}$$

leads to the definition of the $Q$-value previously given in Eq. (4.15):

$$\omega_2 - \omega_1 = \frac{1}{R_P C} \quad \Leftrightarrow \quad Q = \frac{\omega_0}{\omega_2 - \omega_1} = \omega_0 R_P C = \frac{R_P}{\omega_0 L} \quad . \tag{4.20}$$

This shows the equality of the two definitions for this case.

Fig. 4.3 shows resonance curves for three different parallel resistances $R_P$. The $-3\,\mathrm{dB}$ bandwidth increases as the parallel resistance decreases. The $Q$-value is highest for the resonance curve with the highest $R_P$.

### 4.1.5 Measurement Setup

In order to measure the resonance curve and determine the resonance frequency of the resonator under conditions similar to those in the final experimental setup, the resonator (with or without the amplifier) is mounted inside a two stage pulse tube cryocooler (*Sumitomo Heavy Industries*, type: SRP-062B-F-50H). The cooling capacity for the first stage is 30 W at 65 K and 0.5 W for the second stage at 4.2 K. It takes around 100 minutes to cool down to the final temperature of $< 3\,\mathrm{K}$ [Col]. The measurement at cryogenic temperatures is especially important for the axial resonator as the NbTi wire only becomes superconducting below $T_c = 10\,\mathrm{K}$ [Flü+].

In order to characterise the resonator and the amplifier three different measurements can be done. A first measurement is the determination of the free resonance frequency of the resonator. An additional measurement with a capacitance in parallel to the resonator allows one to calculate the inductance and capacitance of the resonator. Second, a measurement of the $Q$-factor of the resonator connected to the amplifier allows for the determination of the appropriate gate voltages for a high $Q$-value and a high SNR. Lastly, the measurement of the noise spectrum of the amplifier leads to a determination of the SNR for the dip-detection. The measurement setups are different for each of these three measurements.

The resonator is mounted inside the vacuum system of the cryocooler where feedthroughs allow for electrical connections from room temperature into the 4 K region. The output signal of the resonator is measured and recorded with a network analyser (*R&S ZVL 3 Vector Network Analyzer*). In order to obtain the resonance frequency and the $Q$-value the recorded data is fitted with the corresponding function, which will be discussed below.

For the cyclotron resonators it is also possible to measure the resonance frequency at room temperature. In order to compare these results to the measurement at 4 K the room temperature measurement is done either before cooling down or after heating up the cryocooler.

**Free Resonance Frequency** The free, i.e. unloaded, resonance frequency is measured by exciting the resonator and measuring the damping of the signal dependent on the excitation frequency. The excitation is coupled to the resonator with an impedance $Z_{\mathrm{in}}$ and is picked up by an impedance $Z_{\mathrm{out}}$, which is connected to the $50\,\Omega$ input resistance of a network analyser. Fig. 4.4 shows a schematic of this setup, where the impedance of the resonator is denoted as $Z_{\mathrm{res}}$.

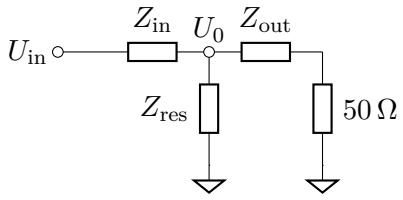


**Figure 4.4:** Schematic circuit for the measurement of the resonator's impedance $Z_{\text{res}}$. The network analyzer excites the resonator with a voltage $U_{\text{in}}$. The network analyzer is represented by its input resistance 50 Ω.

The voltage $U_0$ depends on $Z_{\text{in}}$ and $Z_{\text{res}}$. In order that $U_0$ depends on the impedance of the resonator, $Z_{\text{in}}$ has to be larger than $Z_{\text{res}}$, such that

$$U_0 = \frac{Z_{\text{res}}}{Z_{\text{in}} + Z_{\text{res}}} U_{\text{in}} \approx \frac{Z_{\text{res}}}{Z_{\text{in}}} U_{\text{in}} \tag{4.21}$$

holds. $Z_{\text{out}}$ should also be large compared to $Z_{\text{res}}$ so that the resonator is not loaded. Therefore, $Z_{\text{in}}$ and $Z_{\text{out}}$ are realised by small capacitances.

For the measurement of the free resonance frequency in the cryocooler two cryogenic coaxial cables are capacitively coupled to the resonator, one to excite and one to measure the resonance frequency. In order to avoid crosstalk between the two cables they are spatially separated. Depending on the geometry of the housing the resonator is excited by guiding the inner conductor of one coaxial cable inside. The other cable is capacitively coupled to the hot end (i.e. not grounded) of the coil by wrapping the inner conductor around the wire and fixing it with PTFE tape, see Fig. B.2. This coupling is not reproducible and can lead to different resonance frequencies. The variation thereof will be taken as the error of the free resonance frequency.

In order to amplify the signal of the resonator two *Mini-Circuit Low Noise Amplifiers ZFL-500Ln+* are used, which are connected to the input of the network analyzer. The amplification of the signal is then $\approx 50\,\text{dB}$ [Min].

The resonance curve is described by the absolute value of the resonator's impedance. It can be fitted with a function

$$f_{\text{free}}(\nu) = \sqrt{\frac{4\pi^2 \nu_0^2 L_{\text{fit}}^2}{\frac{1}{Q^2} + \left(\frac{\nu}{\nu_0} - \frac{\nu_0}{\nu}\right)^2}} \quad , \tag{4.22}$$

with the fit parameters $Q$, $\nu_0$ and $L_{\text{fit}}$. $L_{\text{fit}}$ does not represent the inductance of the system but is rather a measure of the maximum value of the curve.

**Characterisation of the Amplifier** Measuring the combined performance of the amplifier and the resonator eliminates the problem of non-reproducible couplings. The coil wire is directly soldered to the input of the amplifier, possible capacitative coupling is realised by a capacitor on the amplifier board. The resonance curve can be described by the same function as the free resonance frequency, see Eq. (4.22).

**Noise Spectrum of the Amplifier** With the final setup the measurement of the eigenfrequencies is done by a dip or peak detection of the ion's signal on the resonator noise, see Sec. 2.2.2 and Sec. 2.2.1. In the case of the resonator only connected to the amplifier two noise sources have to be considered.

The measurement of the noise spectrum is done with the same setup as the characterisation of the amplifier. The noise spectrum can be described by

$$f_{\text{noise}}(\nu) = \sqrt{4k_{\text{B}}T\,\text{Re}(Z)\Delta\nu + e_n^2\Delta\nu} \quad . \tag{4.23}$$

The first term represents the resonator noise, the second the noise of the amplifier, where $e_n$ is the noise density. $\Delta\nu$ describes the measuring bandwidth (usually between 10 Hz and 1 kHz), $k_B$ is the Boltzmann constant, $T$ the temperature of the detector and $\text{Re}(Z)$ is the real part of the resonator's impedance. The real part of the impedance depends on the frequency $\nu$ and is given by

$$\text{Re}(Z) = \left(\frac{1}{R_P} + \frac{R_P}{4\pi\nu_0^2 L^2}\left(\frac{\nu}{\nu_0} - \frac{\nu_0}{\nu}\right)^2\right)^{-1} \quad . \tag{4.24}$$

Here, $R_P$ is the parallel resistance of the detector, $\nu_0$ the resonance frequency and $L$ the inductance of the resonator.

## 4.2 Amplifiers

The cryogenic amplifier plays an important role in the highly-sensitive detection system. A high input resistance and low noise is mandatory for a high SNR (see Sec. 2.2.3).

The axial amplifier presented here was developed by S. Sturm in his PhD thesis on precision $g$-factor measurements of the bound electron in highly charged ions [Stu11], the cyclotron amplifier was designed for the $g$-factor proton experiment [Bla+09] by S. Ulmer [Ulm11]. Both designs were adapted for PENTATRAP by Ch. Roux [Rou12]. During the design of the new detection system a new board layout of the amplifiers was developed. In this section the main characteristics of the amplifiers will be explained together with important aspects of the board layout.

**Characteristics** In order to reduce dielectric losses and parasitic capacitances the amplifier is mounted as close as possible to the resonator. Therefore, the amplifier will be operated at 4 K and experiences a magnetic field of up to 7 T (the magnetic field decreases over the length of the resonator chamber). Therefore, the following charactertistics of the amplifier are essential:

- Low voltage-noise and current-noise density: For a high signal-to-noise ratio the voltage-noise and current-noise density have to be minimised. Choosing the right components, especially a low-noise FET (field effect transistor), and board layout can minimise the noise of the amplifier.

- High input impedance: The input resistance and capacitance of the amplifier are in parallel to the resonator (see Fig. 2.7) and thus shift and damp the resonator. A high input resistance and a small capacitance ($\approx 1\,\mathrm{pF}$) are needed. The board contributes to the parallel and the gate-to-drain capacitances. In order to reduce dielectric losses the board is made out of a PTFE-copper laminate (*Taconic*).
- Negligible parasitic feedback into the resonator should be avoided since it can lead to oscillations of the system [Ulm11].
- Low power consumption: The amplifiers are in thermal contact with the liquid helium bath. A high power consumption would lead to a heating and a loss of liquid helium.

The components used in both amplifiers are surface mounted devices (SMD). The FETs are dual-gate GaAs FETs, which do not suffer from carrier freeze out at low temperatures [Lee93]. In order to avoid parasitic signal paths a proper grounding is needed. The board of the amplifier is grounded by direct electrical contact to the housing of the resonator. The grounding of the ground planes on the top side is realised by so-called vias, which are holes connecting the top to the bottom side of the amplifier board. Usually, either wires or copper rivets are put in the holes and soldered to the top and bottom side. Additionally, the vias also reduce the capacitance of the board. The $Q$-value of the coupled system of resonator and amplifier depends on the proper grounding and thereby on the vias.

Parasitic feedback is mostly due to the gate-to-drain Miller capacitance [Mil19]. A cascode is a two stage amplifier, where the first stage is in common source and the second stage is in common gate configuration. By using a cascode structure the output signal is decoupled from the first FET and the effect of the Miller capacitance is reduced. Additionally, by spatial separation of the gate and drain circuit paths the capacitance between the two can be reduced.

The resistance of the drain-source channel of the FET causes a Johnson-type thermal noise, which scales with the temperature [Stu11]. Therefore, thermalisation of the source is ensured in the board setup by putting it close to the screw used to fixate the amplifier board. At the frequencies of the axial resonators the $1/f$-noise plays an important role. Measures to reduce this noise are discussed in [Stu11].

The cold end of the coil is grounded on the board by a 3 nF capacitance. Since the trap is directly connected to the hot end of the coil, this ensures an AC grounding but allows for biasing the electrode with a DC voltage.

**Axial Amplifier** The circuit diagram of the axial amplifier is shown in Fig. 4.5. The axial amplifier is set up in three stages. The first stage is formed by two NE25139 (*NEC*) dual-gate GaAs FETs. The NE25139s are formed by two transistors in series, which leads to an internal cascode structure. By shorting the two gates the total channel length extends from the source of the first to the drain of the second transistor. If both gates are identical, this reduces the noise by a factor of 4 and doubles the capacitance. The use of two NE25139s further reduces incoherent noise sources by a factor of $\sqrt{2}$.

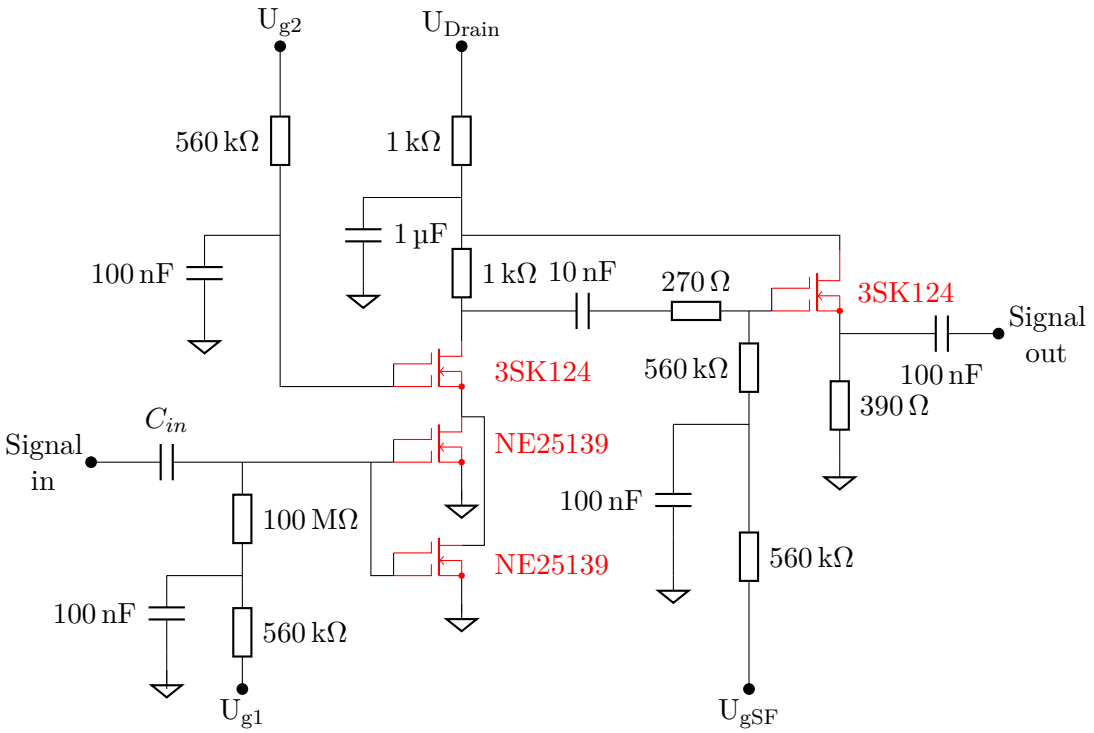


**Figure 4.5:** Circuit diagram of the axial amplifier. The GaAs FETs are marked in red. $C_{in}$ can be chosen to modify the coupling constant $\kappa$. In order to reduce fluctuations of the supply voltages ($U_{g1}$, $U_{g2}$ and $U_{\text{Drain}}$) they are filtered by a low-pass filter. $U_{\text{gSF}}$ is put to ground. More details are given in the text.

In order to suppress parasitic feedback a cascode is formed together with the 3SK124 (*NEC*). The third stage is formed by a 3SK124 in source follower configuration to match the output impedance to the following transmission line. This prevents reflections.

The axial resonator is connected to the amplifier via a tab, a wire soldered to the coil wire at a certain position defining the coupling constant $\kappa$ introduced in Eq. (2.28). A picture of the new axial amplifier can be seen in Fig. B.4.

**Cyclotron Amplifier** The circuit diagram of the cyclotron amplifier is shown in Fig. 4.6. The cyclotron amplifier is set up in two stages. The first stage is a cascode, employing the internal dual gate functionality of an NE25139 and the second stage is a ATF35143 (*Avago*) for matching to the following transmission lines.

Additionally, a varactor diode is coupled to the input of the amplifier and is thus in parallel to the resonator. This allows for fine-tuning of the resonance frequency. The varactor diode MA46H072 from *MACOM* [MC] is chosen, which has a tunable

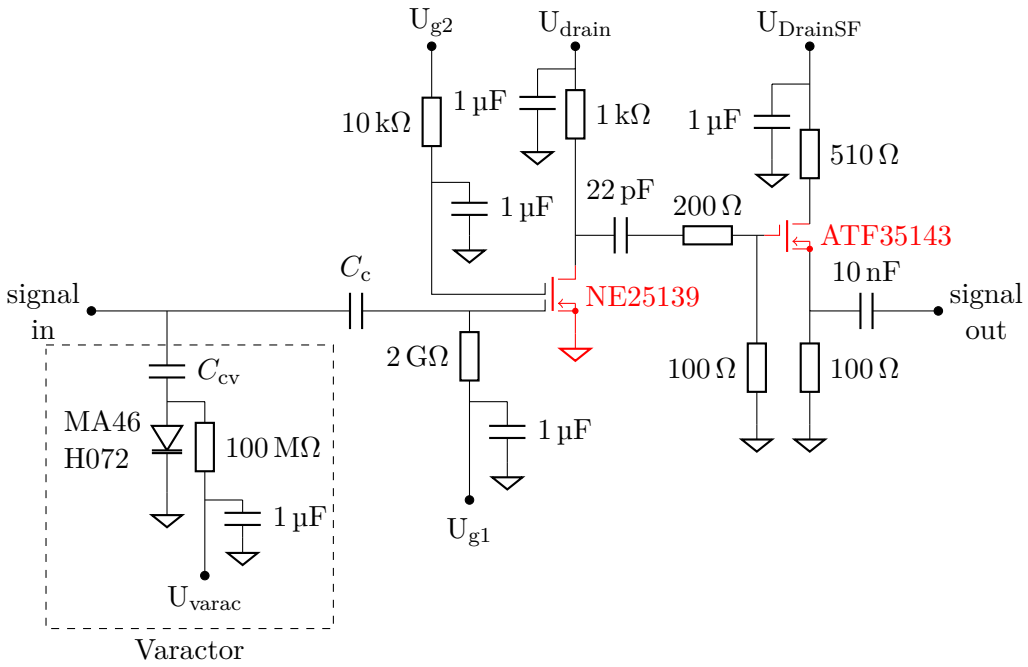


**Figure 4.6:** Circuit diagram of the cyclotron amplifier. The resonator is coupled to the amplifier by a capacitance $C_c = 0.3\,\mathrm{pF}$. The varactor diode is connected to the hot end of the coil with a capacitance $C_{\mathrm{cv}} = 2.2\,\mathrm{pF}$.

capacitance of $1 \ldots 8\,\mathrm{pF}$. It is coupled to the amplifier input by a couple capacitance of $C_{\mathrm{cv}} = 2.2\,\mathrm{pF}$.

For the previous detection system the varactor was mounted on a separate board outside the amplifier chamber. In order to reduce any parasitic capacitance arising from additional cabling between the amplifier and the varactor board, the varactor setup was integrated onto the amplifier board for the new amplifier. A picture of the new cyclotron amplifier can be seen in Fig. B.5.

## 4.3 Previous Detection System

The previous detection system was developed in the framework of the PhD theses of A. Dörr [Dör15] and Ch. Roux [Rou12]. Pictures of a cyclotron and axial resonator as well as a model of the resonator chamber are shown in Fig. 3.3. In total, this detection system consists of two axial housings with two coils each and four cyclotron housings with one coil each. These resonators will be used in the intermediate version of PENTATRAP, called version 1.6. For commissioning of the setup $^{40}\mathrm{Ar}^{9+}$ will be used as it is easily producible. $^{129}\mathrm{Xe}^{29+}$ and $^{187}\mathrm{Re}^{42+}$ have a similar $q/m$-ratio (see Fig. 4.7) and might be used for a first measurement with PENTATRAP version 1.6. The main characteristics of the cyclotron and the axial resonators are given below, with a summary in Tab. 4.2.

**Table 4.2:** Characteristic values of the previous detection system (see [Rou12]). The materials used in the resonators are already given in Tab. 4.1.

| | axial detection | cyclotron detection |
|---|---|---|
| coil type | toroidal | helical |
| resonance frequency $\nu_0$ | 841.8 kHz | 59.16 MHz |
| $Q$-value @ 4 K | 65000 | $\sim$ 4000 |
| number of windings | ~800 | 15 |
| inductance $L$ | 3.2 mH | 2.3 µH |
| capacitance $C$ | 7 pF | 3.2 pF |

### 4.3.1 Axial Resonator

The different materials used in the axial resonator are given in Tab. 4.1. The axial housing was designed to hold two toroidal coils in separate chambers. On the outside of the coil body the spacer structure creates 18 chambers in which the wire is wound in layers. The spacers also serve as a contact point for the holders of the coils, which are two PTFE rings. In order to ensure thermal contact the wire is connected to the coil body with a thin (75 µm) PTFE tape.

The axial coils have 781 windings, leading to a free resonance frequency of 840 kHz to 1000 kHz and a $Q$-value of 43 000 to 66 000. Attaching the amplifier and the trap gives a final resonance frequency of around 600 kHz.

To allow for good electrical connections during the measurement a short piece of copper wire is soldered to both ends of the NbTi wire. One end (the cold end) of the coil is soldered with a coupling capacitance of 3 nF onto an eyelet, which is guided through the toroid and connected via a bolt to the bottom of the chamber. The other end (hot end) and the tab are led out of the housing through holes in the lid and guided into the amplifier chamber or to the trap. The amplifier box, also containing two amplifiers in separate chambers, is screwed to the side of the resonator housing.

Since the axial frequency of an ion can be tuned by varying the voltage of the ring electrode the same resonator can be used for different ions. Without any changes to the geometry and desgin the axial resonators will be thus implemented in PENTATRAP version 1.6.

### 4.3.2 Cyclotron Resonator

In contrast to the axial resonator the cyclotron resonators are helical coils. 15 turns are necessary to reach a free resonance frequency of 59.16 MHz [Rou12]. The maximal $Q$-value at a temperature of 3 K was $\sim$ 4000. Connecting the resonator with the amplifier and the trap leads to a resonance frequency of $\approx$ 30 MHz. Without the varactor board the $Q$-value of the resonator connected to the trap and the amplifier is $\approx$ 1500.

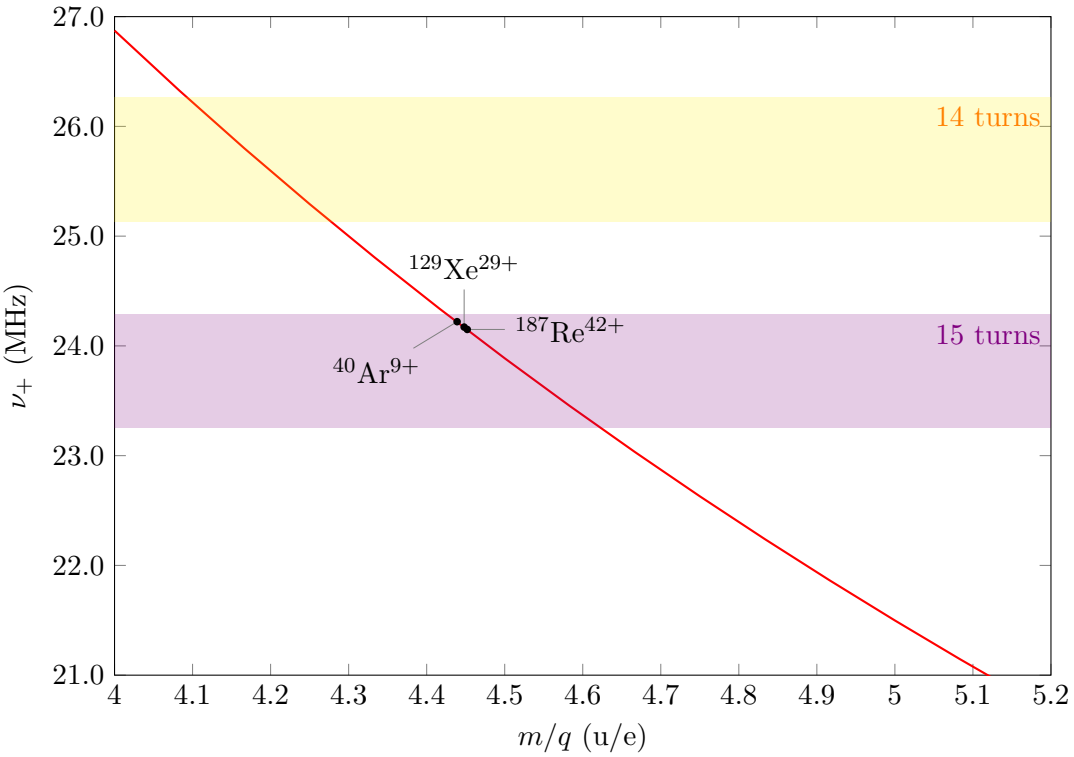


**Figure 4.7:** Modified cyclotron frequency for different mass-to-charge ratios. The axial frequency is assumed to be 600 kHz and the magnetic field strength is 7 T. The $^{40}Ar^{9+}$-ion will be used to commission PENTATRAP, while $^{129}Xe^{29+}$ and $^{187}Re^{42+}$ are planned for a first measurement. The shaded areas correspond to frequency regions which are accessible with a cyclotron resonator coil with 14 or 15 turns connected to the amplifier, trap and the varactor diode.

The amplifier is mounted inside a separate chamber on the lid of the resonator housing and therefore perpendicular to the magnetic field. A magnetic field flowing through the GaAs FETs has an effect on the gate bias [Rou12]. In order to circumvent possible problems due to pinch off the FETs were soldered perpendicular to the board. The varactor diode was mounted on a separate board and screwed onto the lid of the amplifier box.

Fig. 4.7 shows the modified cyclotron frequency as a function of the mass-to-charge ratio of the ion and the respective frequencies of possible candidates for PENTATRAP version 1.6. The modified cyclotron frequency (Eq. (2.8)) was calculated for a magnetic field of 7 T and an axial frequency of 600 kHz. For the case of a coil with 14 and 15 windings the resonance frequency regions accessibly by tuning the varactor diode are marked in colour.

The cabling between the resonator, amplifier and trap also has an effect on the resonance frequency. Especially the connecting cables between the trap and the resonator will be different in the final setup of PENTATRAP, leading to a parasitic capacitance which can not be estimated beforehand. The effect on the resonance frequency is therefore not predictable. The decision for the final number of turns for the cyclotron resonator will be made during the assembly of PENTATRAP version 1.6.

## 4.4 Design Requirements for the new Detection System

In Fig. 3.5 one measurement scheme for PENTATRAP using only trap 2, 3 and 5 was shown. In principle it is possible to use each of the five traps for ion cooling and frequency measurements. In order to have maximal flexibility in the measurement schemes the new resonators were designed in a way that the resonator chamber can house five cyclotron and five axial resonators, one of each for every trap.

The housings for the axial and the cyclotron resonators will be identical. This has the following advantages:

- Exchangeability: it is easy and fast to exchange the housing or resonators during the setup of the experiment
- Positioning: Every resonator can be put in every place in the resonator chamber.

The variable positioning of the resonators is important for two reasons. The axial resonators are wound with superconducting NbTi wire. As explained in Sec. 4.1.3 losses in a type II superconductor scale with the external magnetic field strength. It is therefore advantageous to put the axial resonators in a lower magnetic field region, for example the bottom of the resonator chamber.

For the cyclotron resonators the length of the wire is approximately 0.5 m. The distance from the resonator position to the trap is on the same order. The parasitic capacitances and inductances scale with the length of the cable. In order to reduce this effect, the cyclotron resonators are put at the top of the resonator chamber, thereby decreasing the cable length to $\approx 0.2$ m.

If both resonators have the same housing the position of the amplifier box for the cyclotron resonator needs to change. The new version of the resonators will have the amplifier box for both the axial and the cyclotron resonators at the side of the housing. In order to assure good ground connection of the amplifier its box will be made out of one part of copper together with the resonator housing.

Different materials are used to build the resonators, see Tab. 4.1. The housing itself as well as the wire for the cyclotron resonators are made out of copper, the coil body and the holders of the coil are made of PTFE and the wire for the axial resonator is NbTi with PTFE insulation. The resonators are assembled at room temperature and then cooled down, either in the cryocooler for test measurements or in the magnet. Therefore, their different behaviour with regard to temperature has to be taken into account. In Fig. 4.8 the changes in length for a given temperature normalised to the length at 293 K for

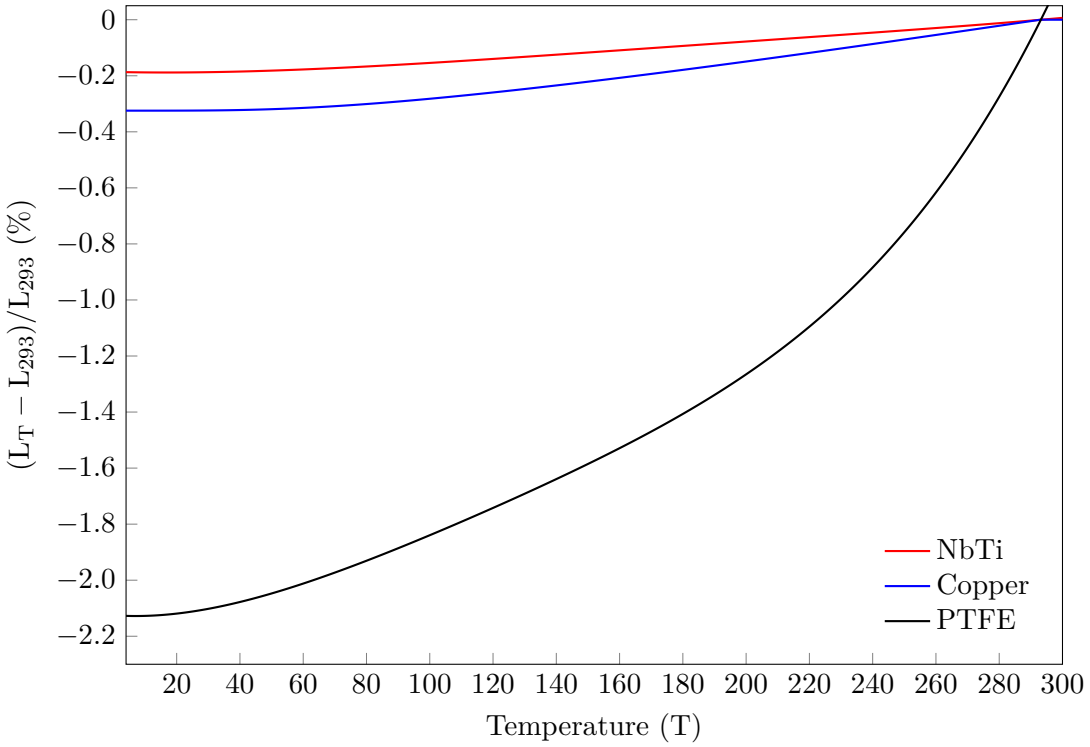


**Figure 4.8:** The temperature behaviour of the three materials used for the resonators is plotted. The length difference of a material at a given temperature to the length at 293 K normalised to the length at 293 K is shown. NbTi and copper have a very similar temperature behaviour while PTFE shrinks about ten times more. This leads to problems while cooling down the resonators. Data taken from [SU92] (copper), [CG61] (PTFE) and [MLR02] (NbTi). The last reference also lists data for PTFE, which is in good agreement with [CG61].

NbTi, copper and PTFE is shown. With a decrease of $\sim 2.2\%$ PTFE shrinks about ten times more than copper and NbTi when it is cooled down to 4 K. Since PTFE is used for the coil body and the holders inside the housing, special care has to be taken to ensure that they do not become loose during the cool down process. In the previous resonator design this was not a problem for the cyclotron resonators, as the coil body itself was connected to the bottom of the housing with a screw and the coil wire was fixed with PTFE onto the coil body. The holders of the axial resonator pressing onto the spacer structure were fixed down by the use of set screws. This required additional holes in the lid and therefore lead to more imperfections and more dielectric materials in the housings. These problems are overcome in the new design by a new pressing system which is used to fixate the coils. This will be discussed in the following.

## 4.5 Design - Resonator Housing

The new resonator chamber will hold ten resonators, arranged in two towers. A model of the final resonator chamber below the trap tower can be seen in Fig. 4.9. For first tests of the resonator design with the new coils a test setup consisting of a tower with only two resonators, one axial and one cyclotron, was built.

Fig. 4.10 shows a drawing of the test setup and a cross-sectional view looking into the amplifier boxes. In order to test it under working conditions the test setup is fitted with an adapter plate to mount it inside the cryocooler. The mounting of the resonators is identical to that of the final setup. A picture of the test setup mounted in the cryocooler can be seen in Fig. B.2.

The crucial difference to the previous resonators is the holding and pressing system of the resonators. As can be seen in Fig. 3.3 both lids for the previous resonators were connected via screws to the housing. Since both coil types are now toroidal, the problem of proper fixation of the coil at cryogenic temperatures arises also for the cyclotron resonators. Using screws to press the coils in their position would require space between the housings and also introduce more imperfections in the housing for the cyclotron resonators.

The main idea for the new pressing system was to use the lid to fix the coils. This works as follows: The bottom of the upper resonator housing will serve as a lid for the resonator below. The upper part of each housing is therefore broadened leading to the formation of a step, while the lower part is narrowed, see Fig. C.2. The inner height of the housing is defined as the length from the bottom up to the step (40.8 mm). Fig. 4.10 also shows an enlarged view of this step.

In the cross-sectional view the coil and the holders are missing. The holders of the coil are designed such that the overall height of the PTFE parts (coil and holders) are larger (by 2.2%) than the inner height of the resonator housing. While assembling the resonator at room temperature the slit at the step will be there when the upper resonator simply sits on the PTFE parts of the lower resonator. The PTFE parts are squeezed until the upper resonator sits on the step of the lower one, leading to a ground connection between the two housings. This is achieved by tightening the screw on top of the resonators, thereby pressing them together. While cooling down the squeezing force on the PTFE parts will decrease as they shrink until at 4 K the height of the PTFE parts is equal to the inner height of the resonator. Therefore, the coil will still be fixed at 4 K.

The amplifier box for both types of resonators is now positioned at the side of the housing. Perfect ground connection is ensured by making the amplifier box and the housing out of one piece of copper.

In order to further reduce parasitic capacitances and cable lengths, the coil wire enters the amplifier box directly from the resonator housing. The grounding of the cold end of the coil will also be done on the amplifier board. Thereby no additional dielectric material, for example a soldering eyelet, is needed inside the housing. The axial resonator has three holes into the amplifier chamber: one for the cold end to be grounded, one to

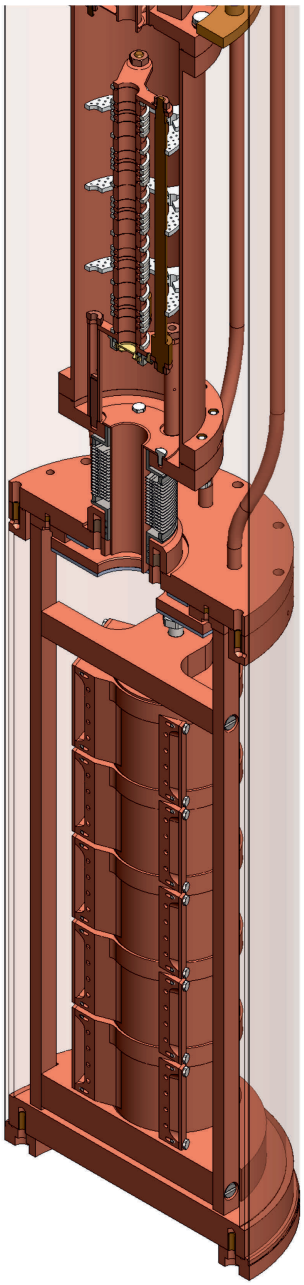

**Figure 4.9:** Cross-sectional view of the resonator chamber below the trap tower in PENTATRAP version 2. The resonator tower consists of five resonators, which are pressed together with a screw. Capillaries are used to guide the cables for the supply voltages into the resonator chamber.

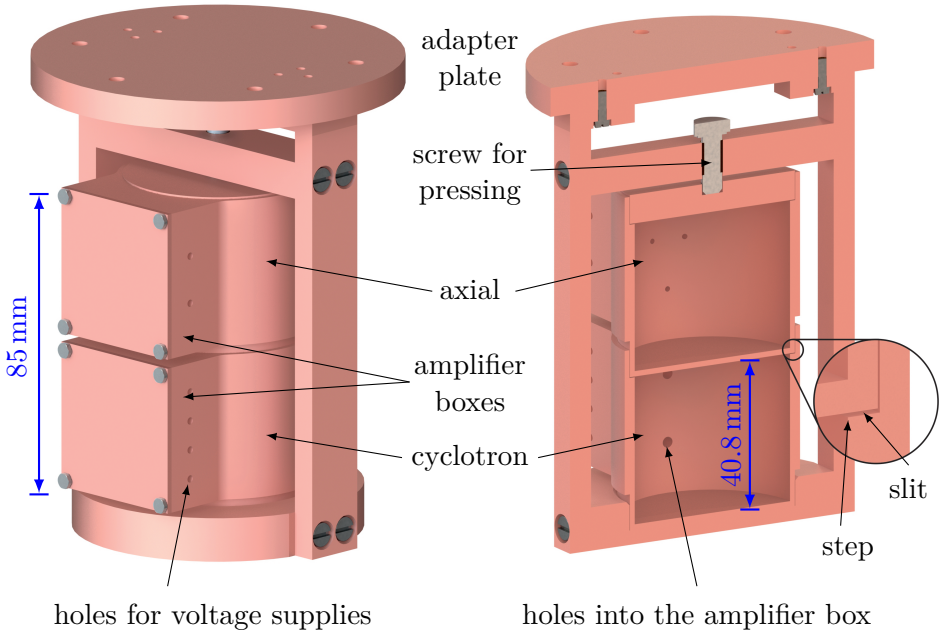


**Figure 4.10:** Rendered schematic of the test setup for the new design of the resonators. The coils and the holders for the coils are not shown. For a cross-sectional view of a housing and the coil body see Fig. 4.11 and Fig. 4.23.

connect the amplifier to the tab and one for the hot end, which will leave the amplifier box to be connected to the trap electrode. The cyclotron coil only has a hot and cold end, but requires a larger diameter of the holes for the wire to fit through.

The position of the two towers in the final setup is defined by a circular dent with the same diameter as the lower part of the resonator in the bottom plate of the pressing system. The lid for the topmost resonator is a plate with the same dimensions as the bottom of the resonator.

## 4.6 Axial Resonators

### 4.6.1 Design

The axial coil body is made out of two halves of a torus which are connected with small PTFE rods. Winding starts on one half, the second half will be attached rotated by 180° with respect to the final position and wound. The last step is rotating the two halves to form a torus.

Compared to the previous coil body the following improvements were made:

- Spacers: While the spacers on the outside of the coil body (see Fig. 3.3 and Fig. 4.2) make it easier to wind the coil by providing chambers, this effectively disrupts an even distribution of the wire and might interfere with the confinement of the

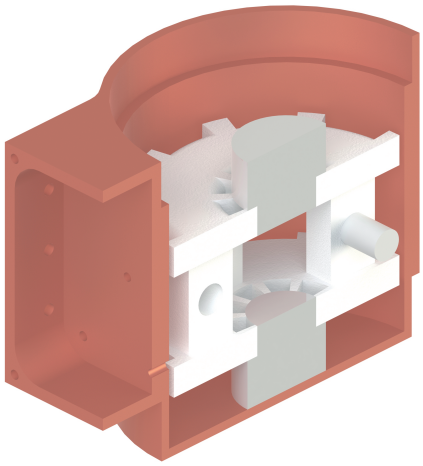

| | value |
|---|---|
| height | 25 mm |
| inner radius $r$ | 9.5 mm |
| outer radius $R$ | 21 mm |
| outer PTFE radius | 23 mm |
| angle covered by one spacer | 10° |

**Figure 4.11:** Left: Rendered schematic of an axial resonator cut in half. The rod is used to connect the two halves of the coil body. In order to distinguish the holders from the coil body, they are shown in a darker colour. Right: Dimensions of the axial coil body. A picture of the axial resonator is shown in Fig. B.1.

magnetic flux inside the coil. The total angle covered by the spacer structure on the outside was reduced from 123° to 100°. In order to make the winding even easier a spacer structure was also implemented on the inside of the coil body. This fixes the wires in their chamber and was especially important for the winding of the outer chambers of one half torus.

- Amount of dielectric material: The PTFE used for the coil body and its holders leads to dielectric losses. The coil body is now made out of two plates of PTFE which define the geometry of the coil. They are held together by spacers in between. These spacers are also used to connect the two halves of the torus. The holder for the coil, in the previous design a ring pressing on the outer spacers, is now realised by a rod pressing on the inner spacers.

Fig. 4.11 shows a cross section of the 3D model of the resonator and the dimensions of the coil. The spacers are set back from the edge of the PTFE plates to assure a perfect torus.

In order to reach the same resonance frequency for the new resonators as for the previous ones the inductance and capacitance should stay the same. Since for a toroidal coil the magnetic flux is nearly completely confined inside the coil the size of the housing does not effect the inductance to first order approximation.

The inductance of a toroidal coil with $N$ windings, a cross-sectional area $A$ and a mean radius $r_m = (R + r)/2$, with $R$ the outer and $r$ the inner radius, is [LF15]:

$$L \propto N^2 \frac{A}{r_m} \quad . \tag{4.25}$$

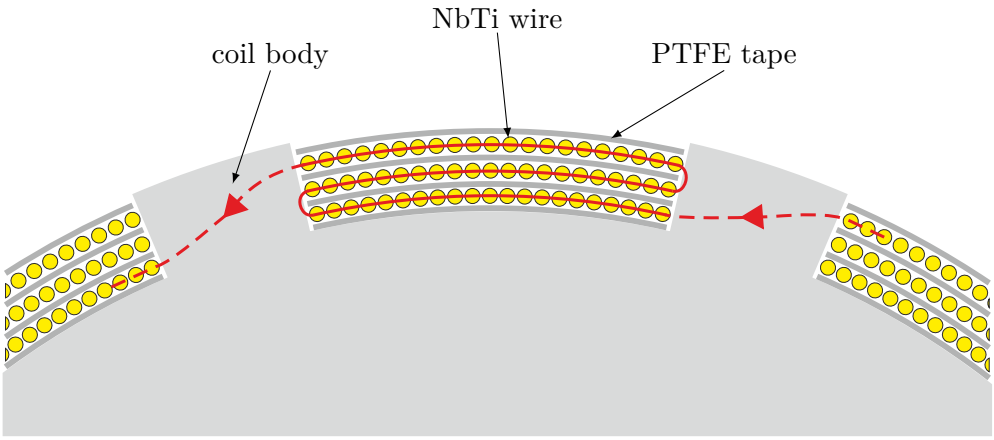


**Figure 4.12:** Sketch of a cross section of the axial coil body with an ideal winding (not to scale). A first layer of PTFE tape is wound around the coil body to ensure thermal contact with the innermost layer of NbTi wire.

For a given $L$ the number of windings squared is proportional to the mean radius and antiproportional to the cross-sectional area $A$. The length of the wire is proportional to the number of windings and the square root of the cross-sectional area. The axial coil wire is made out of superconducting NbTi. Sharp kinks or parts which are not thermalised can be non-superconducting. Therefore, reducing the wire length or rather the cross-sectional area or the number of windings reduces the probability of non-superconducting wires.

In order to decrease the number of windings the outer diameter $R$ is chosen to be as large as possible. With a distance of 3 mm to the wall of the resonator housing the outer radius is $R = 21\,\text{mm}$. The inner radius ($r = 9.5\,\text{mm}$) was chosen as small as possible while still leaving room for the spacers and the holders. The height is $h = 25\,\text{mm}$.

Keeping the inductance constant, an approximation of the number of windings for the new resonator can be made by comparison to the previous geometry and using Eq. (4.25):

$$N_{\text{new}} = N_{\text{old}} \cdot \sqrt{\frac{A_{\text{old}}}{r_{\text{m,old}}} \cdot \frac{r_{\text{m,new}}}{A_{\text{new}}}} = 710 \quad , \tag{4.26}$$

with the dimensions for the previous geometry given in Tab. 4.2 and $N_{\text{old}} = 800$.

The parasitic capacitance is kept low by using a chamber winding, where the wire is wound in layers inside the chamber (see Fig. 4.12). The cross-sectional area $A$ for the inner winding is defined by the geometry of the coil body. The outmost layer has a larger outer and a smaller inner radius. The PTFE tape used to separate the layers is too wide for the inner chamber and needed to be folded, leading to a larger decrease in the radius in the middle than an increase on the outside. This results in a higher inductance of a multilayer winding compared to a single layer coil.

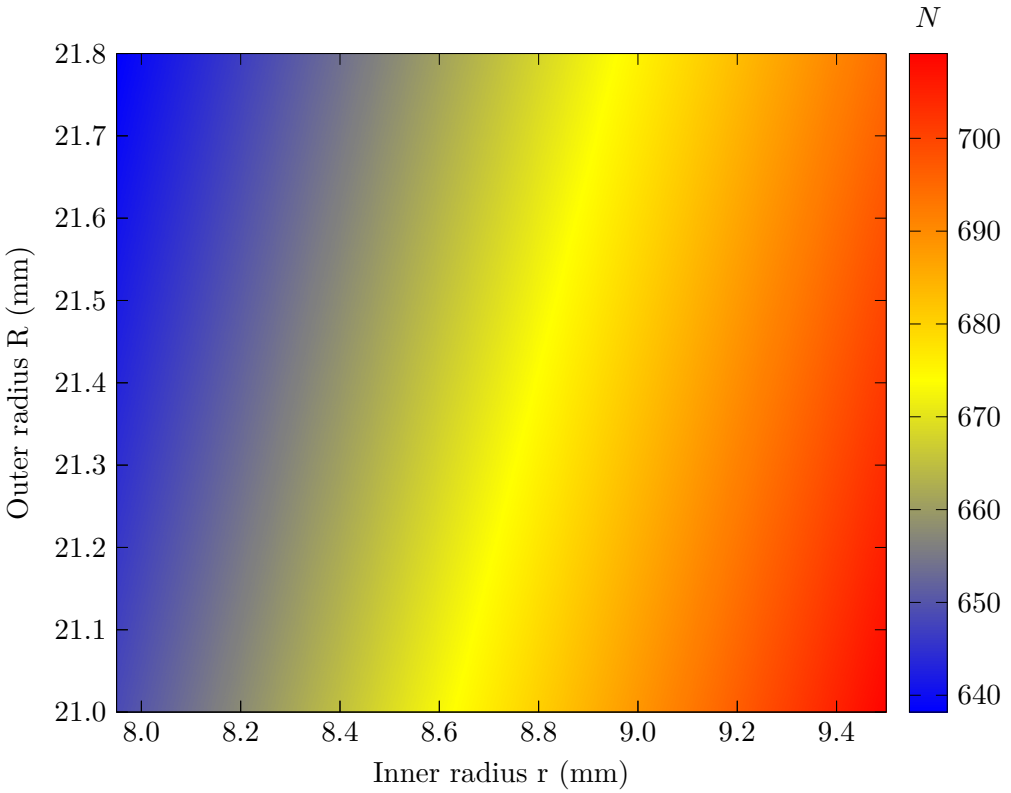


**Figure 4.13:** Shown is the number of windings $N$ needed for different radii of the new axial coil body to reach the same inductance as the previous resonator. Due to the chamber winding not every part of the wire sits on the coil body, leading to a larger cross-sectional area for the outer layers. With three layers of windings and three layers of PTFE tape the distance between the outer wires and the coil body was about 1.0 to 1.5 mm.

The change in the number of windings needed for a given inductance is shown in Fig. 4.13, where the change in radii is shown for all layers. The NbTi wire has a diameter of $\sim 0.16$ mm (with insulation), the PTFE tape is 0.075 mm thick. This together leads to an increase of 0.7 mm on the outer and of $\sim 1$ mm on the inner radius. The same effect also happens on the top and bottom, leading to an additional increase in cross-sectional area.

In the previous version the coil body was solid with a hollow on the inside of the torus to reduce the amount of PTFE. The edges were rounded (see Fig. 4.2). The PTFE parts for new resonator were made on the MPIK milling cutter *LPKF* ProtoMat S103 [Ele]. The cross-sectional area is very close to a rectangle, see Fig. C.3. A higher capacitance compared to the previous version arises from the outer edges, as the wire in this region is closer to the housing than in the previous resonators. The total capacitance is therefore expected to be higher.

In order to counteract the higher inductance for a given number of windings by using a chamber winding and the expected higher capacitance compared to the previous resonator the number of turns were chosen to be 600 with 60 turns per chamber. These 60 turns were divided into three layers to keep the potential difference between two neighbouring wires as small as possible.

Fig. 4.12 shows a sketch of the axial coil body with the wire inside the chamber. The placement of the wire is shown as ideal. In reality the distance between the windings of one layer was larger on the outside, as the length of an outer chamber (9.53 mm) is large enough for twenty wires with a diamter of 0.16 mm. Placing the windings on the inside was more difficult as the arc length of the chamber is about the same as $20 \cdot 0.16\,\text{mm}$. The inner radius was therefore even further decreased, as windings had to be put on top of each other.

The wire is only held by the two PTFE plates. In order to ensure a good thermalisation for every part of the wire a first layer of PTFE tape is wound around the naked coil body. This also softens any possible sharp edges from rounding the plates. Further, every layer is separated by PTFE tape to press the windings onto the coil body.

### 4.6.2 Performance

The measurement errors discussed in the following do not represent the uncertainty of the specified measurement. Instead they do represent the uncertainty in the reproducibility of the setup. Since the setup for the measurement by means of capacitive coupling between the network analyzer and the resonator is less reproducible compared to a measurement with the resonator soldered to the amplifier the uncertainties of these measurements are considerably higher.

**Free Resonance Frequency** For a measurement of the free resonance frequency the inner conductor of one of the cryogenic coaxial cables inside the cryocooler is guided through one hole into the resonator housing. The resonator is excited through this cable. Both ends of the coil are guided through the second and the third hole. The cold end is then soldered to an eyelet and screwed to the housing, while the second cryogenic cable is capacitively coupled to the hot end by fixing it with PTFE tape. The spatial separation of the excitation and the measurement cable avoids crosstalk between the two.

A crucial point during the measurement with the axial resonators was the fixation of the coil and the electrical connection between the housing and the lid. For the first measurement presented in Fig. 4.14, two potential problems were identified. First of all, the holders of the coil were too short, such that the coil was vibrating with the beat of the cryocooler, leading to distortions of the resonance. Second, it was suspected that simply pressing the lid onto the housing did not provide a proper electrical connection between the two with a sufficiently low resistance. The fit of the function given in Eq. (4.22) to the data yields a resonance frequency of $\nu_0 \approx 1.04978\,\text{MHz}$ and a quality factor of $Q \approx 8000$.

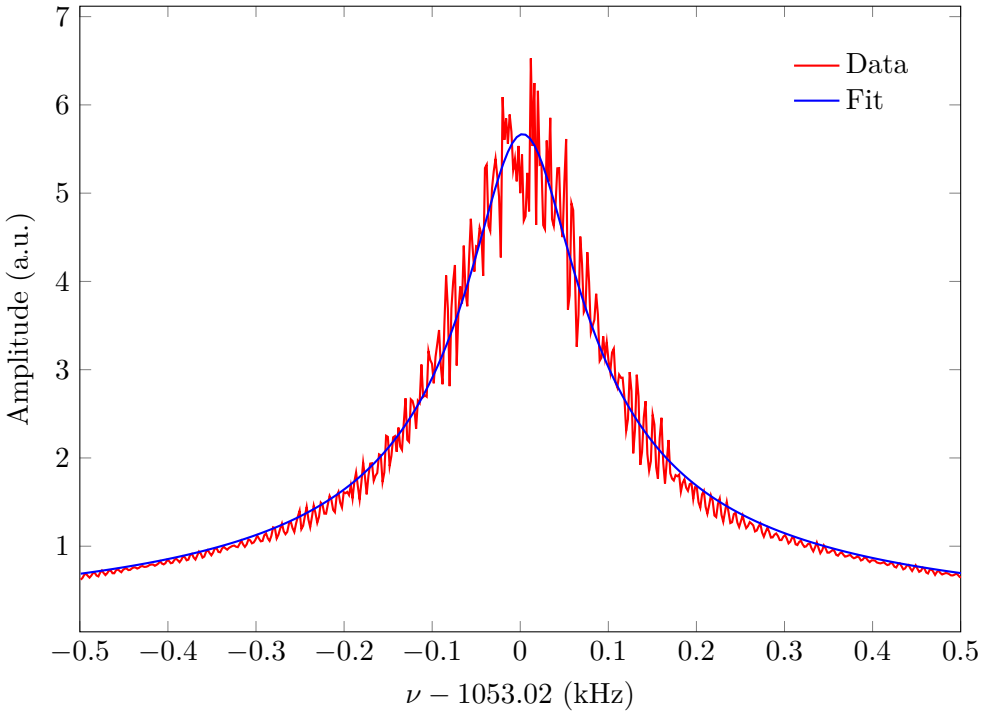


**Figure 4.14:** Measurement and fit of the resonance curve of the axial resonator with a loose coil and a poor electrical connection between the lid and the housing. Due to these imperfections the $Q$-value was lower than expected. The spectrum was averaged ten times and the measurement bandwidth was 100 Hz. This resulted in $Q_{\text{fit}} \approx 8000$ and $\nu_{\text{fit}} \approx 1.0478\,\text{MHz}$.

The PTFE holders were self made on the lathe and did not feature the exact height needed. For the next measurement several layers of PTFE tape were pressed on top of both holders, thereby increasing the height. In order to improve the electrical connection between the lid and the housing small pieces of copper were pressed in between.

The result of these measures is shown in Fig. 4.15. The fit describes the data very well. The difference in resonance frequency between the first and the second measurement arises from the different couplings to the coaxial cables.

The resonance curve of this setup was recorded six times with varying frequency span. While the fit gave no difference in the resonance frequency, the $Q$-value was not identical for every measurement. Taking the mean and the standard deviation of the six measurements results in a $Q$-value of 27500(300).

For a third measurement the resonator was pressed even tighter to further increase the connection between the lid and the housing. This resulted in a resonance frequency of $\nu_0 = 1.047\,\text{MHz}$ and a $Q$-value of 33600(500).

The error of the fit is tiny compared to the error resulting from different measurement setups. Therefore, the error of the free resonance frequency can be taken as the standard

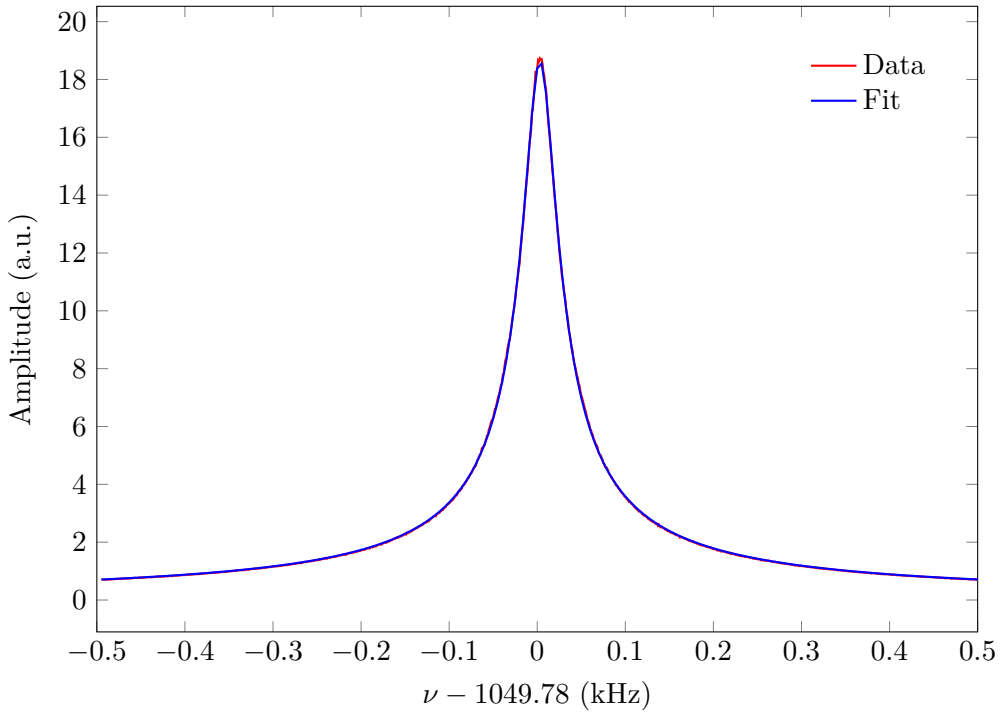


**Figure 4.15:** Measuremet and fit of the resonance curve of the axial resonator for the second measurement setup. Compared to Fig. 4.14 the pressing of the coil as well as the housing were improved. The spectrum was recorded with a measurement bandwidth of 10 Hz. The fit to the data resulted in: $Q_{\text{fit}} = 27660$ and $\nu_{\text{fit}} = 1.050\,\text{MHz}$.

deviation of the three measurement setups mentioned above. This gives a free resonance frequency of

$$\nu_{0,\text{free}} = 1050(3)\,\text{kHz} \tag{4.27}$$

and a maximal $Q$-value of 33600(300) for the free axial resonator.

**Determination of the Inductance and Capacitance** For the determination of the inductance and the capacitance of the resonator the resonance frequency was determined with and without a capacitance connected in parallel to the coil. By knowing this capacitance it is then possible to calculate the inductance and capacitance of the resonator.

In order to minimise the effect of the additional capacitance on the $Q$-value a capacitance with a high $Q$-value is needed. Since the Penning trap is machined very precisely and the only dielectric material is sapphire, the hot end of the coil was attached to the end electrode of a test trap. The capacitance of electrode and the cabling are taken to be 18(2) pF, where the trap capacitance is taken from [Rou12]. The large error arises from the unknown cable length and capacitance.

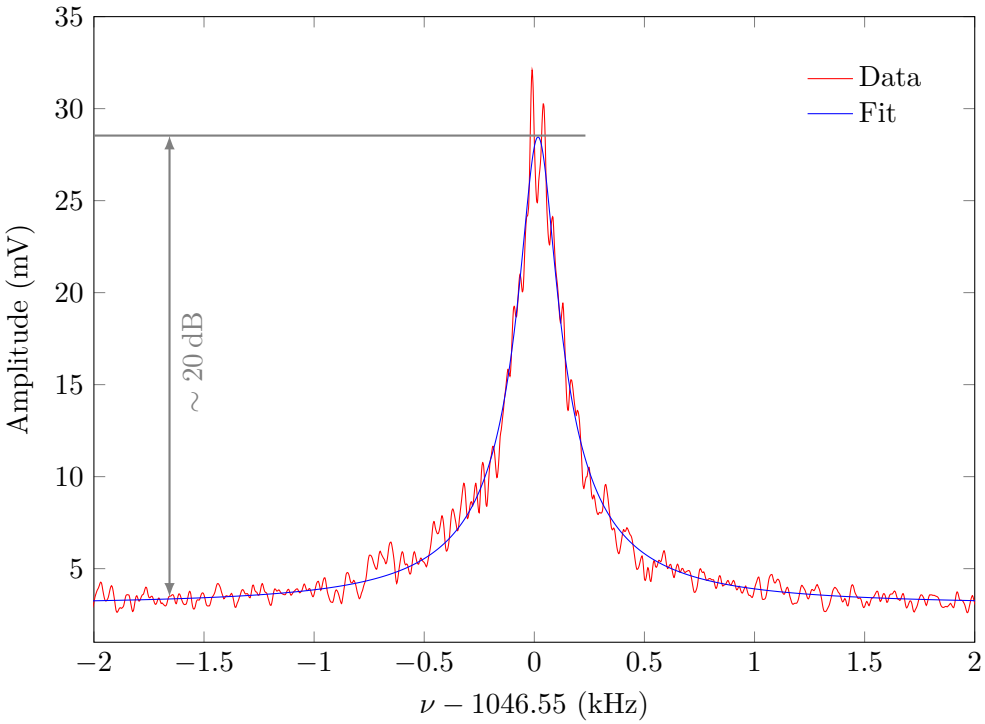


**Figure 4.16:** Noise resonance of the axial resonator connected to the amplifier. The gate voltages of the amplifier were $U_{g1} = -0.69\,\mathrm{V}$ and $U_{g2} = -0.68\,\mathrm{V}$.

Three measurements were done, again with different spans. The resonance frequency was measured to be:

$$\nu_{0,\mathrm{trap}} = 662630(1)\,\mathrm{Hz} \quad . \tag{4.28}$$

The error is again given by the statistical uncertainty of the fit results. However, the error of the resonance frequency should not be described by the standard deviation. To that end a conservative estimate of the uncertainty of 3 kHz is done as above.

The resulting inductance and capacitance of the resonator are:

$$C_{\mathrm{axial}} = 11.91(0.13)\,\mathrm{pF} \quad , \tag{4.29}$$

$$L_{\mathrm{axial}} = 1.93(0.21)\,\mathrm{mH} \quad . \tag{4.30}$$

As expected the capacitance is higher than in the previous axial resonator (see Tab. 4.2), resulting from the decreased distance of the coil's wire to the resonator housing. The inductance might be decreased by a mutual inductance of the housing and the coil due to this smaller distance.

**Coupled Performance of Amplifier and Resonator** For a first test of the amplifier with the resonator a tab is not used. Instead the resonator is capacitively coupled to the amplifier with 0.3 pF. A measured noise spectrum is shown in Fig. 4.16.

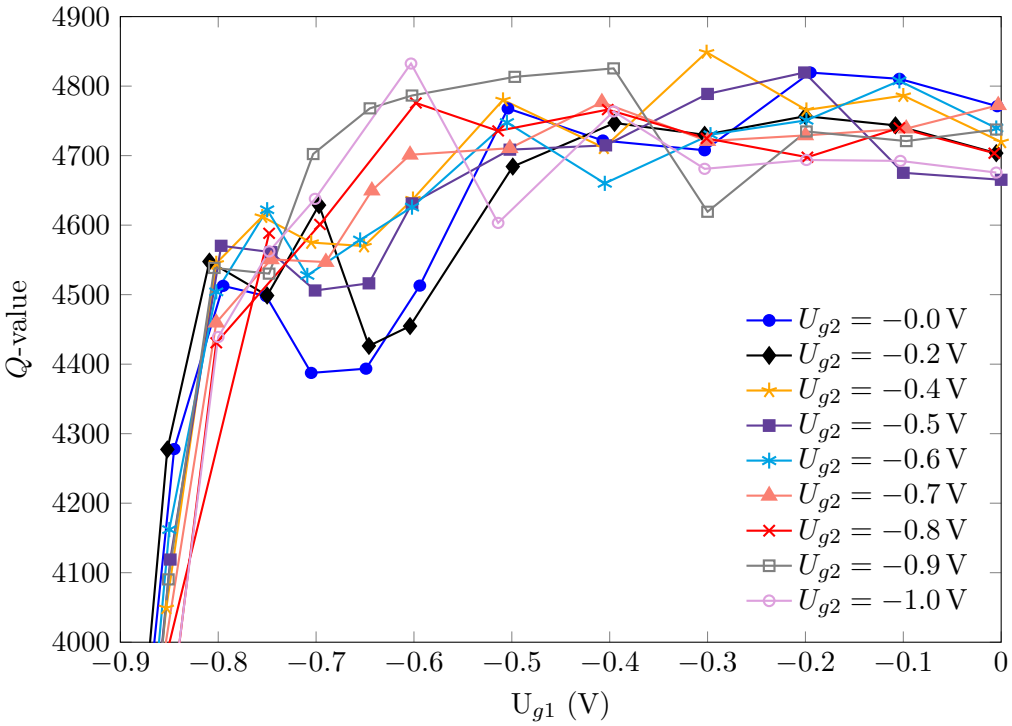


**Figure 4.17:** $Q$-value of the axial resonator connected to the amplifier for different gate voltages. The resonance curve for each voltage setting was averaged 10 times and fitted afterwards to determine the $Q$-value.

The $Q$-value of the coupled system depends on the gate voltages of the amplifier. In the following the gate of the common source FET in the cascode is denoted as gate 1, while the gate of the common gate stage is gate 2. Fig. 4.17 shows the dependence of the $Q$-value on the gate 1 voltage for different gate 2 voltages. The voltage gain of the amplifier was measured for the same gate voltages and is shown in Fig. 4.18. For this measurement the resonator was disconnected from the amplifier.

Independent of $U_{g2}$ the $Q$-value is maximal for gate 1 voltages more positive than $U_{g1} = -0.5\,\mathrm{V}$. At lower gate 1 voltages the gain of the amplifier rises to its maximum while the $Q$-value decreases. This can be explained by the parasitic feedback from the amplifier onto its input and thereby the resonator. This effect is maximal for $U_{g1} = -0.7\,\mathrm{V}$ where also the highest amplifier gain can be reached.

For a well set-up cascode the back action onto the resonator can be reduced or even vanishes. For $U_{g2} = -0.9\,\mathrm{V}$ and gate 1 voltages between $-0.75\,\mathrm{V}$ and $-0.5\,\mathrm{V}$, where the gain has its maximum, the $Q$-value only has a weak dependence on the amplifier gain. This is due to the suppressed Miller effect in this configuration.

When choosing the right bias voltages a compromise between a high $Q$-value and a large amplifier gain has to be made. In this case, one possiblity would be to choose $U_{g1} = -0.6\,\mathrm{V}$ and $U_{g2} = -0.7\,\mathrm{V}$. There, the gain is about 5 dB and the $Q$-value is 4700.

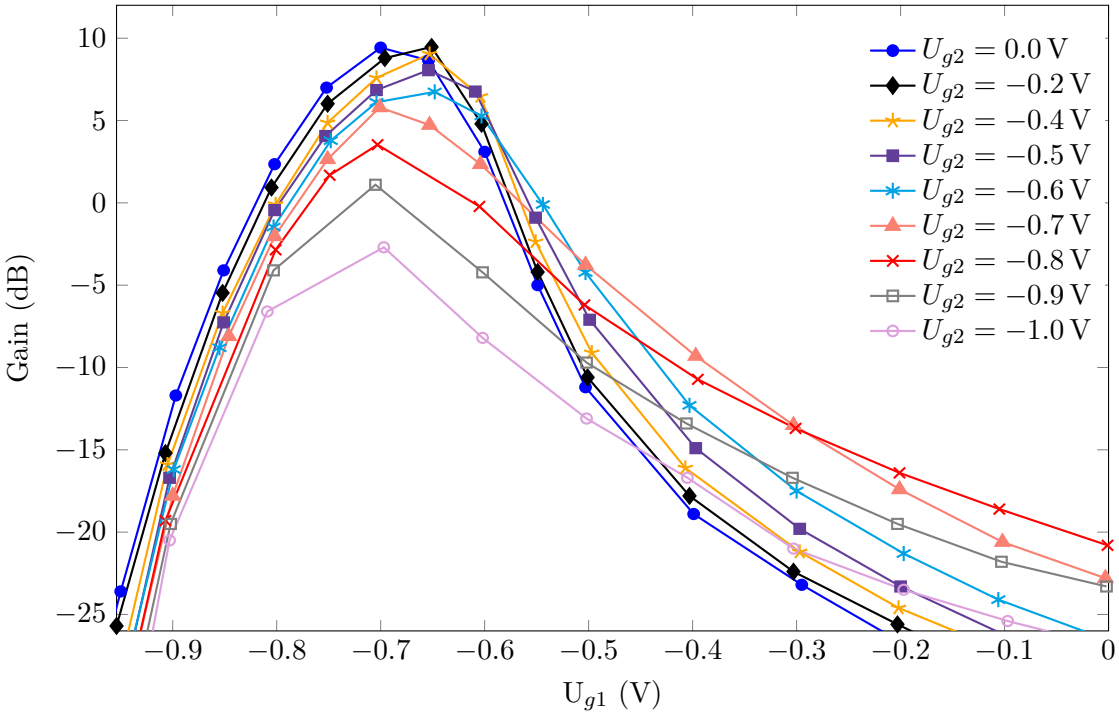


**Figure 4.18:** Voltage gain of the axial amplifier for different gate 1 and gate 2 voltages. The coil was disconnected from the amplifier and the amplification was estimated for a frequency region of 0.1 to 1.5 MHz. The errors arising from fluctuations over this frequency range and the errors of the gain voltages are smaller than the marks.

The dipwidth in the dip detection measurement can now be calculated exemplarily. The parallel resistance of the detector is given by

$$R_P = Q\omega L \approx 38.53\,\mathrm{M\Omega} \quad , \tag{4.31}$$

with a $Q$-value of 4800. For a $^{35}Cl^{10+}$-ion and an effective electrode distance $D_{\mathrm{eff}} = 12.5\,\mathrm{mm}$ the dipwidth on resonance, defined in Eq. (2.27), is then:

$$\Delta\nu = \frac{q^2 R_P}{2\pi m D_{\mathrm{eff}}^2} \approx 1.73\,\mathrm{Hz} \quad . \tag{4.32}$$

This dipwidth of 1.73 Hz is very close to the ideal dipwidth of 1 Hz, see Sec. 2.2.3, and therefore sufficient for first tests with PENTATRAP version 2.

## 4.7 Cyclotron Resonators

Possible ion candidates for PENTATRAP version 2 are $^{28}Si^{8+}$, $^{35}Cl^{10+}$ and $^{36}Cl^{10+}$. In contrast to the axial case the resonance frequencies of the cyclotron resonators have to

match the modified cyclotron frequencies of the ion, which depend on the charge-to-mass ratio. The ions mentioned above have a modified cyclotron frequency between 29.9 and 30.7 MHz. Since it is challenging to design a resonator whose resonance frequency exactly matches the modified cyclotron frequency, a varactor diode is added to the input of the amplifier. The capacitance of the varactor diode changes with the applied voltage and allows for a fine tuning of the resonance frequency of the resonator. For more information see chapter Sec. 4.2.

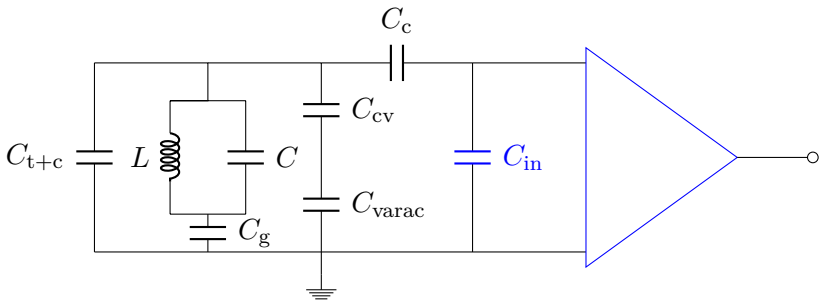


**Figure 4.19:** Circuit diagram of a cyclotron resonator connected to the amplifier, varactor board and trap. Relevant for the determination of the resonance frequency of the coupled system are only the capacitances and the inductances. Blue marked is the input capacitance of the amplifier and the amplifier itself. For a description of the variables see Tab. 4.3.

Connecting the amplifier, varactor diode and trap to the resonator changes its free resonance frequency $\nu_{0,\text{free}}$ to a lower frequency $\nu_{0,\text{final}}$, which has to be equal to the modified cyclotron frequency of the ion. In order to estimate the needed $\nu_{0,\text{free}}$ one can use the circuit diagram shown in Fig. 4.19. The resonator is represented by $L$ and $C$. The amplifier is represented by its input capacitance as this has an effect on the resonance frequency. The description and the values for the rest of variables are given in Tab. 4.3.

The cyclotron resonator is connected to a segmented ring electrode, which has a capacitance of 8 pF [Rou12]. Possible changes to the resonance frequency due to the different cabling in the final setup in PENTATRAP are taken into account by an error of the combined trap and cable capacitances of 3 pF.

The resonance frequency of the whole setup shown in Fig. 4.19 can be determined by calculating the total impedance $Z_{tot}$ and solving $1/Z_{tot} = 0$ for the frequency

$$\omega_0 = \sqrt{\frac{C_c \cdot [C_{t+c}C_v + C_{cv}C_{varac} + C_vC_g] + C_{in} \cdot [C_cC_v + C_{t+c}C_v + C_{cv}C_{varac}]}{L \cdot ([C_c + C_{in}] \cdot [C_{res}\,(C_{cv}C_{varac} + C_vC_{t+c}) + CC_vC_g] + C_{res}C_{in}C_cC_v)}}\,, \tag{4.33}$$

where the parameters $C_v = C_{cv} + C_{varac}$ and $C_{res} = C_g + C$ are used to simplify the equation. Knowing the inductance $L$ and the capacitance $C$ of the resonator Eq. (4.33) can be used to estimate the final resonance frequency $\nu_{0,\text{final}}$.

**Table 4.3:** Description and values for the variables used in Fig. 4.19. The capacitance of the varactor diode depends on the voltage applied to it.

| Description | | Value |
|---|---|---|
| Capacitance to ground | $C_\mathrm{g}$ | 3 nF |
| Coupling capacitance btw varactor board & amplifier | $C_\mathrm{cv}$ | 2.2 pF |
| Coupling capacitance btw amplifier & resonator | $C_\mathrm{c}$ | 0.3 pF |
| Capacitance of varactor | $C_\mathrm{varac}$ | 1 . . . 8 pF |
| Input capacitance of amplifier | $C_\mathrm{in}$ | 1 pF |
| Cable and trap capacitance | $C_\mathrm{t+c}$ | 15(3) pF |

In the first section of this chapter the design process for the coil body with the help of Eq. (4.33) will be explained. The next section will then discuss the performance of the final geometry with and without the amplifier and the varactor.

### 4.7.1 Design

Before the start of this thesis no toroidal cyclotron resonators were in use in any experiment. In order to familiarise oneself with the new geometry and the effects of the housing a test coil body was manufactured. The outer radius (18 mm) of the body was chosen to leave enough room (8 mm) between the coil body and the housing. The inner circumference is large enough to be able to place 20 windings of a 1 mm wire with a distance of 1 mm in between, leading to a radius of about 6.5 mm. At the top and the bottom of the coil the 20 windings are separated by spacers. A picture of the coil body can be seen in Fig. 4.20.

In order to be able to wind the coil more easily a slit was made in the middle, see Fig. 4.20. This idea proved to be wrong as there was no possibility to fix the wire and several windings tended to slip through the slit during the winding process. Also, the first and last winding, placed on either side of the slit, were either deformed or had to be left out.

Another difficulty arose from the curvature of the wire. As seen in Fig. 4.20 the wire is bent towards the center on the inside and towards the housing on the outside. It lies flat on the coil body only at the bottom and the top. Especially in the center of the torus the wire had to be positioned carefully to keep the adjacent windings from touching.

The resonance frequency of a coil wound this way with 19.5 windings is

$$\nu_0 \approx 49\,\mathrm{MHz} \tag{4.34}$$

with an inductance $L \approx 2.7\,\mu\mathrm{H}$ and a capacitance $C \approx 3.9\,\mathrm{pF}$. At cryogenic temperatures typical $Q$-values of 3100 were found.

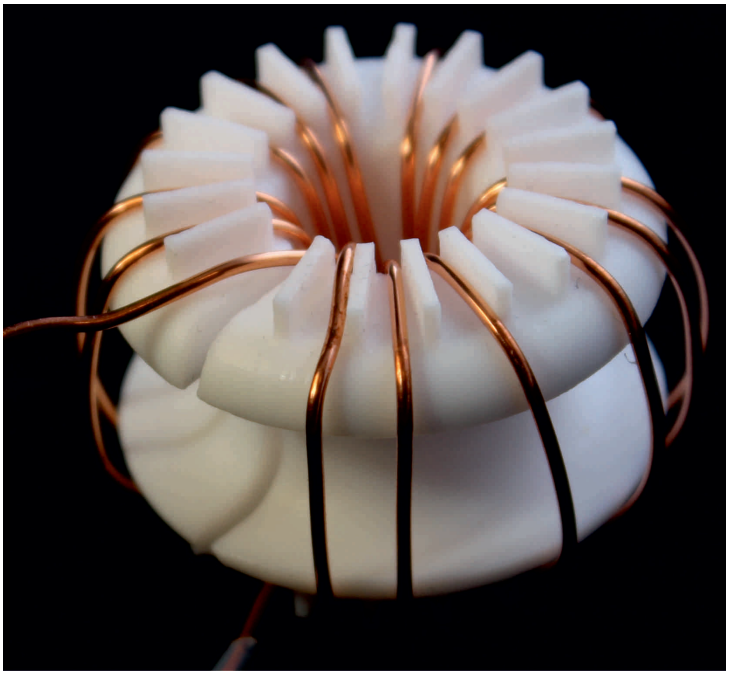

**Figure 4.20:** Picture of a first test coil for the cyclotron resonator. The wire is held in place with spacers on the top and the bottom. The amount of PTFE is reduced by a cut on the outside. The slit into the middle of the coil was designed to make winding easier. For this coil type the wire is straight on the top and bent on the side and in the middle.

Using the values given in Tab. 4.3 and Eq. (4.33) the resonance frequency of the whole system is on the order of

$$\nu_0 \in [10.33, 10.69]\ \text{MHz} \quad , \tag{4.35}$$

depending on the value of the varactor diode.

The modified cyclotron frequency for $^{35}Cl^{10+}$ is given in Fig. 2.2 and is $\approx 30.69\,\text{MHz}$. The free resonance frequency therefore has to be higher in order to end up with a higher resonance frequency of the whole system. It is easier to control the inductance than the parasitic capacitance of the resonator. Therefore, the inductance has to be decreased, ideally in a way also leading to a decrease in the capacitance.

The inductance can be reduced by decreasing the number of windings or the cross-sectional area. The capacitance depends on the difference in electrical potential between the two poles. Comparably large potential differences and small distances to the grounded housing can be found at the outer radius of the coil. The capacitance between the outer windings and the housing therefore plays an important role in the overall capacitance. For the second coil body a different winding was chosen to reduce the parasitic capacitance.

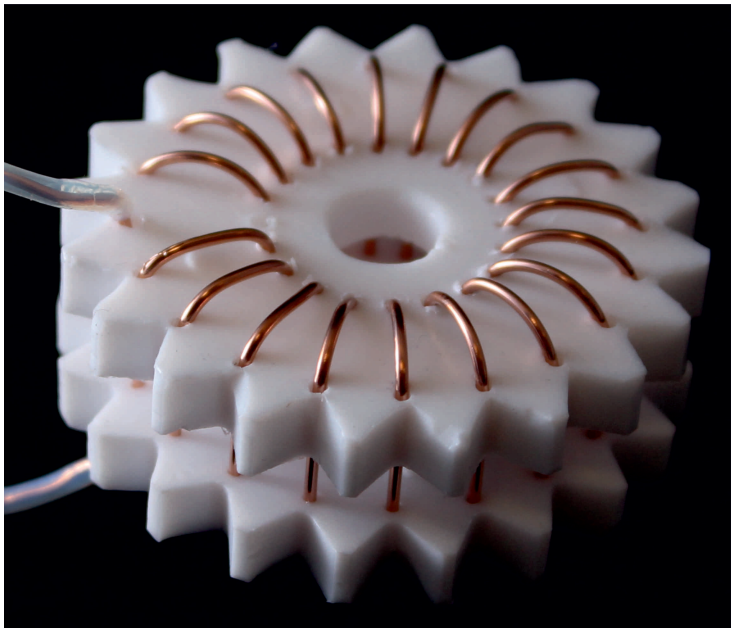

**Figure 4.21:** Cyclotron coil with the right dimensions. The wire is now bent on the top and the bottom, but straight on the sides. The coil body consists of two PTFE plates with spacers in between. The amount of PTFE between the coil wire and the housing is reduced by a triangular cut. The remaining tips center the coil at room temperature.

Fig. 4.21 shows a picture of the second coil body. It consists, similar to the axial coil, of two PTFE plates separated by a spacer. This reduces the amount of PTFE and therefore the losses. The position of the wire is fixed by guiding the wire through holes which define the geometry of the coil body.

The wire is now straight on the sides and bent on the top and bottom. For the first version of this coil body the same outer and inner radius was chosen as for the first toroidal cyclotron coil. Fig. 4.22 shows the difference in curvature of the wire for the two types of coil body.

In order to achieve a final resonance frequency of 30 MHz a free resonance frequency of $\approx$ 60 MHz is needed. For the new coil body 15 windings were chosen for the first measurements. The resonance frequency of such a coil with the same dimensions as the first type (including a height of 20 mm) was measured to be $\sim$ 70 MHz. The capacitance is about ten times higher than expected, while the inductance is a tenth of the desired value. In order to find an explanation for these values the measurement was repeated with different heights of the coil body. Tab. 4.4 gives the capacitance and inductance of these resonators. The explanation for the change in capacitance and inductance is the following:

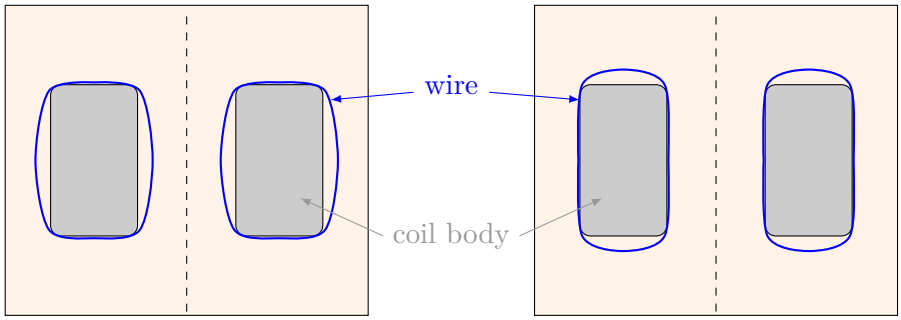


**Figure 4.22:** Sketch of the different curvatures of the wire (blue) for both types of cyclotron coil bodies. The dashed line represents the symmetry axis, the light orange rectangle the size of the resonator housing. The cross-sectional area of the coil body is grey.

**Table 4.4:** The measured capacitances and inductances of the cyclotron resonator for a coil body with different heights.

| height | $\nu_0$ | inductance | capacitance |
|---|---|---|---|
| 20 mm | 70.3 MHz | 0.139 µH | 36.24 pF |
| 15 mm | 68.23 MHz | 1.03 µH | 5.265 pF |
| 5 mm | 134 MHz | 0.442 µH | 3.19 pF |

- 20 mm: Due to the top/bottom curvature the wire is in this case closer to the housing than in the first coil type. This leads to a higher parasitic capacitance. The low inductance can be explained by the formation of a mutual inductance between the coil and the housing. Another additional effect is that the windings do not all have the same height on the bottom and the top.

- 15 mm: Due to the larger distance to the bottom and lid the mutual inductance is smaller leading to a higher inductance. The wire is shorter, therefore the capacitance between the windings of the coil is reduced. The larger distance to the housing additionally decreases the capacitance.

- 5 mm: The capacitance is further reduced by the use of a shorter wire. The smaller inductance can be explained by the reduction of the cross-sectional area. If one assumes that the curvature of the wire on the top and the bottom of the coil leads to an overall increase of 2 mm in height the height ratio, equal to the ratio of cross-sectional areas, $(15 + 2)\,\text{mm}/(5 + 2)\,\text{mm} = 2.43$ is very close to the ratio of the inductances $L_{15}/L_5 = 2.33$.

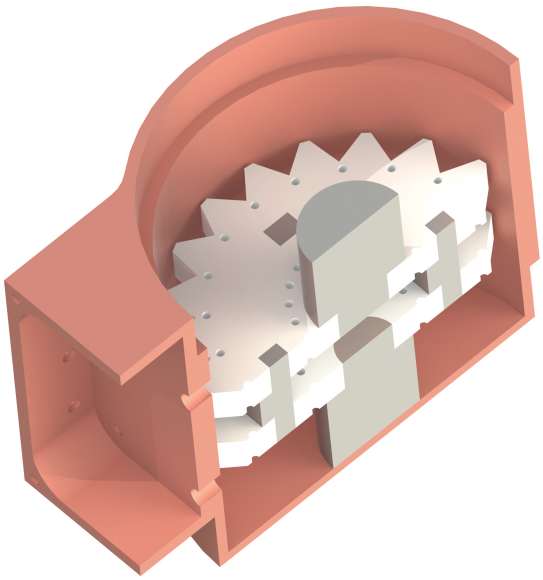

| | value |
|---|---|
| height | 15 mm |
| inner radius | 8.7 mm |
| outer radius | 18.5 mm |
| wire hole radius | 0.55 mm |
| outer PTFE radius | 23.9 mm |

**Figure 4.23:** Sectional view of the 3D model of the cyclotron resonator and values for the geometry. The holders and the spacers are shown in a darker colour to distinguish them from the PTFE plates. A picture of the cyclotron resonator can be seen in Fig. B.3.

The change in inductance and capacitance between the coils with a height of 15 mm and 5 mm can be explained only by the geometry of the coil. Therefore, the effect of the housing seems to have vanished for a height of 15 mm. The effect of a mutual inductance due to the sides of the coil being close to the housing can be neglected. The effect was not noteacible in the first type of resonator, where the winding was closer to the housing.

The height of the final geometry was hence chosen to be 15 mm. In order to further increase the inductance the number of windings was increased. At the same time the capacitance between the wires in the center of the torus was kept constant by increasing the inner radius.

A 3D model of the final design inside the housing is shown in Fig. 4.23. The values given in this picture are those of the final geometry. The holders, the plates and the spacers in between are all made out of PTFE. The wire position is fixed by holes in the PTFE plates. PTFE is a dielectric material and increases the capacitance between the coil and the housing. This effect was minimised by cutting triangles out of the plates where the holes are. In the middle this was not possible, as the holders press on this part of the plates.

The inner radius of the housing is 24 mm and thus 0.1 mm larger than the tips of the coil body. The tips therefore center the coil at room temperature. Since it will still be pressed at 4 K the shrinkage of the tips does not matter.

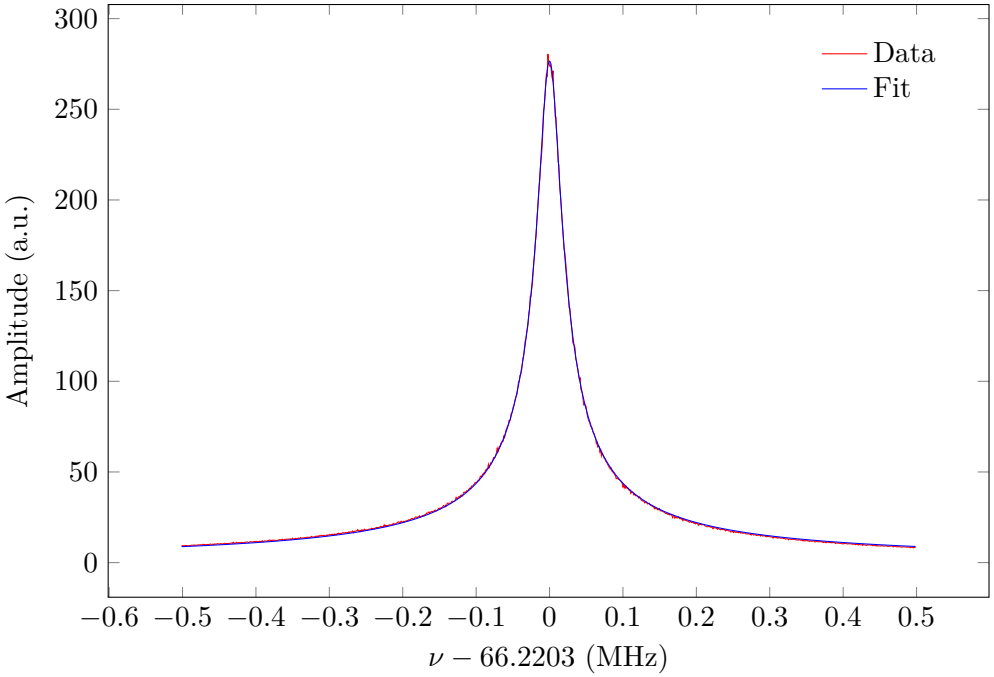


**Figure 4.24:** Resonance curve of the free cyclotron resonator with the dimensions given in Fig. 4.23. The fit to the shown data resulted in $\nu_{\text{fit}} = 66.2\,\text{MHz}$ and $Q_{\text{fit}} = 2066(5)$, where the error of the resonance frequency resulting from the fit was below 1 mHz.

### 4.7.2 Performance

The final geometry gave a free resonance frequency of 66.2(5) MHz. The errors again represent the reproducibility of the setup, see Sec. 4.6.2. The error of the resonance frequencies was estimated to be 0.5 MHz, resulting from a variation of $\nu_0$ depending on the coupling and the length of the wire sticking out of the resonator housing. Fig. 4.24 shows a resonance curve of the unloaded cyclotron resonator. Tab. 4.5 shows the resonance frequencies for different settings and measurement setups.

**Inductance and Capacitance** The determinations of the inductance and the capacitance of the resonator were done at room temperature. Instead of the trap a 15 (2) pF capacitor was soldered between the hot end and ground. After measuring the resonance frequency in this setup,

$$\nu_{0,\text{trap}} = 32.0(5)\,\text{MHz} \quad , \tag{4.36}$$

the capacitor was removed and the free resonance frequency (65.0 (5) MHz) was recorded.

**Table 4.5:** Resonance frequencies and maximal $Q$-values for different setups. The errors in the $Q$-values for the measurements at room temperature arise from different couplings between the resonators and the network analyser. The errors of all other measurands are discussed in the text.

| Setting | Resonance frequency | $Q$-value |
|---|---|---|
| free resonator @ 300 K | 65.0 (5) MHz | 370 (10) |
| resonator with 15 pF "trap"@ 300 K | 32.0 (5) MHz | 220 (10) |
| free resonator @ 3 K | 66.2 (5) MHz | 2066 (5) |
| resonator with amplifier @ 3 K | 56.17 (1) MHz | 850 (5) |

The inductance and capacitance of the resonator are then given by:

$$\begin{aligned} C &= 4.8(3)\,\mathrm{pF} \quad , \\ L &= 1.25(6)\,\mu\mathrm{H} \quad . \end{aligned} \tag{4.37}$$

The inductance is only half of that of the first cyclotron resonator type. This can be explained by the smaller cross-sectional area and the magnetic field confinement inside the coil. Since the wire is not uniformly wound on the top and on the bottom the loss of the magnetic flux might still lead to a mutual inductance and a decrease in the overall inductance.

**Cool Down Process** During the cool down of the resonator in the cryocooler the resistance of the copper is decreasing with decreasing temperature. Fig. 4.25 shows the measurement of the $Q$-value for different times during the cool down process. The blue curve shows the temperature of the cryocooler as determined by the built-in temperature sensor.

The time for the cool down of the cryocooler (160 min). The thermalisation of the resonator takes about 7 h. The measurement after one day of thermalisation is shown in Fig. 4.24 and resulted in a $Q$-value of 2066(5).

**Resonator connected to the Amplifier** Fig. 4.26 shows a noise spectrum of the resonator and amplifier at room temperature. Connecting the amplifier to the resonator reduces the resonance frequency due to the additional input capacitance of the amplifier and the capacitance of the varactor diode. For this measurement the hot end of the coil was directly soldered to the input of the amplifier, eliminating the problem of the non-reproducible coupling.

The resonance frequency of the resonator connected to the amplifier is

$$\nu_{0,\mathrm{amp}} = 56.17(1)\,\mathrm{MHz} \quad . \tag{4.38}$$

The error of the fit was below 1 mHz. Therefore, a conservative error is estimated to be 0.01 MHz. This measurement was done with a supply voltage of 0 V for the varactor

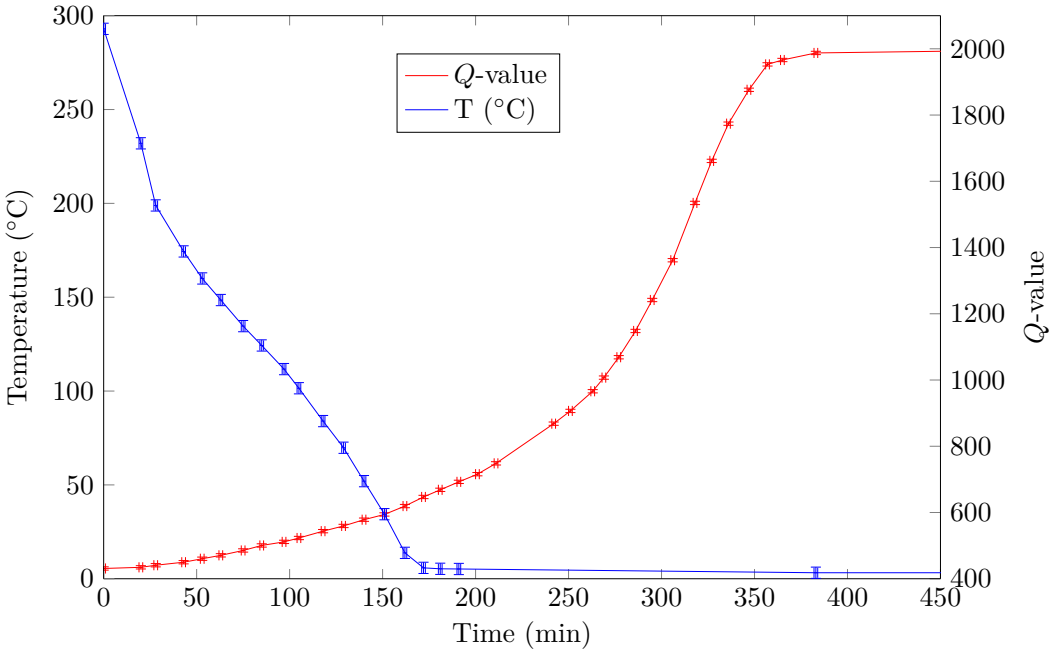


**Figure 4.25:** $Q$-value of a cyclotron resonator at different temperatures during the cool down process. For the time an error of 1 min was taken as this is the measurement time. The error of the temperature was estimated from the fluctuation of the temperature sensor. The error of the $Q$-value resulting from the fit was $\pm 5$. This does not imply that the parameters of the resonator are reproducible to this level of precision.

diode. Decreasing the voltage to $-20\,\mathrm{V}$, thereby decreasing the capacitance from 8 pF to 1 pF, results in a resonance frequency of

$$\nu_{0,\mathrm{varac}=8\,\mathrm{pF}} = 59.62\,(1)\,\mathrm{MHz} \quad , \tag{4.39}$$

where the same error estimation as above is used.

The coupled performance of the resonator and the amplifier is shown in Fig. 4.27. For this measurement the varactor was biased with 0 V. The bias voltages of the first and second gate define the back action on the resonator and therefore also the $Q$-value.

In Fig. 4.28 the voltage gain of the amplifier without the varactor diode is shown. The maximal gain decreases with decreasing gate 2 voltage. Its maximum can be found for $U_{g1} = -0.75\,\mathrm{V}$ and $U_{g2} = 0\,\mathrm{V}$, where the $Q$-value has its minimum. Curves for a gate 2 voltage $U_{g2} < -0.6\,\mathrm{V}$ are not shown, as they resulted in negative gain only. Connecting the varactor to the amplifier reduces the gain to a maximal value of $\approx 2.5\,\mathrm{dB}$.

One possible setting for a high gain and a high $Q$-value would be $U_{g1} = -0.65\,\mathrm{V}$ and $U_{g2} = 0\,\mathrm{V}$. There the gain is $\sim 5\,\mathrm{dB}$ and the $Q$-value $\sim 750$. This corresponds to a parallel resistance of

$$R_P = Q\omega L \approx 329.8\,\mathrm{k\Omega} \quad . \tag{4.40}$$

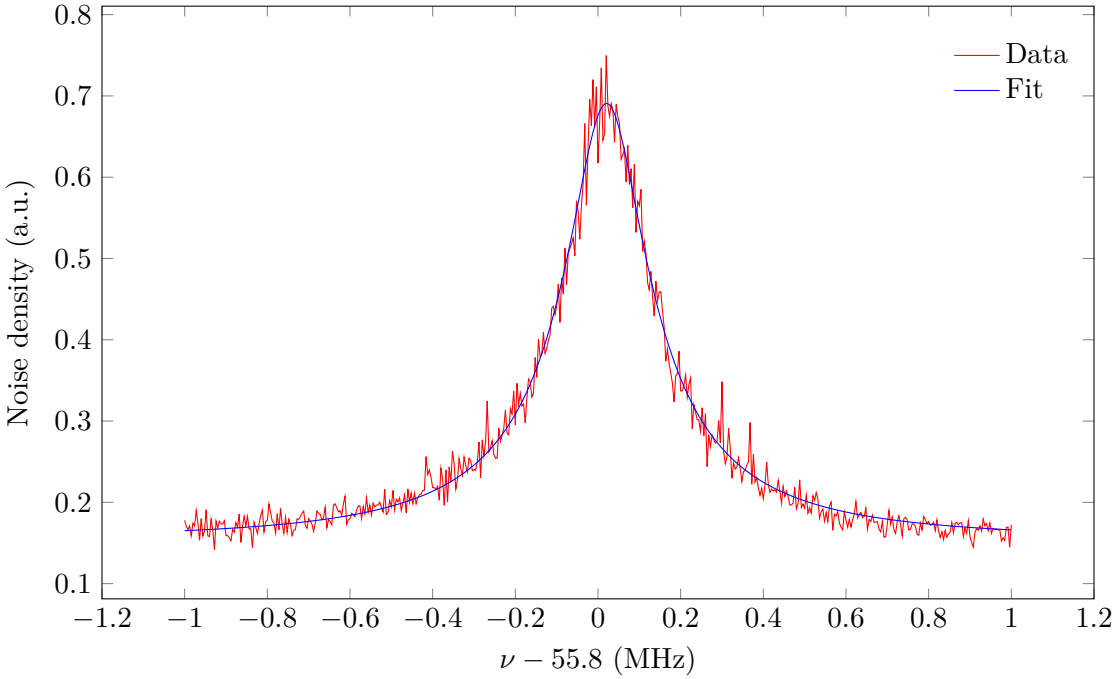


**Figure 4.26:** Noise spectrum of the cyclotron resonator connected to the amplifier at room temperature. In order to fit the data with the fit function in Eq. (4.23) a temperature of $T = 300\,\mathrm{K}$ was assumed. The resulting $Q$-value was 291(5).

For a $^{35}Cl^{10+}$-ion the cooling time constant with the cyclotron detector connected to one half of a correction electrode ($D_{\mathrm{eff}} = 23.1\,\mathrm{mm}$) at resonance is:

$$\tau = \frac{m D_{\mathrm{eff}}^2}{q^2 R_P} \approx 36.6\,s \quad . \tag{4.41}$$

Thus, the time for direct cooling of the modified cyclotron motion will be $\lesssim 10\%$ of a cyclotron frequency determination cycle for a $^{35}Cl^{10+}$-ion. For heavy highly-charged ions the cooling time constants will be reduced.

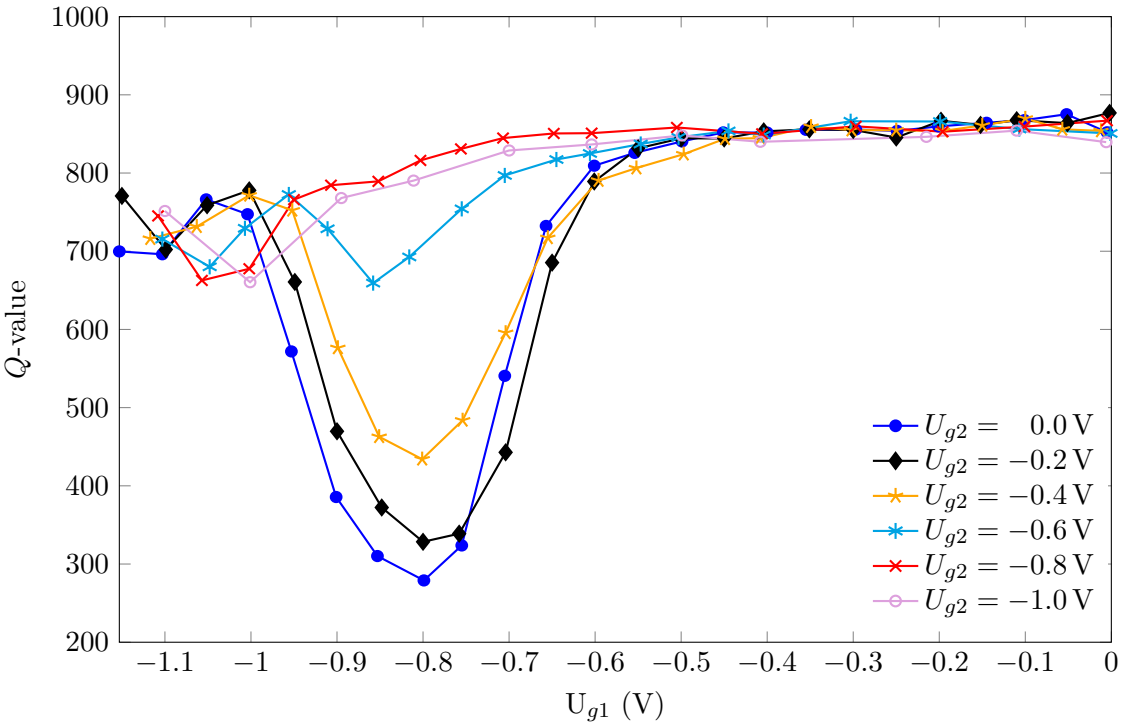


**Figure 4.27:** $Q$-value of the resonator connected to the amplifier for different gate voltages. For all measurements the supply voltage for the varactor diode was kept constant as well as the drain voltage of the amplifier. The drop in the $Q$-value can be explained by the back action of the amplifier onto the resonator.

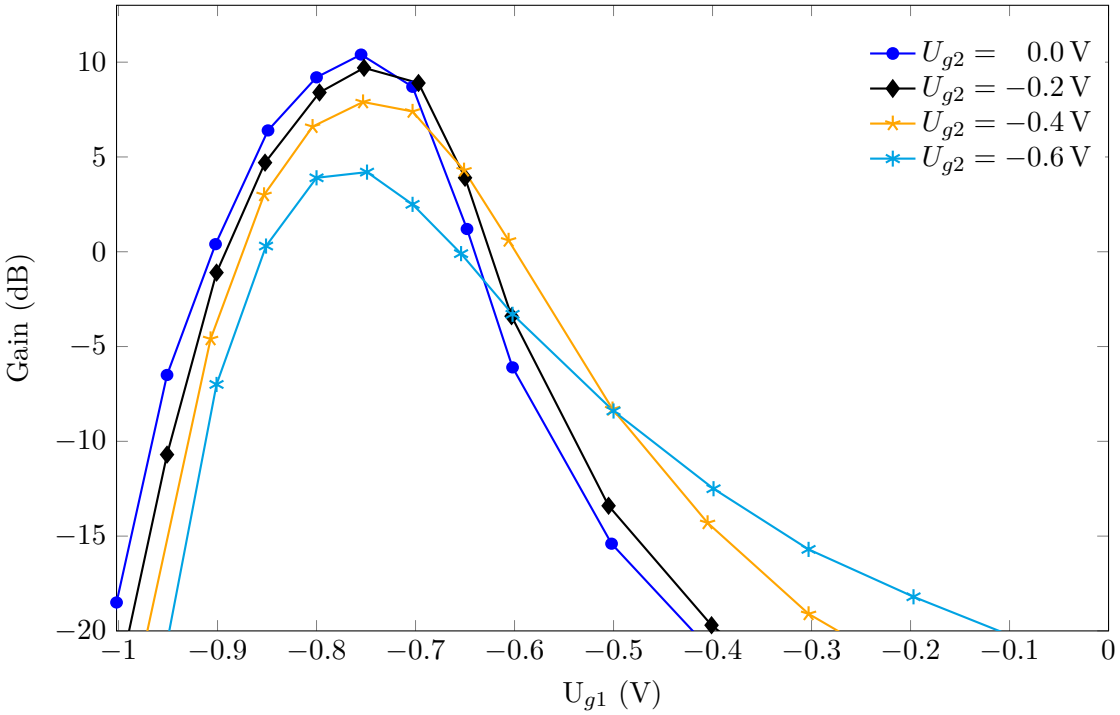


**Figure 4.28:** Gain of the cyclotron amplifier (without varactor) for different gate voltages. Only curves with a maximum gain larger than zero are shown.

# Chapter 5

# Summary and Outlook

In the framework of this thesis a new detection system for the next version of PENTATRAP was designed and tested. A toroidal cyclotron resonator design was devoloped and the geometry of the axial resonator was adapted to the new experimental setup.

The ten resonators needed at PENTATRAP are arranged in two towers with five resonators each. The housing is the same for axial and cyclotron resonators, allowing one to freely choose the position for each of the resonators. Hence, the superconducting axial resonators can be put in the lower magnetic field region, while the cyclotron resonators are positioned closer to the traps in order to minimise the influence of the cabling on the resonance frequency. Instead of screwing a lid to every resonator housing the bottom of the upper resonator acts as a lid to the lower one. The whole tower is pressed together to ensure a proper electrical connection between the lid and the housing.

For the final design for the axial resonator a free resonance frequency of 1050(3) kHz and a resonance frequency of 662.630(1) kHz for the resonator connected to the trap was measured. The maximum $Q$-value for the resonator without trap or amplifier attached is 33600(500). Connecting the cryogenic amplifier to the resonator lowered the $Q$-value to $\sim$ 4800 and resulted in a signal-to-noise ratio of $\sim$ 20 dB for the appropriate bias voltages. For the dip detection of a $^{35}Cl^{10+}$-ion this would result in a signal width of 1.73 Hz, which is close to the 1 Hz dip width that is aimed for at the start. By changing the coupling constant $\kappa$ between the amplifier and the resonator the dip width can be adjusted for subsequent measurements.

In order to find the dimensions for the new toroidal cyclotron resonators with the required resonance frequency ($\sim$ 30 MHz) and a high $Q$-value the first approach was to use simulations with *COMSOL Multiphysics*, see A. At the same time the resonance frequency of a first prototype was measured. A high discrepancy between simulation and experimental results the simulations were stopped and the final resonator design was developed based on experimentally input. Possible explanations for this disagreement include the simplifications of the resonator model, which were neccessary due to limited computing power, see Sec. A.2.3.

Two different coil types were tested, where the main difference is the curvature of the coil wire. This leads to a difference in resonance frequency and $Q$-value, even if

the two coil bodies have the same dimensions. The maximum $Q$-value of 3100 for the first coil type is higher than that of the second coil type ($Q \approx 2000$). Still, since the second coil body type is easily made on the milling machine, a final geometry leading to the right resonance frequency of 32 MHz was developed with the second version. With this geometry a cooling time constant for a $^{35}Cl^{10+}$-ion with the resonator connected to one half of the correction electrode of 36.6 s is reached, which takes about 10% of the overall time for a cyclotron frequency measurement. Still, by finding a geometry of a first coil body type which results in the same resonance frequency, the $Q$-value will most probably be larger and the cooling time constant reduced. Since the first coil type is not easily made, it is not modular and cannot be made on the milling machine, the right dimensions cannot be found by using different prototypes. Therefore, the simulations need to be understood in order to improve the cyclotron detector.

This detection system developed in this thesis is sufficient for the first run of PENTATRAP version 2. Still, several improvements will be made before manufacturing of all housings and coils. The bottom plates of the housings have a thickness of 1.5 mm. Due to the strong compression at room temperature the resulting force can lead to a dent in the copper of the bottom. This leads to imperfections in the housing and possibly also in the electric connection between the housings.

The electrical connection between the lid and the housing needs to be improved. While pressing pieces of copper between the two led to a major improvement in the $Q$-value and electrical connection, this might still not be ideal.

Both of these problems can be solved by increasing the thickness of the bottom to several millimeters. In this way screws can be used to fix the lid to the housing after pressing the tower together. This will improve the electrical connections. In order to leave the inner volume of the resonator unchanged, the height needs to be increased. This can be done as the total height of this detection system does not extend over the total length of the resonator chamber.

For the axial resonators only minor changes are planned for the future. In order to be able to eliminate any contributions of the housing to the overall inductance, a test resonator with a smaller outer radius of the coil might be constructed. If there is an effect of the housing on the inductance, similar to the cyclotron resonator, the outer axial coil radius needs to be reduced. The right number of windings will then have to be deduced from a test coil.

As this thesis was ending, a fundamental decision for the new detection system was made by the members of the PENTATRAP experiment. In order to minimise the inductive and capacitative effect as well as dielectric losses of the cabling on the cyclotron resonators they need to be as close as possible to the traps. Therefore, instead of only positioning the cyclotron resonators on the highest positions in the resonator chamber, they will be mounted directly above and below the trap tower. Depending on the space, two or three resonators will be positioned above the traps and around the beam line. Regardless of the number of cyclotron resonators, the limited space there requires smaller housings with only about half the radius compared to the detection system developed here. This makes it impossible to wind toroidal coils and the coil type will be changed

back to helical coils. The remaining five axial resonators will be set up in the resonator chamber in two towers with three resonator housings each. The remaining housing might be used to hold additional electronics.

After an extensive modification was made for PENTATRAP version 1.6 the experiment will again be assembled in the very near future. Commissioning experiments are expected to start at the end of this summer, while PENTATRAP version 2 will be set up at the end of 2015.

# Appendix A

# Simulations of the Cylotron Resonator

In the case of the axial resonators the previous design was helpful in developing the new coils. The capacitance could be approximated by that of the previous version and the inductance estimated from the geometry. This was not possible for the cyclotron resonators. In parallel to the experimental tests of the first coil design (see Fig. 4.20) simulations were performed to find optimal coil dimensions for a resonator with a high $Q$-value and high inductance. Unfortunately, very early in this process it became clear that the deviation of the experimental from the simulation results were too large to develop a resonator this way. This chapter serves to show the first results of the simulation studies and explain the difference to the experiment.

For the simulations the FEM-based (finite element method) simulation software *COMSOL Multiphysics* [Coma; Comb] was used. The 3D model of the resonator is built using *SolidWorks 2014* and imported into *COMSOL*.

## A.1 Finite Element Method

The finite element method (FEM) is a standard tool to solve partial differential equations. The following descriptions is based on [RIB12; GN08].

The solution domain, in this case the model of the resonator, is divided into finite elements. For each of these elements the underlying differential equation is solved for the appropriate boundary conditions. This results in a system of equations which can be solved numerically and whose size is determined by the number of finite elements.

The partial differential equation that needs to be solved can be written as:

$$L[f] = s \quad , \tag{A.1}$$

where $f$ is the unknown function, $s$ is the source and $L$ is an operator which acts on the domain $\Omega$. The process of FEM can then be devided into four steps:

1. The solution domain $\Omega$ is divided into non-overlapping elements, creating the so-called mesh.

2. The solution is expanded in a finite number of basis functions:

$$f(\vec{\mathbf{r}}) = \sum_{i=1}^{n} f_i \varphi_i(\vec{\mathbf{r}}) \quad . \tag{A.2}$$

   The coefficients $f_i$ multiply the basis functions $\varphi_i(\vec{\mathbf{r}})$, which are non-zero only in a few elements.

3. The coefficients $f_i$ should be chosen such, that the residual

$$r = L[f] - s \tag{A.3}$$

   is as small as possible.

4. Weighting functions are chosen: $w_i,\ i = 1, 2, ..., n$. In the Galerkin method, which is used in Comsol [Coma], the weighting functions are the same as the basis functions: $w_i = \varphi_i$. Lastly, the weighted residuals are set to zero,

$$\langle w_i, r \rangle = \int_\Omega w_i r \mathrm{d}\Omega = 0 \quad , \tag{A.4}$$

   and solved for the unknown functions $f_i$.

In addition to the limited numerical precision of a computer the error of the solution depends on how well the true geometry is decribed by the mesh [Coma]. An advantage of the FEM is that certain parts of the model can be meshed with smaller elements, thereby increasing the resolution locally. If the element size approaches zero, the geometry in most cases can be seen as perfectly described by the mesh. In this case the solution of the FEM approaches the true solution of the partial differential equation [And15]. For the following simulations the RF module of Comsol was used [Comb].

## A.2 Resonance frequency of the Cyclotron Resonator

The simulations were done for the first coil body, which is described in detail in Sec. 4.7.1. With 20 windings the measured free resonance frequency was:

$$\nu_0 \approx 49\,\mathrm{MHz} \quad , \tag{A.5}$$

with a $Q$-value of $\approx 500$ at room temperature.

For the simulations the model of the resonator was simplified by removing the slit between the lid and the housing and thereby assuming a perfect electrical connection between the two parts. Further, the amplifier box was removed as it does not contribute to the electromagnetic properties of the resonator.

A difference between the simulation and the experiment is the grounding of the cold end. The hole in the housing was removed and the wire ends by touching the wall of the housing. This is legitimate since the potential difference between the cold end before leaving the housing to the housing is nearly zero. It therefore makes no difference, if the cold end is grounded on the inside or on the outside.

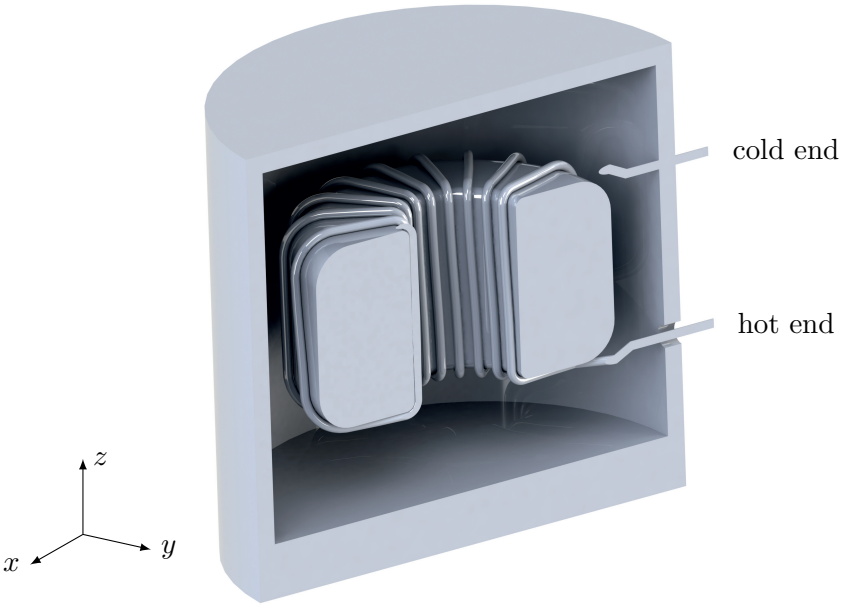


**Figure A.1:** Cross-sectional view of the CAD model used in the simulations. In contrast to the real coil body this one is solid and has no spacers. The cold end is grounded by directly ending on the resonator housing. The thickness of the bottom and the top of the housing is irrelevant for the simulations.

### A.2.1 Simulations without Material Properties

At the resonance frequencies of the cyclotron resonator the current in the copper is nearly completely on the surface (see Sec. 4.1.2). Hence, for a first simulation the surfaces of the wire and the housing are taken to be perfect electric conductors. Since there are no losses in this case it is not possible to determine a $Q$-value.

For the first simulation the wire lies flat on the coil body with a distance of 0.05 mm in between. The size of the mesh between the wire and the coil body therefore had to be so fine that it was impossible to simulate this geometry with the given computing power. In order to circumvent this problem the coil body was removed from the simulation domain.

Fig. A.1 shows the model used for the first simulations. The resonance frequency obtained from the simulations was:

$$\nu_{0,\mathrm{flat}} \approx 68\,\mathrm{MHz} \quad . \tag{A.6}$$

The difference between the simulation and the experiment is therefore $\approx 20\,\mathrm{MHz}$.

In order to find an explanation for this difference a second simulation was performed with a more realistic wire run. The distance of the wire to the coil body was taken as 2 mm on the outside and 1 mm in the middle (compare to Fig. 4.20).

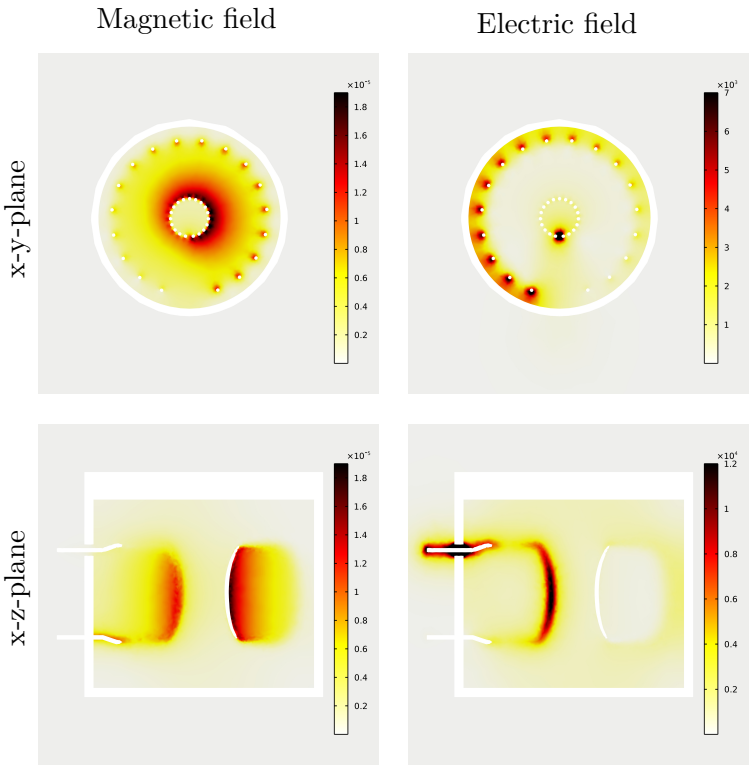


**Figure A.2:** Distribution of the magnetic and electric field amplitude at the resonance frequency shown for two cross sections of the resonator. The magnetic field is completely confined inside the coil and strongest, where the electric field is weakest. The electric field is strong at the hot end and decreases towards the cold end, where the potential between the coil and the housing is nearly the same.

The resonance frequency was thereby reduced to

$$\nu_{0,\text{bent}} \approx 58\,\text{MHz} \quad , \tag{A.7}$$

which is still $\approx 10\,\text{MHz}$ higher than the experimental result.

Fig. A.2 shows the computed electric and magnetic field of this simulation for two planes. Analogue to an $LC$-circuit the magnetic field is large where the electric field is small and vice versa.

The magnetic field is nearly completely confined inside the coil. It is larger on the inside because the windings are closer together. The electric field is largest between the outer windings and the housing. The inner windings do not seem to generate an electric field, which can be explained by the fact, that they are close in electric potential. This also means that the capacitance between the windings in the middle can be neglected compared to the overall capacitance.

### A.2.2 Simulations with Material Properties

The simulation of the resonator with bent wires was repeated with the right material properties. The housing and the wire were set as copper with an electrical conductivity of $5.998 \cdot 10^7$ S/m, a relative permeability of $\mu_r = 1$ and a relative permittivity of $\epsilon_r = 1$. The temperature was set to room temperature and the pressure to normal air pressure.

The simulations yield the resonance frequency and the damping of the electromagnetic field from which the $Q$-factor can be determined [Comb]. The resulting resonance frequency is

$$\nu_{0,\text{copper}} \approx 58\,\text{MHz} \quad , \tag{A.8}$$

and the $Q$-value is given by

$$Q = 540 \quad . \tag{A.9}$$

While the $Q$-value agrees with the experimental value at room temperature, the resonance frequency is still $\approx 10\,\text{MHz}$ higher than the experimental value. Still, the wire curvature in this model seems to describe the real resonator best.

### A.2.3 Possible Explanations of the Difference between Experiment and Simulation

The simulations were originally planned to be used to find a geometry which yields the right resonance frequency and the highest $Q$-value. After the first simulations showed such a difference this idea was discarded. For the simulations described above no convergence tests were made. It is therefore possible that the results given are not the real solution and a convergence test (decreasing the mesh until the solution does not depend on the mesh size) leads to a lower final frequency, which approaches or even coincides with the experimental value.

Other explanations are based on the less than perfect windings in the experimental coil and the simplifications made for the simulation model. In order to end up with a lower resonance frequency in the experimental results the capacitance and/or the inductance need to be larger.

The winding of the coil in the simulation is regular, whereas the distance between the windings as well as their curvature is irregular for the experimental coil. On the outside some wires might be even closer to the housing, thereby increasing the capacitance.

The dielectric materials are not taken into account in the simulations. The coil body and the holders are made out of PTFE, which has a relative permittivity of $\epsilon_r = 2$. This leads to an increase of capacitances between the windings of the coil.

Overall, the difference between the experimental value and the simulation is not completely understood. More simulations to quantify these effects need to be done.

# Appendix B

# Lab Pictures

**Figure B.1:** Picture of the axial coil inside the housing. The two halves of the coil body are pressed together by wrapping several layers of PTFE tape around the outer spacers. The inner surface of the housing is mechanically polished.

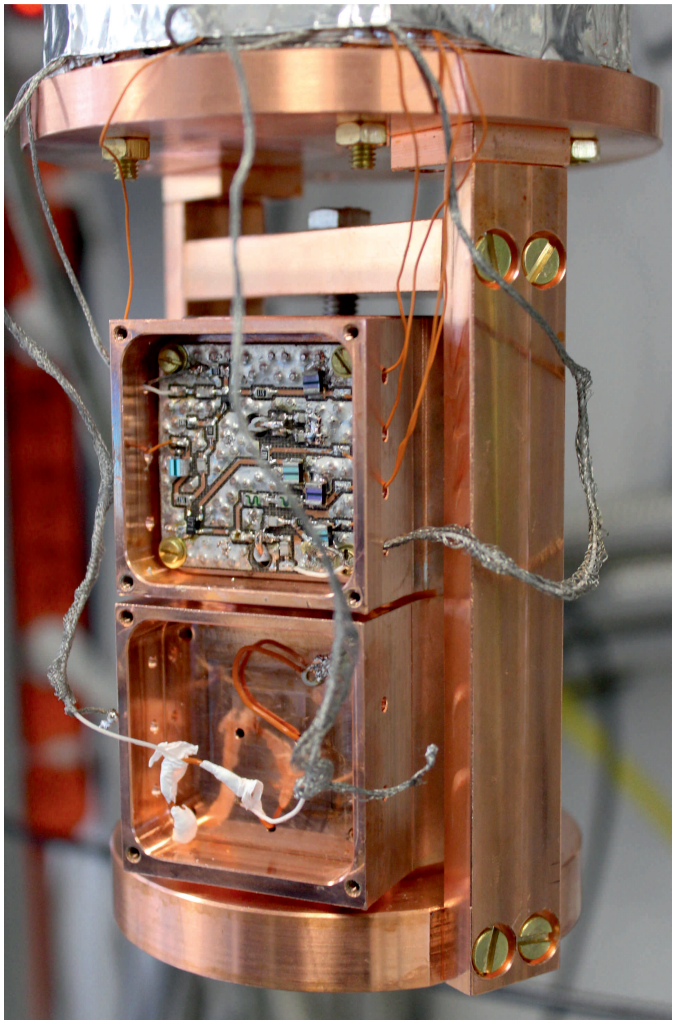

**Figure B.2:** Picture of the test setup fixed to the cryocooler. The grey cables are cryogenic coaxial cables used for the excitation and measurement of the resonator. The orange cables are used for the supply voltages for the amplifier. In the upper housing the cyclotron resonator is connected to the amplifier. At the lower housing the cryogenic coaxial cables are capacitively coupled to the copper cable, which is soldered to the end of the NbTi wire used in the axial resonators.

**Figure B.3:** Picture of the cyclotron coil inside the housing. The inner surface of the housing is mechanically polished.

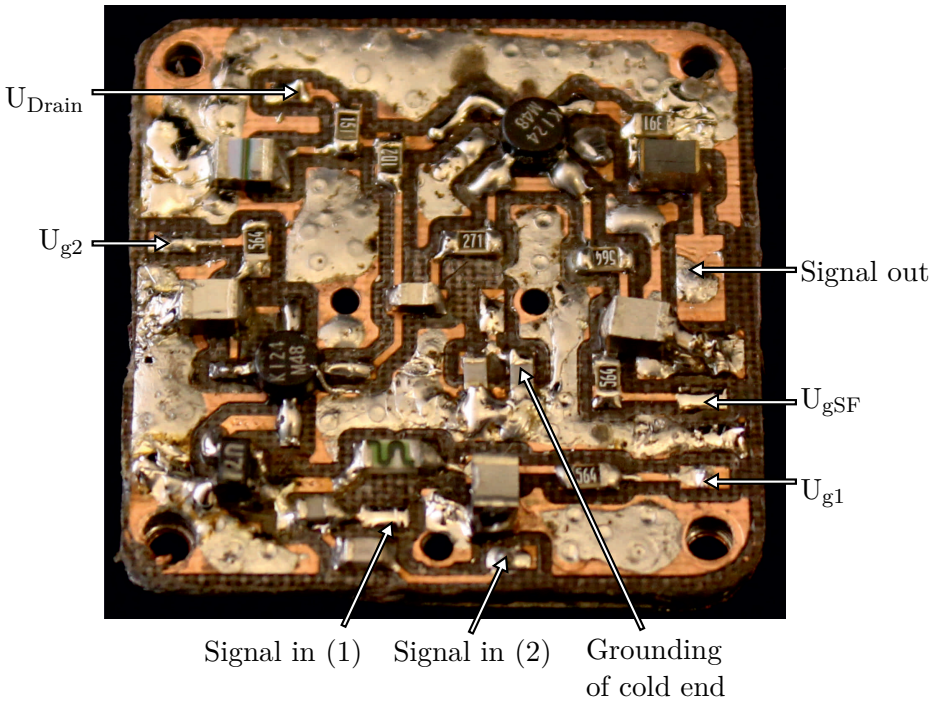


**Figure B.4:** Picture of the axial amplifier. Signal in (1) is used to connect the amplifier to the resonator, while the capacitor in front of the Signal in (2) is used to cpacitively couple the excitation signal to the resonator.

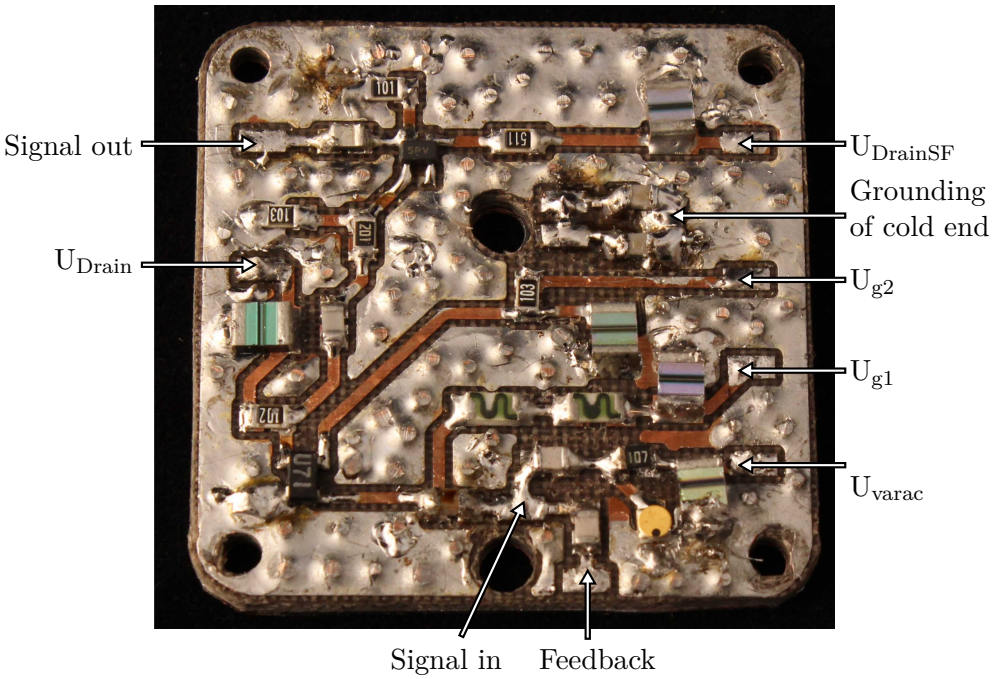


**Figure B.5:** Picture of the cyclotron amplifier. Additionally on the board is the grounding of the cold end of the coil and a pad to apply a feedback (see [Stu11]).

# Appendix C

# Technical Drawings of the Test Setup

This section shows technical drawings of the test setup for the new detection system. In Fig. C.1 several views of the complete test setup are shown. In the cross-sectional view prototype coil bodies can be seen.

The pressing of the two resonators works by tightening the screw (denoted as 11 in Fig. C.1). Since the position of the bar 6 is fixed to the outer bar 5, the plate 1 will be pressed downwards.

The drawing of the housings can be seen in Fig. C.2. The dimensions of the housings are identical for both resonators. The only difference between them is the number of holes into the amplifier box from the outside and from the housing.

The technical drawings of the test setup and the resonator housings were done by the construction workshop at MPIK, according to the specifications given by the author. This was neccessary as they tend to the whole technical drawings of PENTATRAP. All other models were built by the author.

Fig. C.3 and Fig. C.4 show the drawing of the CAD model of the PTFE plates as well as the spacers for the coil bodies. Since the plates are made on the milling machine only the outline of the plate is important. The striped area is introduced into the CAD modell to prevent the milling machine from cutting this part.

The hole in the spacer is a stud hole. This prevents the rod, which is used connect the two halves of the coil, from sliding through the spacer. The spacers are set back from the cutting line of the torus by 1 mm. Therefore, thicker parts of the spacers do not prevent a perfect torus.

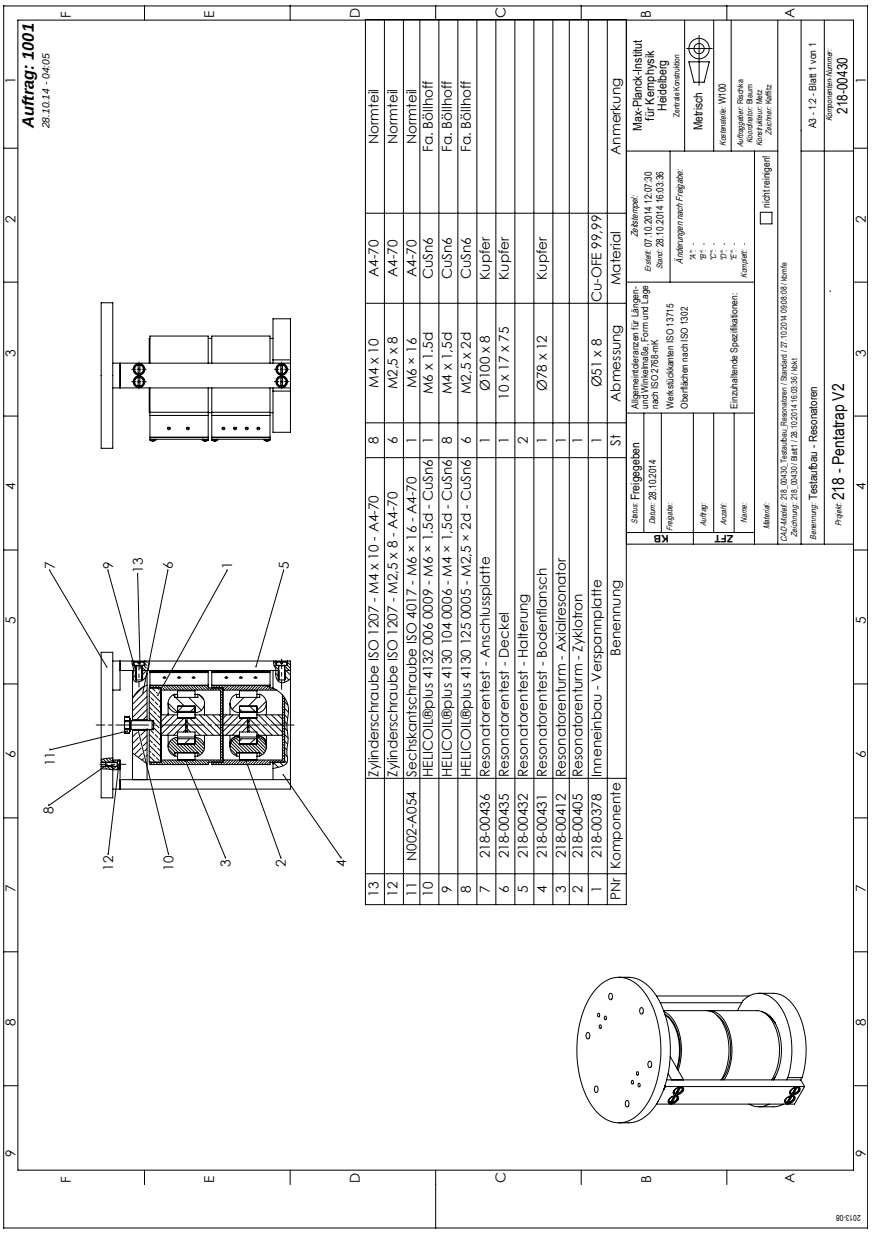


**Figure C.1:** Overview of the test setup as well as a list of all parts needed.

Cyclotron:

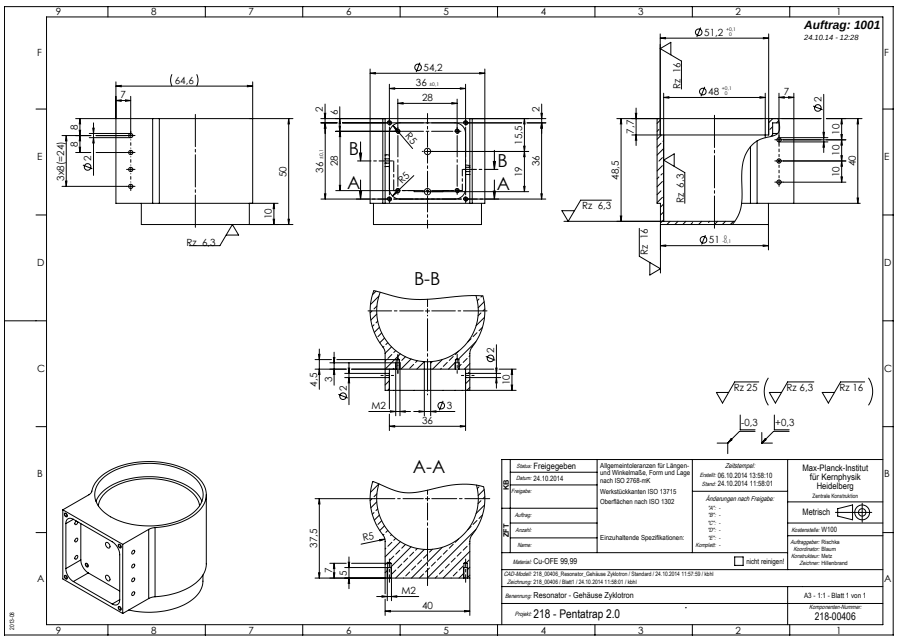


Axial:

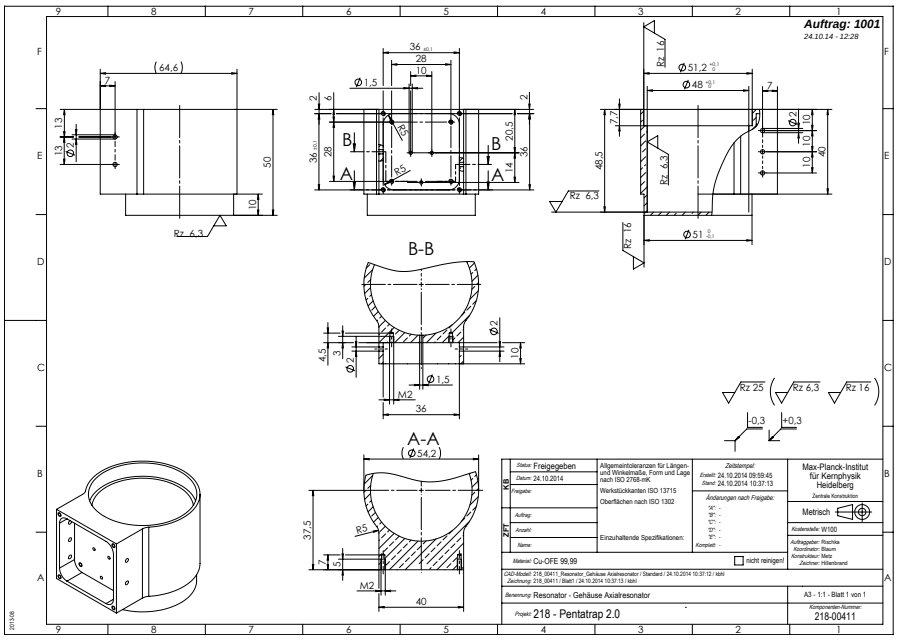


**Figure C.2:** Technical drawing of the cyclotron and axial resonator housing. The only difference between the two housings are the different number for the supply voltages for the amplifier and the holes into the amplifier. Dimensions in mm.

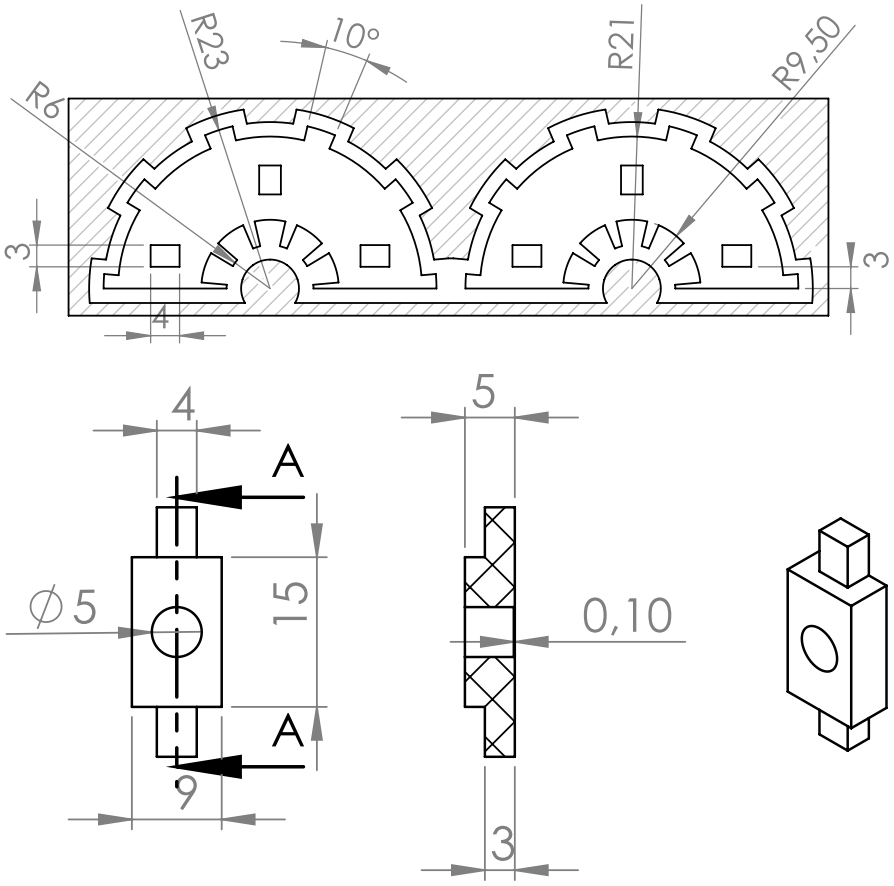


**Figure C.3:** Technical drawing of the two plates for the axial resonator as well as the spacers used to define the distance between the PTFE plates. The plates are made on the milling machine, which only cuts out the part between the coil part and the striped area. The striped area is only there to quicken the milling process. For more details, see text. Dimensions in mm.

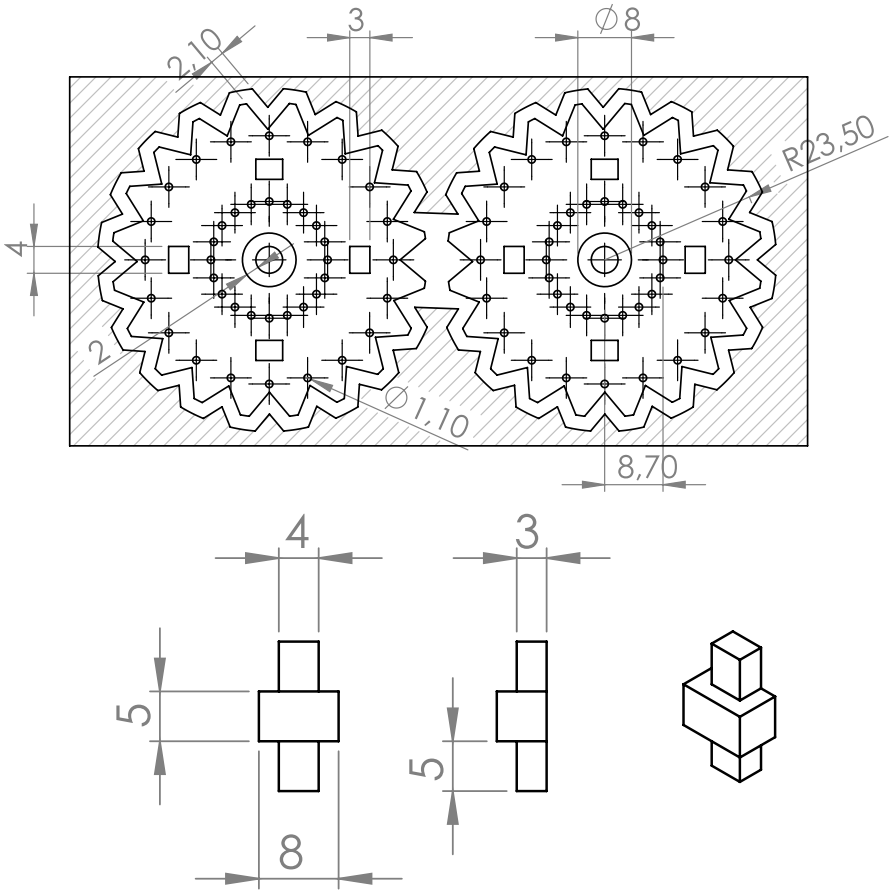


**Figure C.4:** Technical drawing of the PTFE plates and spacers for the cyclotron resonator, also made with the milling machine. Dimensions in mm.

# Bibliography


[And15] L. Andersson. Private communication. Comsol Support. 2015 (cited on page 74).

[BG82] L. S. Brown and G. Gabrielse. "Precision spectroscopy of a charged particle in an imperfect Penning trap". In: *Physical Review A* 25.4 (1982), pp. 2423–2425 (cited on page 8).

[BG86] L. S. Brown and G. Gabrielse. "Geonium theory: Physics of a single electron or ion in a Penning trap". In: *Review of Modern Physics* 58 (1986), pp. 233–311. URL: http://link.aps.org/doi/10.1103/RevModPhys.58.233 (cited on pages 7, 8, 14).

[Bla+09] K. Blaum et al. "$g$-factor experiments on simple systems in Penning traps". In: *Journal of Physics B: Atomic, Molecular and Optical Physics* 42.15 (2009), p. 154021. URL: http://stacks.iop.org/0953-4075/42/i=15/a=154021 (cited on page 37).

[BNW10] K. Blaum, Yu. N. Novikov, and G. Werth. "Penning traps as a versatile tool for precise experiments in fundamental physics". In: *Contemporary Physics* 51.2 (2010), pp. 149–175. URL: http://dx.doi.org/10.1080/00107510903387652 (cited on page 1).

[Bra00] M. P. Bradley. "A sub-ppb measurement of the mass of cesium for a new determination of the fine-structure constant". PhD thesis. Massachusetts Institute of Technology, 2000 (cited on page 11).

[CG61] R. J. Corruccini and J. J. Gniewck. *Thermal expansion of technical solids at low temperatures: a compilation from the literature*. N.B.S. Mono. Washington, DC: US. Gov. Printing Office, 1961. URL: http://cds.cern.ch/record/234002 (cited on page 44).

[CLUDMU99] J. R. Crespo López-Urrutia, A. Dorn, R. Moshammer, and J. Ullrich. "The Freiburg Electron Beam Ion Trap/Source Project FreEBIT". In: *Physica Scripta* T80B (1999), pp. 502–503 (cited on pages 2, 19, 20).

[Col] *SHI CRYOCOOLER SPECIFICATIONS, Model:SRP-062B-F-50H*. Manual. Sumitomo Heavy Industries, ltd. 2007 (cited on page 35).

[Coma] *Reference Guide Version 4.3a*. Comsol Multiphysics. 2012 (cited on pages 73, 74).

[Comb] *RF Module User's Guide*. Comsol Multiphysics. 2012 (cited on pages 73, 74, 77).

[DHMW13] G. Drexlin, V. Hannen, S. Mertens, and C. Weinheimer. "Current direct neutrino mass experiments". In: *Advances in High Energy Physics* 2013 (2013) (cited on page 2).

[DW68] H. G. Dehmelt and F. L. Walls. ""Bolometric" Technique for the rf Spectroscopy of Stored Ions". In: *Physical Review Letters* 21 (3 1968), pp. 127–131. URL: http://link.aps.org/doi/10.1103/PhysRevLett.21.127 (cited on pages 1, 2, 10, 11).

[Dör15] A. Dörr. "PENTATRAP: A novel Penning-trap system for high-precision mass measurements". PhD thesis. Ruprecht-Karls Universität Heidelberg, 2015 (cited on pages 2, 12, 17, 40).

[Ele] LPKF Laser & Electronics. *LPKF ProtoMat S103*. (cited on page 50).

[EM95] S. R. Elliott and R. E. Marrs. "A wire probe as an ion source for an electron beam ion trap". In: *Nuclear Instruments and Methods in Physics Research B* 100 (1995), pp. 529–535 (cited on page 17).

[Flü+] R. Flükiger et al. "SpringerMaterials". In: (). accessed: 06.05.2015. URL: http://materials.springer.com/lb/docs/sm_lbs_978-3-540-48230-7_53 (cited on pages 32, 35).

[Fuk+98] Y. Fukuda et al. "Evidence for Oscillation of Atmospheric Neutrinos". In: *Physical Review Letters* 81 (1998), pp. 1562–1567 (cited on page 2).

[Gas+14] L. Gastaldo et al. "The Electron Capture $^{163}$Ho Experiment ECHo". In: *Journal of Low Temperature Physics* 176 (2014), pp. 876–884. URL: http://dx.doi.org/10.1007/s10909-014-1187-4 (cited on page 2).

[GKT80] G. Gräff, H. Kalinowsky, and J. Traut. "A direct determination of the proton electron mass ratio". In: *Zeitschrift für Physik A* 297 (1980), pp. 35–39 (cited on page 9).

[GN08] R. Glowinski and P. Neittaanmäki. *Partial Differential Equations: Modelling and Numerical Simulation*. Computational Methods in Applied Sciences. Springer Netherlands, 2008. URL: https://books.google.de/books?id=xKhfyc0Nf54C (cited on page 73).

[Hay14] W. M. Haynes, ed. *Handbook of Chemistry and Physics*. 95th. CRC Press, 2014 (cited on page 31).

[Hel81] K.H. Hellwege. *Einführung in die Festkörperphysik*. Springer Berlin Heidelberg, 1981 (cited on page 31).

[HFG08] D. Hanneke, S. Fogwell, and G. Gabrielse. "New Measurement of the Electron Magnetic Moment and the Fine Structure Constant". In: *Physical Review Letters* 100 (2008), p. 120801 (cited on page 1).

[Ket+14a] J. Ketter et al. "First-order perturbative calculation of the frequency-shifts caused by static cylindrically-symmetric electric and magnetic imperfections of a Penning trap". In: *International Journal of Mass Spectrometry* 358 (2014), pp. 1–16 (cited on page 14).

[Ket+14b] J. Ketter et al. "Classical calculation of relativistic frequency-shifts in an ideal Penning trap". In: *International Journal of Mass Spectrometry* 361 (2014), pp. 34–40 (cited on page 14).

[Kön+95] M. König et al. "Quadrupole excitation of stored ion motion at the true cyclotron frequency". In: *International Journal of Mass Spectrometry and Ion Processes* 142.1-2 (1995), pp. 95–116. URL: http://www.sciencedirect.com/science/article/pii/016811769504146C (cited on page 8).

[Lee93] A. T.-J. Lee. "A low-power-dissipation broadband cryogenic preamplifier utilizing GaAs MESFETs in parallel". In: *Review of Scientific Instruments* 64.8 (1993), pp. 2373–2378. URL: http://scitation.aip.org/content/aip/journal/rsi/64/8/10.1063/1.1143938 (cited on page 38).

[LF15] H. Linse and R. Fischer. *Elektrotechnik für Maschinenbauer: Grundlagen und Anwendungen*. Vieweg+Teubner Verlag, 2015. URL: https://books.google.de/books?id=A9N8BwAAQBAJ (cited on page 48).

[LL85] H. Lindner and H. B. C. Lehmann. *Taschenbuch der Elektrotechnik und Elektronik*. Verlag Harri Deutsch, 1985 (cited on pages 29–31).

[LU+04] J. R. Crespo López-Urrutia et al. "Progress at the Heidelberg EBIT". In: *Journal of Physics: Conference Series* 2.1 (2004), p. 42. URL: http://stacks.iop.org/1742-6596/2/i=1/a=006 (cited on page 20).

[Mar+07] A. J. González Martínez et al. "The Heidelberg EBIT: Present Results and Future Perspectives". In: *Journal of Physics: Conference Series* 72.1 (2007), p. 012001. URL: http://stacks.iop.org/1742-6596/72/i=1/a=012001 (cited on page 20).

[MC] M/A-COM. *Surface Mount GaAs Tuning Varactors*. (cited on page 39).

[Mil19] J. M. Miller. *Dependence of the input impedance of a three-electrode vacuum tube upon the load in the plate circuit*. Vol. 351. Govt. Print. Off., 1919 (cited on page 38).

[Min] *Low Noise Amplifier ZFL-500Ln+*. Data Sheet. Mini-Circuits. 2014 (cited on page 36).

[MLR02] E. D. Marquardt, J.P. Le, and R. Radebaugh. "Cryogenic material properties database". In: *Cryocoolers 11*. Springer, 2002, pp. 681–687 (cited on page 44).

[Moo13] A. Mooser. "Der $g$-Faktor des Protons". PhD thesis. Johannes Gutenberg-Universität Mainz, 2013 (cited on page 32).

[MS59] W. W. Macalpine and R. O. Schildknecht. "Coaxial Resonators with Helical Inner Conductor". In: *Proceedings of the IRE* 47.12 (1959), pp. 2099–2105 (cited on page 29).

[Mye13] E. G. Myers. "The most precise atomic mass measurements in Penning traps". In: *International Journal of Mass Spectrometry* 349 - 350 (2013), pp. 107–122 (cited on pages 1, 24).

[Pie54] J. R. Pierce. *Theory and Design of Electron Beams*. 2nd. D. Nostrand Company, Inc., 1954 (cited on page 1).

[Rai+05] S. Rainville et al. "A direct test of $E = mc^2$". In: *Nature* 438 (2005), pp. 1096–1097 (cited on page 1).

[Ram39] S. Ramo. "Currents Induced by Electron Motion". In: *Proceedings of the IRE* 27.9 (1939), pp. 584–585 (cited on page 9).

[Rep+12] J. Repp et al. "PENTATRAP: a novel cryogenic multi-Penning-trap experiment for high-precision mass measurements on highly charged ions". In: *Applied Physics B* 107.4 (2012), pp. 983–996 (cited on pages 1, 17).

[Rep12] J. Repp. "The setup of the high-precision Penning trap mass spectrometer PENTATRAP and first production studies of highly charged ions". PhD thesis. Ruprecht-Karls-Universität Heidelberg, 2012 (cited on pages 19, 20).

[RIB12] T. Rylander, P. Ingelström, and A. Bondeson. *Computational Electromagnetics*. Texts in Applied Mathematics. Springer, 2012. URL: https://books.google.de/books?id=gXUhER4HbPAC (cited on page 73).

[Ris11] A. Rischka. "Aufbau und Charakterisierung eines Systems zur Stabilisierung des Magnetfeldes an PENTATRAP". Bachelor's thesis. Ruprecht-Karls-Universität Heidelberg, 2011 (cited on page 20).

[Ris14] A. Rischka. "Aufbau eines Heliumdruck- und Heliumlevel-Stabilisierungssystems und Konstruktion eines kryogenen Faraday-Bechers für PENTATRAP". Master's thesis. Ruprecht-Karls Universität Heidelberg, 2014 (cited on page 20).

[Ris17] A. Rischka. "To be submitted". PhD thesis. Ruprecht-Karls-Universität Heidelberg, 2017 (cited on page 21).

[Rou+12] C. Roux et al. "The trap design of PENTATRAP". In: *Applied Physics B* 107.4 (2012), pp. 997–1005 (cited on page 17).

[Rou12] C. Roux. "High-resolution mass spectrometry. The trap design and detection system of Pentatrap and new $Q$-values for neutrino studies". eng. PhD thesis. Heidelberg, Univ., 2012, Online–Ressource. URL: http://archiv.ub.uni-heidelberg.de/volltextserver/14006/ (cited on pages 13, 37, 40–42, 53, 57).

[RTP04] S. Rainville, J. K. Thompson, and D. E. Pritchard. "An Ion Balance for Ultra-High-Precision Atomic Mass Measurements". In: *Science* 303.5656 (2004), pp. 334–338. URL: http://www.sciencemag.org/content/303/5656/334.abstract (cited on page 1).

[Sch02] P. Schmüser. "Superconductivity in high energy particle accelerators". In: *Progress in Particle and Nuclear Physics* 49.1 (2002), pp. 155 – 244. URL: http://www.sciencedirect.com/science/article/pii/S014664100200145X (cited on page 32).

[Sho38] W. Shockley. "Currents to Conductors Induced by a Moving Point Charge". In: *Journal of Applied Physics* 9.10 (1938), pp. 635–636. URL: http://scitation.aip.org/content/aip/journal/jap/9/10/10.1063/1.1710367 (cited on page 9).

[Sta98] S. Stahl. "Aufbau eines Experimentes zur Bestimmung elektronischer g-Faktoren einzelner wasserstoffähnlicher Ionen". PhD thesis. Johannes Gutenberg-Universität Mainz, 1998 (cited on page 9).

[Stu11] S. Sturm. "The $g$-factor of the electron bound in $^{28}Si^{13+}$: The most stringent test of bound-state quantum electrodynamics". PhD thesis. Johannes Gutenberg-Universität Mainz, 2011 (cited on pages 1, 11, 37, 38, 82).

[SU92] National Institute of Standards and Technology (U.S.) *NIST monograph*. NIST Monograph No. 177. U.S. Dept. of Commerce, National Institute of Standards and Technology, 1992, pp. 7–23. URL: http://books.google.de/books?id=TxRWAAAAYAAJ (cited on page 44).

[SWSB11] S. Sturm, A. Wagner, B. Schabinger, and K. Blaum. "Phase-Sensitive Cyclotron Frequency Measurements at Ultralow Energies". In: *Physical Review Letters* 107 (2011), p. 143003 (cited on pages 3, 13, 14).

[Ter43] F.E. Terman. *Radio Engineer's Handbook*. McGraw-Hill handbooks. McGraw-Hill Book Company, Incorporated, 1943. URL: https://books.google.de/books?id=QwCrAAAAIAAJ (cited on page 32).

[TMW15] P. A. Tipler, G. Mosca, and J. Wagner. *Physik für Wissenschaftler und Ingenieure. [der Begleiter bis zum Bachelor]*. 7. dt. Aufl. Lehrbuch. Berlin ; Heidelberg: Springer Spektrum, 2015, XXXVI, 1454 S. (Cited on page 29).

[Ulm+09] S. Ulmer et al. "The quality factor of a superconducting rf resonator in a magnetic field". In: *Review of Scientific Instruments* 80.12 (2009), p. 123302 (cited on pages 32, 33).

[Ulm+11] S. Ulmer et al. "Direct Measurement of the Free Cyclotron Frequency of a Single Particle in a Penning Trap". In: *Physical Review Letters* 107 (10 2011), p. 103002. URL: http://link.aps.org/doi/10.1103/PhysRevLett.107.103002 (cited on page 3).

[Ulm11] S. Ulmer. "First observation of spin flips with a single proton stored in a cryogenic penning trap". eng. PhD thesis. Heidelberg, Universität, 2011, Online–Ressource. URL: http://archiv.ub.uni-heidelberg.de/volltextserver/volltexte/2011/12306 (cited on pages 37, 38).

[Ver+04] J. L. Verdú et al. "Determination of the $g$-Factor of Single Hydrogen-Like Ions by Mode Coupling in a Penning Trap". In: *Physica Scripta* T112 (2004), pp. 68–72 (cited on page 13).

[WD75] D. J. Wineland and H. G. Dehmelt. "Principles of the stored ion calorimeter". In: *Journal of Applied Physics* 46 (1975), pp. 919–930 (cited on page 12).

[Zsc+09] G. Zschornak et al. *DRESDEN ELECTRON BEAM ION SOURCES: LATEST DEVELOPMENTS*. Tech. rep. Technische Universität Dresden and DREEBIT GmbH, 2009 (cited on pages 2, 19, 20).

## Danksagung

Zuerst möchte ich mich bei meinem Betreuer Klaus Blaum für die herzliche Aufnahme in seine Abteilung bedanken. Vielen Dank für die Möglichkeit, mich mit einem sehr spannenden Bereich der Physik zu beschäftigen und deine Unterstützung auch über diese Arbeit hinaus.

Vielen Dank an Wolfgang Quint für die Übernahme des Zweitgutachtens meiner Arbeit.

Besonderer Dank gilt Andreas Dörr, welcher mir stets mir Rat und Tat zur Seite stand und selbstverständlich das Korrekturlesen meiner Arbeit übernahm. Vielen, vielen Dank auch an Alexander Rischka für die tolle Unterstützung im Labor. Vielen Dank an alle PENTATRAP Mitglieder für die schöne Zusammenarbeit.

Für das weitere Korrekturlesen meiner Arbeit bin ich Jens Dilling, Jochen Ketter und Marc Schuh sehr dankbar!

Ebenfalls möchte ich mich bei Ralph Zilly für die Hilfe im Labor bedanken!

For the help in the lab, the discussions, during the writing phase, for every explanation given, for the nice and relaxing lunch and ice cream breaks, I thank the members of the Alphatrap, The-Trap and Piperade experiments.

Außerdem möchte ich mich bei meinen Eltern Ursula und Bobby und meiner Oma Annemie, sowie meinem Freund Julian Stark für die tolle Unterstützung bedanken.

## Erklärung:

Ich versichere, dass ich diese Arbeit selbstständig verfasst habe und keine anderen als die angegebenen Quellen und Hilfsmittel benutzt habe.

Heidelberg, den 29.5.2015 .....